

# Optical Studies of AlGaAs Photonic Crystal Waveguides



*Thesis submitted for Degree of Doctor of Philosophy*

*by Agoney Z. García-Déniz*

*Department of Physics and Astronomy*

*University of Sheffield*

*September 2005*

The cover picture shows a Meleager's Blue butterfly (*Meleageria daphnis* or *Polyommatus daphnis*). The surface of its wings are coated with tiny scales pitted with arrays of submicrometre-sized holes the form a natural photonic crystal.

**To Maite**

---

# Table of Contents

Abstract	viii
Publication list	ix
Acknowledgements	x
<b>Chapter 1: General Introduction</b>	<b>1</b>
1.1 Motivation and Technological Background	2
1.2 Outline	6
<b>Chapter 2: Introduction to Linear and Nonlinear Photonic Crystals</b>	<b>9</b>
2.1. Introduction to Photonic crystals	10
2.2. Theoretical Background	12
2.2.1. The Master Equation	12
2.2.2. Study of Symmetry	16
2.2.3. Physical Origin of the Photonic Band Gap	20
2.3. Introduction to Nonlinear Optics	26
2.4. Nonlinear Effects in Photonic Crystals	36
2.5. Conclusions	41

---

**Chapter 3: Linear and Nonlinear Measurements of 2-D**

<b>Photonic Crystal Ridge Waveguides</b>	<b>46</b>
<b>3.1. Introduction</b>	<b>47</b>
<b>3.2. Sample Preparation</b>	<b>48</b>
<b>3.2.1. Introduction to Materials</b>	<b>48</b>
<b>3.2.2. In-Plane Transmission Geometry Samples</b>	<b>49</b>
<b>3.2.3. Reflectivity Geometry Samples</b>	<b>60</b>
<b>3.3. Linear Characterization Methods</b>	<b>61</b>
<b>3.3.1. Experimental Techniques for Transmission Spectroscopy</b>	<b>61</b>
<b>3.3.2. Experimental Set-Up and Samples</b>	<b>63</b>
<b>3.3.3. Experimental Results</b>	<b>67</b>
<b>3.4. Introduction to Nonlinear Measurements on Photonic Crystal Ridge Waveguides</b>	<b>75</b>
<b>3.4.1. Nonlinear Measurements in Photonic Crystal Waveguides</b>	<b>75</b>
<b>3.4.2. Experimental Results</b>	<b>78</b>
<b>3.4.3. Perpendicular Pump-Probe Geometry</b>	<b>86</b>
<b>3.5. Conclusions</b>	<b>90</b>

**Chapter 4: Real Carrier Nonlinear Properties of 1D Photonic**

<b>Crystal Waveguides</b>	<b>97</b>
<b>4.1. Introduction</b>	<b>98</b>

---

<b>4.2. Introduction to Semiconductor Quantum Wells</b>	<b>99</b>
<b>4.3. Experimental Methods</b>	<b>103</b>
<b>4.3.1. Samples</b>	<b>103</b>
<b>4.3.2. Reflectivity Measurements</b>	<b>105</b>
<b>4.3.3. Modeling of Reflectivity Spectra</b>	<b>114</b>
<b>4.4. Linear Characterization</b>	<b>116</b>
<b>4.5. Time-Resolved Pump-Probe Reflectivity Measurements</b>	<b>121</b>
<b>4.5.1. Experimental Details</b>	<b>121</b>
<b>4.5.2. Single and Two photon absorption tuning of photonic resonances</b>	<b>125</b>
<b>4.5.3. Two and Three photon absorption tuning of photonic resonances</b>	<b>139</b>
<b>4.6. Conclusions</b>	<b>156</b>

<b><i>Chapter 5: Nonlinear Switching Properties of 1D Photonic Crystals</i></b>	<b>162</b>
<b>5.1. Introduction</b>	<b>163</b>
<b>5.2. Experimental Setup Modifications</b>	<b>164</b>
<b>5.3. Nonlinear Response Lifetime Control via Alteration of the Photonic Crystal Waveguide Parameters</b>	<b>168</b>
<b>5.3.1. Period and Fill Factor (Stripe Width)</b>	<b>168</b>

---

5.3.2. Modeling of the Dependence of the Nonlinear Response Lifetime on the Stripe Width	172
5.3.3. Etch Depth	177
5.4. Subpicosecond Switching via Virtual Nonlinearities	181
5.4.1. Subpicosecond Switching via the Nonlinear Kerr Effect	182
5.4.2. Subpicosecond Switching via the Optical (AC) Stark Effect	188
5.5. Conclusions	196
<b>Chapter 6: Summary and Conclusions</b>	<b>202</b>
6.1. Summary and Conclusions	203
6.2. Future Work	207

---

# **Optical Studies of AlGaAs Photonic Crystal Waveguides**

*Agoney Z. García-Déniz*

## **Abstract**

This thesis describes a number of optical spectroscopic measurements in novel one and two dimensional photonic crystals patterned in a slab waveguide.

Two dimensional photonic crystals have also been embedded in a ridge waveguide to confine light to the plane containing the photonic crystal. Linear characterization of these structures revealed a photonic band gap. Nonlinear measurements revealed pulse compression, negative differential transmission and showed that the ridge waveguide nonlinear response dwarfs that of the photonic crystal.

Pump-probe spectroscopy is used to study the nonlinear response of AlGaAs/InAlGaAs MQW one dimensional photonic crystals. The modulation of the reflectivity spectra due to the refractive index change produced by two and three-photon induced free-carriers was measured. Pump-induced blue-shifts in the wavelength of photonic resonances were measured. These were followed by rapid decay  $\sim 25$  ps. The blue-shifts in the photonic resonances were as large as 15 nm.

The lifetime of free-carrier nonlinearities in one dimensional photonic crystals was found to depend on the photonic crystal parameters, i.e. period, air fill factor and etch depth. It was found that the free-carrier nonlinearities lifetime varied from 8 to 33.5 ps.

Ultrafast tuning of the photonic resonances was obtained via the optical Kerr effect and the optical (AC) Stark effect. Decay-less tuning was observed. The response time was measured to be at FWHM  $\sim 300$ -400 fs.

---

## Publications List

1. A.D. Bristow, D.O. Kundys, **A. Z. García-Déniz**, J.-P.R. Wells, A.M. Fox, M.S. Skolnick, D.M. Whittaker, A. Tahraoui, T.F. Krauss, J.S. Roberts, “Ultrafast nonlinear tuning of the reflection properties of AlGaAs in photonic crystal waveguides by two-photon absorption,” J. Appl. Phys. 96, 4729 (2004).
2. A.D. Bristow, **A. Z. García-Déniz**, A.M. Fox, D.M. Whittaker, M.S. Skolnick, T.F. Krauss, M. Hopkinson, "Reflection and emission of Brillouin zone edge states for active photonic crystal waveguides" J. Opt. A: Pure Appl. Opt. 7 S270-S275 (2005).
3. P. Murzyn, **A.Z. Garcia-Deniz**, A.M. Fox, J.-P.R. Wells, D.M. Whittaker, M.S.Skolnick, T.F. Krauss and J.S. Roberts “Ultrafast nonlinear response of AlGaAs/InAlGaAs MQW photonic crystal waveguides” (submitted for publication to Physica Status Solidi B).
4. **A.Z. Garcia-Deniz**, P. Murzyn, D.O. Kundys, A.M. Fox, J.-P.R. Wells, D.M. Whittaker, M.S.Skolnick, T.F. Krauss and J.S. Roberts, “Subpicosecond reflectivity modulation in AlGaAs/InAlGaAs MQW photonic crystal waveguides”, *manuscript in preparation*.
5. P. Murzyn, **A.Z. Garcia-Deniz**, D.O. Kundys, A.M. Fox, J.-P.R. Wells, D.M. Whittaker, M.S.Skolnick, T.F. Krauss and J.S. Roberts, “ Modulation of the nonlinear properties of 1-D photonic crystals via alteration of sample parameters“, *manuscript in preparation*.

---

## Acknowledgements

I would like to thank, in no particular order, Prof. D.M. Whittaker, for his scattering matrix modeling suite and help with theoretical understanding, Dr. J.P.R. Wells for his help in the ultrafast laboratories and encouragement, Dr. P. Murzyn for his help in this crucial final year, and my supervisors Dr. A.M. Fox and Prof. M.S. Skolnick.

Thank you to our collaborators, in particular to the growth and fabrication staff of the EPSRC National Centre for III-V Technologies at the University of Sheffield, and to Dr. A. Tahraoui and Prof. T. F. Krauss at the School of Physics and Astronomy at the University of St. Andrews for processing the photonic crystal samples used in this work.

Many thanks to Dr. Dr. Santiago Olaizola for all the help with Linux and the conversations in Spanish.

I would also like to thank, in no particular order, my former and current fellow PhD students: Dr. Ian Sellers, Dr. Ruth Oulton, Dr. Richard Green, Dr. Alan Bristow, Dymtro Kundys, Wing Ng, Andrew Ebbens, Tom Badcock, James Brown, Ahmadreza Daraei, Ali Hashemizadeh, Ahmed Alyamani and everyone else I have forgotten.

Me gustaría agradecerle el apoyo incondicional durante estos largos años a Toña, Miguel Angel, Famara y al resto de mi familia. Muchas gracias. Gracias a Maite por soportarme durante estos años, especialmente durante estos últimos meses. Muchas gracias. Te quiero mucho.

# **Chapter 1: General Introduction**

## **1.1 Motivation and Technological Background**

## **1.2 Outline**

“This is the sort of English up with which I shall not put”

*Winston Churchill*, attributed.

### **1.1 Motivation and Technological Background**

In 1987, Eli Yablonovitch<sup>1</sup>, on his quest to increase the efficiency of telecommunication lasers and, Sajeev John<sup>2</sup>, whose goal was to achieve light localization, separately proposed the first artificial photonic crystals. However, photonic crystals have existed for several hundred million years in the form of opal gems. These are formed by the self assembly of nanometre sized colloidal silica, which naturally tend to form a three dimensional lattice. Incidentally, artificial opals are formed in much the same manner<sup>3</sup>, on a far shorter time scale and are a very active area of research. Another example of natural photonic crystals is the wings of many butterflies, which are formed by a lattice of air holes. This is nothing less than a photonic crystal.

When in 1947 the transistor effect was discovered and the first device manufactured at Bell Labs by Shockley, Bardeen and Brattain, the computer era had dawned. Along with the first modem computers came the first networks, in the 1960's. ARPANET was the first packet switching network and progenitor of the internet. In 1989, Tim Berners Lee proposed a global hypertext project, later known as the World Wide Web. The project aim was to allow scientists to work together by combining their knowledge in a world wide web of hypertext documents. The WorldWideWeb program was first made available within CERN in December 1990 and on the internet in the summer of 1991.

The explosion of internet use has led to an ever increasing interest and demand in telecommunications. Higher bandwidth networks are a necessity as, not only the number of broadband connections, but also the bandwidth of these connections, continues to increase. Most of the “last mile” network still relies on copper wires, but the large backbones use optical fibres due to the larger bandwidths.

The first useful optical fibre was created in 1970 by a team of researchers at Corning Glass Works. It consisted of Titanium doped silica that worked at  $\lambda = 633 \text{ nm}$  with a loss of 17 db/km. Nowadays, optical fibres have attenuations of 0.2 db/km at  $\lambda = 1.55 \text{ }\mu\text{m}$ , which allow bandwidths in excess of several tens of Gigabits per second, while there are reports of experimental fibres that have bandwidths of one terabit per second.

The next step in optic fibres could come from photonic crystal fibres. These can be of two types: “holey” fibres<sup>4</sup> or air guiding fibres<sup>5</sup>. Photonic crystal fibres could guide light on air. The advantages of this would include: reduced nonlinearity, controllable dispersion, increased damage threshold and ultra-low optical attenuation.

While significant improvements have been made on the quality of the fibres, regarding attenuation, dispersion and nonlinearity control, the underlying circuitry used to process the optical signal is still electronic in nature. The optic fibres simply transport light. The light is then converted into electricity, processed, and finally converted back into light. This is normally referred to as node by node electrical processing. Photonic crystals could be used to create all-

optical data and voice communications systems that would operate significantly faster, allow larger bandwidths and operate more reliably. All-optical switches have been one of the major stumbling blocks to all-optical communications systems. The experiments carried out in this thesis will demonstrate the suitability of photonic crystals for all-optical switching in picosecond and subpicosecond time scales. This will allow switching speeds of tens of gigahertz and several terahertz respectively. Furthermore, the nonlinear response lifetime in one dimensional photonic crystals will be shown to depend on the photonic crystal sample parameters, which could be used for highly customizable all-optical switches.

The superprism effect can help in dense wavelength division multiplexing systems by substituting the silica based waveguide grating filter normally used in such systems. This effect is a simple enhancement of the effects of a normal prism, i.e. dispersion, and angle steering due to super dispersion and ultra refraction which are ultimately caused by the highly anisotropic nature of photonic crystals, which make propagation of light through the super prism very sensitive to changes in angle and wavelength. Optical time division multiplexing could be feasible for two dimensional photonic crystals embedded in ridge waveguides (this type of structures will be studied in this thesis), that present enhanced third order nonlinearities, which could be accomplished by growing quantum dots or quantum wells on the core and/or cladding layers.

The telecommunications revolution could not have occurred without the development in 1960 of the laser by T.H. Maiman<sup>6</sup>, an extension of the maser

concept to optical wavelengths. But it is not until the development of the semiconductor laser, with its low power requirements and minute sizes, along with the light emitting diode, that finally allowed the extensive use of lasers and light emitting diodes in telecommunications and thus bandwidth capacity increased substantially.

Photonic crystals can be used to create different type of lasers: Band edge lasers operate without a cavity as they work by the enhancement of the emission at the band edge, which is caused by slow light, due to low group velocity at the edge of the Brillouin zone. These devices could not only work as planar lasers, but also as vertically emitting lasers. Using this same property of the band structure of photonic crystals, i.e. low group velocity at the edge of the Brillouin zone, light extraction from light emitting diodes could be greatly enhanced. Microcavity photonic crystal lasers, offer another example of photonic crystal lasers. These lasers present high quality factors and small mode volume that could lead to ultra low threshold lasers.

The wealth of applications of photonic crystals, particularly in the field of telecommunications make photonic crystals a very important field of research.

## **1.2 Outline**

This thesis will discuss experimental results obtained from measurements performed on AlGaAs based one and two dimensional photonic crystal structures.

Chapter 2 will begin with an introduction to photonic crystals and its theoretical basis. This will be followed by an introduction to nonlinear optics and finally an introduction to nonlinear effects in photonic crystals will conclude this chapter.

In chapter 3 the growth and fabrication methods used to manufacture photonic crystals will be discussed. A description of the experimental set-up will be given. Linear and nonlinear in-plane transmission measurements of two dimensional photonic crystals embedded in ridge waveguides will be presented and discussed. The emphasis of this thesis shifted from the in-plane transmission measurements on ridge waveguides photonic crystals to reflectivity measurements as insurmountable problems were found. The main original results of the thesis are presented in chapters 4 and 5.

Chapter 4 will discuss the linear and nonlinear properties of one dimensional high refractive index contrast photonic crystals. These samples include quantum wells in the waveguide core to enhance the nonlinear response. An external coupling technique in reflectivity geometry will be described. Linear spectroscopy will be used for characterization purposes. The nonlinear properties will be measured using a spectrally resolved pump-probe technique that will allow to measure the temporal and spectral response of the photonic crystals at the same time and therefore investigate the effects of free carriers in high refractive index contrast one dimensional photonic crystals.

Chapter 5 will discuss further nonlinear properties of high refractive index contrast one dimensional photonic crystals. The ability to engineer the nonlinear

response decay time of one dimensional photonic crystals at fabrication time via alteration of the period, air fill factor and etch depth will be discussed.

Instantaneous switching of photonic resonances via non-resonant pumping (optical Kerr effect) and via resonant pumping (optical (ac) Stark effect) will be also discussed in this chapter.

Chapter 6 will give some concluding remarks on the work presented. Also, suggestions for future work will be presented.

**References**

1. E. Yablonovitch, "Inhibited spontaneous emission in solid-state physics and electronics," *Phys. Rev. Lett.* **58**, 2059 (1987).
2. S. John, "Strong localisation of photons in certain disordered dielectric superlattice," *Phys. Rev. Lett.* **58**, 2486 (1987).
3. V.N. Astratov, Yu.A. Vlasov, O.Z. Karimov, A.A. Kaplyanskii, Yu.G. Musikhin, N.A. Berth, V.N. Bogomolov, A.V. Prokofiev, "Photonic band gaps in 3D ordered fcc silica matrices" *Phys. Lett. A.* **222** 349 (1996).
4. J.C. Knight, T.A. Birks, P.S. Russell, and D.M. Atkin, "All-silica single-mode optical fiber with photonic crystal cladding," *Opt. Lett.* **21** 1547 (1996).
5. R. F. Cregan, B. J. Mangan, J. C. Knight, T. A. Birks, P. St. J. Russell, P. J. Roberts, D. C. Allan, "Single-Mode Photonic Band Gap Guidance of Light in Air", *Science* **285** 1537 (1999).
6. T.H. Maiman, "Stimulated optical radiation in ruby" *Nature* **187** 493 (1960).

# **Chapter 2: Introduction to Linear and Nonlinear Photonic Crystals**

## **2.1. Introduction to Photonic crystals**

## **2.2. Theoretical Background**

### **2.2.1. The Master Equation**

### **2.2.2. Study of Symmetry**

### **2.2.3. Physical Origin of the Photonic Band Gap**

## **2.3. Introduction to Nonlinear Optics**

## **2.4. Nonlinear Effects in Photonic Crystals**

## **2.5. Conclusions**

“All generalizations are false, including this one”

*Mark Twain*

## 2.1 Introduction to Photonic Crystals

The main feature of a photonic crystal is its band gap, a range of frequencies for which electromagnetic radiation is not allowed to propagate through the crystal; this is analogous to the band gap in a semiconductor. Such a structure could behave as a perfect mirror for a particular range of wavelengths. This, in fact, has been known to occur for multilayer dielectric stacks formed by multiple layers with different refractive indices of appropriate thickness, usually one quarter of the wavelength for which the stack is designed to have high reflectivity at, i.e. the stop gap. This type of structure is normally called a distributed Bragg reflector. The underlying principle of a distributed Bragg reflector is that light undergoes multiple reflections at the different interfaces and for light satisfying the Bragg condition, i.e.  $2d\sin\phi = m\lambda$ , constructive interference will occur and almost all the light will be reflected.

A conceptually different approach would be to take the structure as having a refractive index that is modulated by some periodic function, a situation analogous to the solid state, where atoms are subjected to a periodic potential. This modulation of the refractive index can be extended to two and three dimensional structures as shown in figure 2-1 below.

The latter approach will be used throughout this thesis, as it is more adequate for the treatment of higher dimensional photonic crystals.

## 2.2 Theoretical Background

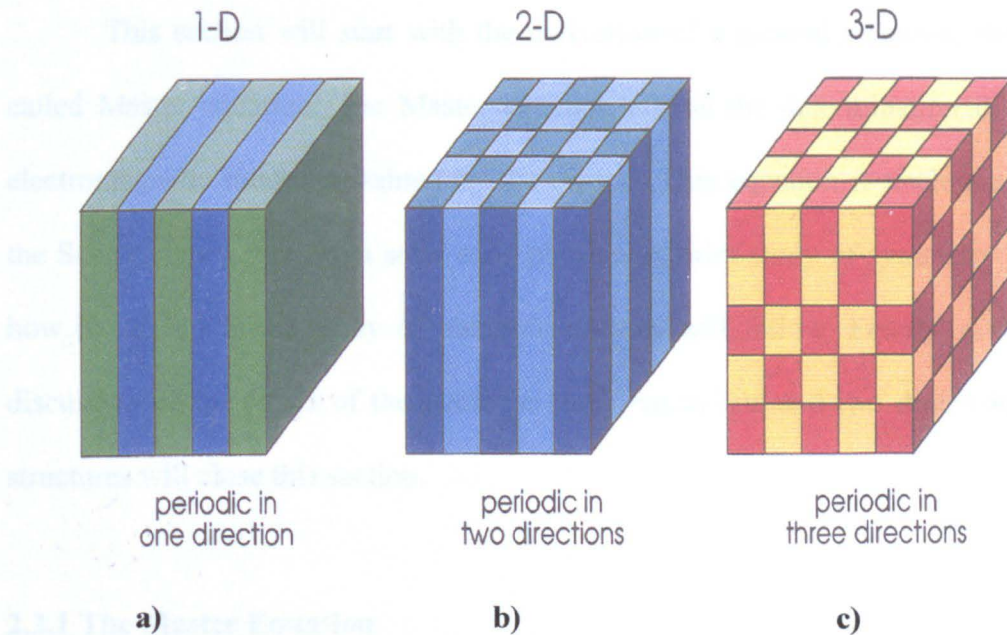


**Figure 2-1** Examples of a one, two and three dimensional photonic crystal<sup>1</sup>

The list of possible applications for photonic crystals is as long as it is varied: Threshold less lasers, narrow frequency filters, cavity less lasers, waveguides with bend radii of the order the operating wavelength, beam steering devices based on the superprism effect to name but a few linear effects<sup>2</sup>.

In this chapter, I give a brief introduction to the physics of photonics crystals and nonlinear optics.

In section 2.2 a theoretical background to photonic crystals will be discussed. Topics include the Master equation, symmetry in photonic crystals and the physical origin of the photonic band gap. Section 2.3 will give a brief introduction to nonlinear optics, while section 2.4 will concentrate in the nonlinear effects in photonic crystals.

## 2.2. Theoretical Background

This section will start with the derivation of a general equation, the so called Master equation. The Master equation allows the determination of the electromagnetic modes sustained by the crystal. This equation is analogous to the Schrödinger equation in solid state physics. A brief study of symmetry and how it can aid in the study of photonic crystals will follow. Finally, a short discussion of the origin of the photonic band gap in one and two dimensional structures will close this section.

### 2.2.1 The Master Equation

Maxwell's equations describe the propagation of light in macroscopic systems and thus can be used to describe the propagation of light in photonic crystals. This set of equations is scale invariant. While the Schrödinger equation in itself is scale invariant, constants like the Bohr radius or the electron mass set a fundamental scale. The analogies and differences between the electronic and photonic cases will be explored below.

Maxwell's equations are:

$$\begin{aligned}
 \nabla \cdot \mathbf{D}(\mathbf{r}, t) &= \rho \\
 \nabla \cdot \mathbf{B}(\mathbf{r}, t) &= 0 \\
 \nabla \times \mathbf{E}(\mathbf{r}, t) &= -\frac{\partial \mathbf{B}(\mathbf{r}, t)}{\partial t} \\
 \nabla \times \mathbf{H}(\mathbf{r}, t) &= \mathbf{J} + \frac{\partial \mathbf{D}(\mathbf{r}, t)}{\partial t}
 \end{aligned} \tag{2.1}$$

where  $\mathbf{D}$  is the displacement field,  $\rho$  is the free charge,  $\mathbf{B}$  is the magnetic

induction field,  $\mathbf{E}$  is the electric field,  $\mathbf{H}$  is the magnetic field and  $\mathbf{J}$  is the current density.

In order to simplify the task of obtaining an all encompassing equation for the electromagnetic case, equivalent to the Schrödinger equation in the semiconductor case, we shall make several simplifications.

Firstly, we will restrict the type of media. We shall deal only with a low loss mixed dielectric medium, i.e. a composite of regions of different dielectric materials with no currents and no free charges.

Secondly, we shall assume, without great loss of generality, that we are dealing with materials that are non magnetic, i.e.  $\mu_r = 1$ . This is reasonable assumption, at optical frequencies, so long as one is not dealing with ferromagnetic materials.

With these approximations in place, it is possible to write the induction magnetic field as follows:

$$\mathbf{B}(\mathbf{r}, t) = \mathbf{H}(\mathbf{r}, t) \quad (2.2)$$

Thirdly, we shall assume that we are dealing with macroscopic and isotropic media, in order to simplify the relationship between the electric field  $\mathbf{E}$  and the displacement field  $\mathbf{D}$ .

Fourthly,  $\epsilon(\mathbf{r})$  will be non-dispersive, i.e. independent of frequency. This is a gross simplification, but this assumption will simplify the mathematical treatment significantly.

Finally, we will restrict the electric field to small strengths, such that the dielectric function will only include linear terms. With all these assumptions and simplifications, the displacement field becomes:

$$\mathbf{D}(\mathbf{r}, t) = \varepsilon(\mathbf{r})\mathbf{E}(\mathbf{r}, t) \quad (2.3)$$

So now (2.1) becomes:

$$\nabla \cdot \varepsilon(\mathbf{r})\mathbf{E}(\mathbf{r}, t) = 0$$

$$\nabla \cdot \mathbf{H}(\mathbf{r}, t) = 0$$

$$\nabla \times \mathbf{E}(\mathbf{r}, t) = -\frac{\partial \mathbf{H}(\mathbf{r}, t)}{\partial t} \quad (2.4)$$

$$\nabla \times \mathbf{H}(\mathbf{r}, t) = \varepsilon(\mathbf{r}) \frac{\partial \mathbf{E}(\mathbf{r}, t)}{\partial t}$$

By using a complex valued field, harmonic modes can be written as a field pattern times a complex exponential:

$$\mathbf{H}(\mathbf{r}, t) = \mathbf{H}(\mathbf{r})e^{i\omega t} \quad (2.5)$$

$$\mathbf{E}(\mathbf{r}, t) = \mathbf{E}(\mathbf{r})e^{i\omega t}$$

Inserting (2.5) into (2.4) where appropriate we find for the divergence equations:

$$\nabla \cdot \varepsilon(\mathbf{r})\mathbf{E}(\mathbf{r}) = 0 \quad (2.6)$$

$$\nabla \cdot \mathbf{H}(\mathbf{r}) = 0 \quad (2.7)$$

And for the curl equations, repeating the same process yields:

$$\nabla \times \mathbf{E}(\mathbf{r}) = -i\omega\mathbf{H}(\mathbf{r}) \quad (2.8)$$

$$\nabla \times \mathbf{H}(\mathbf{r}) = i\omega\varepsilon(\mathbf{r})\mathbf{E}(\mathbf{r}) \quad (2.9)$$

If we now divide equation (2.9) by  $\varepsilon_0\varepsilon(\mathbf{r})$  and then take the curl we have

$$\nabla \times \frac{\nabla \times \mathbf{H}(\mathbf{r})}{\varepsilon(\mathbf{r})} = i\omega\nabla \times \mathbf{E}(\mathbf{r}) \quad (2.10)$$

This can be simplified if we use equation (2.8) to eliminate  $\mathbf{E}(\mathbf{r})$

$$\nabla \times \left( \frac{1}{\varepsilon(\mathbf{r})} \nabla \times \mathbf{H}(\mathbf{r}) \right) = \omega^2 \mathbf{H}(\mathbf{r}) \quad (2.11)$$

This is the so called Master equation; it is the photonic crystal equivalent of the Schrödinger equation in quantum mechanics.

Equations (2.7) and (2.11) determine  $\mathbf{H}(\mathbf{r})$ . Knowledge of  $\mathbf{H}(\mathbf{r})$  allows us to obtain  $\mathbf{E}(\mathbf{r})$  using:

$$\mathbf{E}(\mathbf{r}) = \left( -\frac{i}{\omega\epsilon(\mathbf{r})} \nabla \times \mathbf{H}(\mathbf{r}) \right) \quad (2.12)$$

This in turn, allows us to obtain  $\mathbf{D}(\mathbf{r})$  using (2.3).

The Master equation can be simplified to take the form of an eigenvalue equation

$$\Theta \mathbf{H}(\mathbf{r}) = \omega^2 \mathbf{H}(\mathbf{r}) \quad (2.13)$$

where  $\omega^2$  is the eigenvalue,  $\mathbf{H}(\mathbf{r})$  is the eigenvector and  $\Theta = \nabla \times \left( \frac{1}{\epsilon(\mathbf{r})} \nabla \times \right)$  is the differential operator. The differential operator,  $\Theta$  is linear and Hermitian<sup>3</sup>, and therefore, has real eigenvalues.

As discussed before, Maxwell's equations have no fundamental length scale. This is also a property of photonic crystals, which helped the research get off the ground by allowing the growth of structure in the microwave regime that required feature sizes on the centimetre scale. This property is also embedded in the Master equation as shall be demonstrated below.

Let us assume that we know the solution for the dielectric function  $\epsilon(\mathbf{r})$  and let us define a new dielectric function  $\epsilon'(\mathbf{r}) = \epsilon(\mathbf{sr})$ .

The Master equation (2.11) looks like this:

$$\nabla' \times \left( \frac{1}{\epsilon'(\mathbf{r}')} \nabla' \times \mathbf{H}'(\mathbf{sr}') \right) = (\omega s)^2 \mathbf{H}'(\mathbf{sr}') \quad (2.14)$$

If  $\mathbf{H}_n(\mathbf{r})$  satisfies the Master equation (2.11) for frequencies  $\omega_n$ , then the solutions of equation (2.14) are  $\mathbf{H}'_n(\mathbf{r}) = \mathbf{H}_n(\mathbf{sr})$  with  $\omega'_n = s\omega_n$ . The solution of the Master equation can therefore be easily scaled down or up, thus allowing for scaling of the solutions to any part of the electromagnetic spectrum.

### 2.2.2 Study of Symmetry

The study of the different types of symmetries of a crystal can be very useful to aid the understanding of the electromagnetic modes sustained by such a system. By virtue of their periodicity, all photonic crystals present discrete translational symmetry. It is, however, interesting to study a system that has continuous translational symmetry, e.g. an infinitely long thin slab of homogenous dielectric. Solution of the eigenvalue form of the Master equation yields a discrete number of modes below the light line  $\omega = ck$ , and a continuum of states above it. The former are guided on the slab, while the latter lie outside and are known as leaky modes<sup>1</sup>.

Let us now consider a system that has discrete translational symmetry. An infinite 1-D photonic crystal has a periodic modulation of the refractive index. This periodic modulation of the refractive index allows us to define a unit cell for the crystal, which forms the irreducible basis which through repetition forms the crystal. The primitive lattice vector is a vector with direction on the periodic axis and magnitude equal to the length of the unit cell; the length of this unit cell

$a$ , is normally referred to as the lattice constant of the crystal. Discrete translations in integer quantities of the primitive lattice vector will leave the crystal unchanged such that  $\varepsilon(\mathbf{r}) = \varepsilon(\mathbf{r} + \mathbf{R})$ , where  $\mathbf{R} = n \mathbf{a}$ ,  $n$  is an integer and  $\mathbf{a}$  is a primitive lattice vector. This translation is specified by the translation operator  $T_{\mathbf{R}}$ . The translation operator  $T_{\mathbf{R}}$  has to commute with the differential operator  $\Theta$  for the crystal to be truly symmetric under a discrete translation.  $T_{\mathbf{R}}$  operates on the eigenfunctions of  $\Theta$  and changes the value of the eigenvalues by  $\mathbf{R}$ . Addition of a primitive lattice vector to any lattice vector will land us on another lattice point with the same eigenvalue, i.e. the states will be degenerate. Any linear combination of eigenfunctions is itself an eigenfunction with the same eigenvalue. The states can be described as the product of a plane wave with a periodic modulation, similar to the Bloch<sup>4</sup> functions used in solid state physics.

The information about the modes sustained by a 3-D photonic crystal can be neatly stated in terms of the wavevector  $\mathbf{k}$  and the periodic Bloch function  $\mathbf{u}_{\mathbf{k}}(\mathbf{r}) = \mathbf{u}_{\mathbf{k}}(\mathbf{r} + \mathbf{R})$ .

By solving the Master equation (2.13) for  $\mathbf{u}_{\mathbf{k}}(\mathbf{r})$ , the eigenvalue equation can be rewritten as:

$$\Theta_{\mathbf{k}} \mathbf{u}_{\mathbf{k}}(\mathbf{r}) = \omega(\mathbf{k})^2 \mathbf{u}_{\mathbf{k}}(\mathbf{r}) \quad (2.15)$$

where  $\Theta_{\mathbf{k}} \equiv (i\mathbf{k} + \nabla) \times \left( \frac{1}{\varepsilon(\mathbf{r})} (i\mathbf{k} + \nabla) \times \right)$  is the differential operator. This operator

is also Hermitian<sup>1</sup>.

One consequence of discrete translational symmetry is that the crystal can be fully characterized by looking at a limited number of wavevectors. The Brillouin zone<sup>5</sup> is defined as the non-redundant range of wavevector values, i.e.

$$-\frac{\pi}{a} < k \leq \frac{\pi}{a}.$$

Similarly to the case of continuous translational symmetry, solution of the revised Master equation (2.15) yields a set of discrete modes. However, the modes now only extend as far as  $\pm \frac{\pi}{a}$  on  $k$ -space, due to the discrete translational symmetry. By subtracting the appropriate number of reciprocal lattice vectors<sup>6</sup> (RLV)  $\mathbf{G}$ , all modes which extend further than  $\pm \frac{\pi}{a}$  can be folded back into the Brillouin zone.

Rotational symmetry allows us to define the irreducible Brillouin zone. This is defined as the region within the Brillouin zone, where there are no redundant  $\omega_n(\mathbf{k})$ . Rotational symmetry, along with mirror reflection and inversion symmetry, define the point group symmetry of the crystal<sup>7</sup>. The corners of the irreducible Brillouin zone, see figure 2-2, are high symmetry points and are normally referred as  $\Gamma$ , M and K for triangular lattices and  $\Gamma$ , X and M for rectangular lattices.  $\Gamma$  represents the centre of the Brillouin zone, K (X) represent the nearest neighbour direction and M (M) the next nearest neighbour for a triangular (square) lattice.

An illustration of the Brillouin Zone and Irreducible Brillouin Zone for the most commonly used two dimensional lattice geometries is shown in figure 2-2. Figure 2-2 a) represents a two dimensional triangular lattice, and figure 2-2 b) represents a two dimensional square lattice.

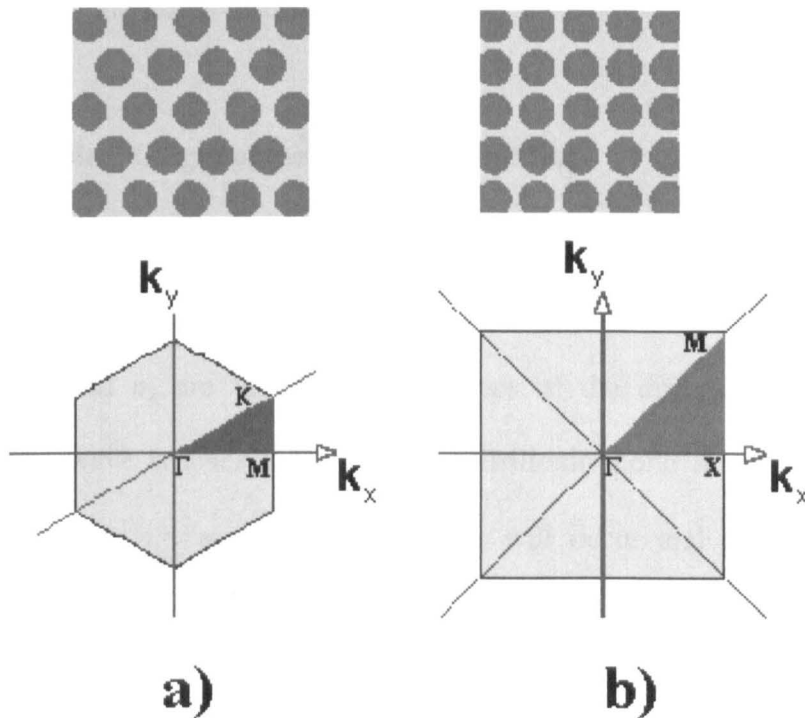


**Figure 2-2** Examples of Brillouin zone (light grey) and Irreducible Brillouin Zone (dark grey) for a triangular **a)** and a square **b)** two dimensional lattice.

To finalize the study of symmetries applied to photonic crystals, mirror reflection symmetry will be discussed next. Mirror reflection symmetry allows the Master equation (2.15) to be solved separately for each field polarisation. This allows the separation of the modes in a one or two dimensional photonic crystal as either: Transverse Electric modes for those modes that have the electric field  $\mathbf{E}$  parallel to the plane, i.e.  $E_x, E_y, H_z$  or Transverse Magnetic modes

for modes having their magnetic field  $\mathbf{H}$  parallel to plane, i.e.  $H_x, H_y, E_z$ . This assumes that the plane of the sample surface is the x-y plane. Different polarizations will lead to different band structures in two dimensional structures, whereas it will only lead to similar band structure with a small splitting in the one dimensional case.

### 2.2.3. Physical Origin of the Photonic Band Gap

The simplest type of photonic crystal, a one dimensional multiple bilayer structure, see figure 2-1 a), will show a photonic band gap as soon as  $n_1 \neq n_2$  where  $n_1$  and  $n_2$  are the refractive indices of the different layers. When a travelling wave reaches the end of the Brillouin Zone in a multiple bilayer structure with  $n_1 \neq n_2$ , Bragg reflections will occur and the waves become standing waves proportional to either:  $\cos\left(\frac{\pi x}{a}\right)$  or  $\sin\left(\frac{\pi x}{a}\right)$ , with wavelength  $2a$ , where  $a$  is the lattice constant as defined earlier. Such a wave can have its nodes positioned either on the high refractive index layers, or on the low refractive index layers.

The variational electromagnetic theorem<sup>1</sup> says that the low-frequency modes concentrate their energy in the high refractive index regions, and the high-frequency modes concentrate their energy in the low refractive index regions. This causes a band gap to open up. The bands on each side of the gap are called the dielectric and air bands, where the former is below the gap, and the latter is

above it. The size of such a gap will be proportional to the difference in refractive index. This only applies to one dimensional multiple bilayer stacks.

The more interesting case of two dimensional structures (see figure 2-1 b) will be discussed next. As discussed in section 2.2.2., mirror reflection symmetry allows us to separate the Master equation (2.15) into two different equations: transverse electric and transverse magnetic modes. These two different polarisations have different band structures.

A two dimensional square or hexagonal lattice of dielectric columns, can easily present a photonic gap for transverse magnetic modes, but not for transverse electric modes. The reason for this lies partly on the topology of the lattice but mainly on the nature of the fields. The displacement field of the lowest transverse magnetic mode, i.e. the dielectric band, concentrates most of its energy on the dielectric columns, thus lowering its frequency, whereas the next mode, the air band, concentrates most of its energy on the air surrounding the dielectric columns, thereby raising its frequency. Thus a photonic band gap is created.

The transverse electric modes do not show a band gap. This is due to their displacement field having a significant amount of energy in the air surrounding the columns for every band. As a result, there is hardly any contrast in the frequency of the bands. This stems from the vectorial nature of the displacement field for the transverse electric modes, where the field lines must be continuous and thus must go through air.

A square lattice of dielectric veins can easily present a band gap for transverse electric modes, but does not present a band gap for transverse magnetic modes.

The reason is that, now, the displacement field can stay in high dielectric regions in the dielectric band, whereas on the air band some of the field concentrates on air, thus increasing the frequency of the modes and creating a gap.

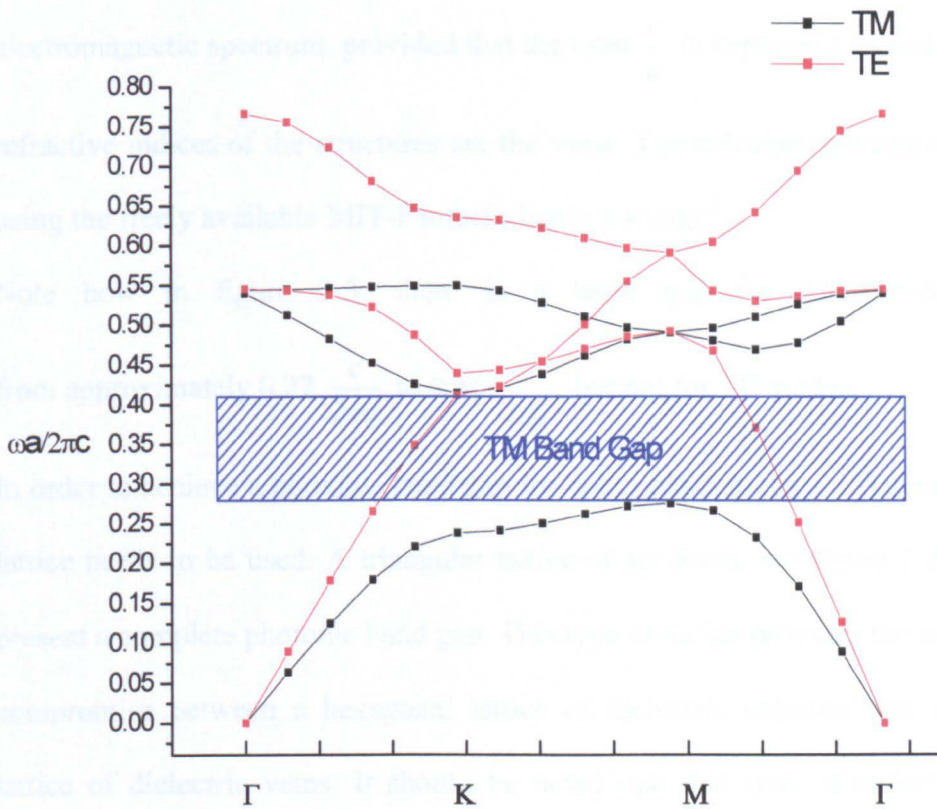


**Figure 2-3** Band structure of a two dimensional square lattice of dielectric rods with dielectric constant  $\epsilon = 12.69$ . The rod radius is set to  $r = 0.2a$ , where  $a$  is the period of the lattice. The hatched area represents the photonic band gap for transverse magnetic modes .

Figure 2-3 above shows a typical example of band structure calculation of a two dimensional square lattice of infinitely long dielectric rods holes, see figure 2-2 b). The dielectric constant is set to  $\epsilon = 12.69$ , this is the refractive index of GaAs at a wavelength of 900 nm. The rod radius is set to  $r = 0.2a$ , where  $a$  is the period and it is arbitrarily set. This is possible due to scalability, which enables photonic crystal to behave identically for completely different parts of the electromagnetic spectrum, provided that the ratio  $\frac{r}{a}$  is kept constant and that the refractive indices of the structures are the same. The calculation was performed using the freely available MIT-Photonic bands package<sup>8</sup>.

Note how in figure 2-3, there is a band gap for TM modes only from approximately  $0.27 \frac{c}{2\pi a}$  to  $0.41 \frac{c}{2\pi a}$ , but not for TE modes.

In order to achieve a photonic band gap for both polarisations a different type of lattice needs to be used. A triangular lattice of air holes, see figure 2-2 a), can present a complete photonic band gap. This type of lattice provides the necessary compromise between a hexagonal lattice of dielectric columns and a square lattice of dielectric veins. It should be noted that this type of lattice favours transverse electric gaps, but a complete gap tends to occur for  $\frac{r}{a} > 0.42$ <sup>9</sup>.

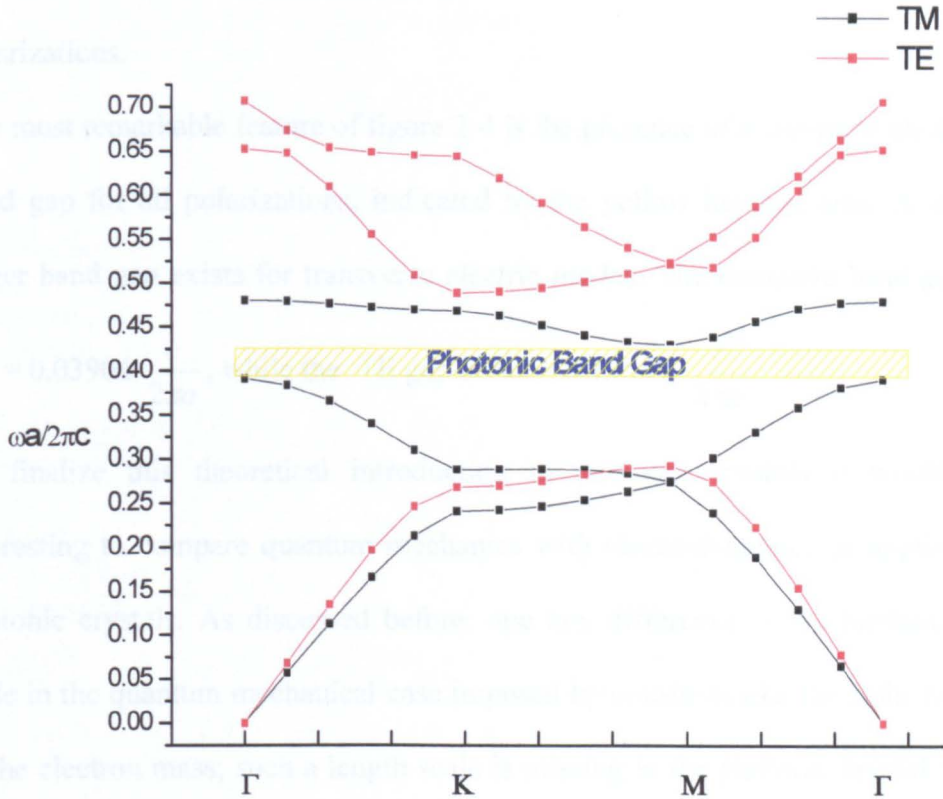


**Figure 2-4** Band structure of a two dimensional triangular lattice of air holes. The dielectric constant of the lattice is set to  $\epsilon = 12.69$ . The rod radius is set to  $r = 0.45a$ , where  $a$  is the period of the lattice. The hatched area represents the complete photonic band gap for both polarizations. Note how the transverse electric band gap is significantly bigger than the complete band gap.

Figure 2-4 shows a typical example of a band structure for a two dimensional triangular lattice. The band structure was again calculated using the MIT photonic bands package. The dielectric constant is set to  $\epsilon = 12.69$ , which is the refractive index of GaAs at a wavelength of 900 nm. The rod radius is set to  $r = 0.45a$ , where  $a$  is the period and again it is arbitrarily set. As discussed

above,  $r > 0.42a$  is necessary in order to yield a complete band gap for both polarizations.

The most remarkable feature of figure 2-4 is the presence of a complete photonic band gap for all polarizations, indicated by the yellow hatched area. A much larger band gap exists for transverse electric modes. The complete band gap is

$$\Delta\omega = 0.03904 \frac{c}{2\pi a}, \text{ while the TE gap is } \Delta\omega = 0.19644 \frac{c}{2\pi a}.$$

To finalize this theoretical introduction to photonic crystals it would be interesting to compare quantum mechanics with electrodynamics as applied to photonic crystals. As discussed before, one key difference is the fundamental scale in the quantum mechanical case imposed by constants like the Bohr radius or the electron mass; such a length scale is missing in the photonic crystal case. Another key difference is the nature of the Hermitian operators. In quantum mechanics the Hamiltonian is a scalar operator, whereas in the photonic crystal case it is a vector operator. Table 2-1 summarizes the main similarities and differences between quantum mechanics in a periodic potential and electrodynamics as applied to photonic crystals.

	<b>Quantum Mechanics in a Periodic Potential</b>	<b>Electrodynamics (Photonic Crystals)</b>
<b>Field</b>	$\Psi(\mathbf{r}, t) = \Psi(\mathbf{r})e^{i\omega t}$	$\mathbf{H}(\mathbf{r}, t) = \mathbf{H}(\mathbf{r})e^{i\omega t}$
<b>Eigenvalue Equation</b>	$H\Psi = E\Psi$	$\Theta\mathbf{H}(\mathbf{r}) = \omega^2\mathbf{H}(\mathbf{r})$
<b>Hermitian operator</b>	$H = -\frac{\hbar^2}{2m}\nabla^2 + V(\mathbf{r})$	$\Theta = \nabla \times \left( \frac{1}{\varepsilon(\mathbf{r})} \nabla \times \right)$
<b>Commutation Relationship</b>	$[H, T_R] = 0$	$[\Theta, T_R] = 0$
<b>Discrete Translation Symmetry</b>	$V(\mathbf{r}) = V(\mathbf{r} + \mathbf{R})$	$\varepsilon(\mathbf{r}) = \varepsilon(\mathbf{r} + \mathbf{R})$
<b>Bloch Theorem</b>	$\Psi_{\mathbf{k}_n}(\mathbf{r}) = u_{\mathbf{k}_n}(\mathbf{r}) \cdot e^{i\mathbf{k}_n \cdot \mathbf{r}}$	$\mathbf{H}_{\mathbf{k}_n}(\mathbf{r}) = u_{\mathbf{k}_n}(\mathbf{r}) \cdot e^{i\mathbf{k}_n \cdot \mathbf{r}}$

**Table 2-1** Comparison of Quantum Mechanics in a periodic potential and Electrodynamic applied to Photonic crystals

### 2.3. Nonlinear optics

In this section a short introduction to nonlinear optics will be given, where only topics relevant to this thesis will be discussed. The underlying assumption of linear optics is that the polarization vector,  $\mathbf{P}$ , depends linearly on the electric field  $\mathbf{E}$  of the light wave. This allows us to write:

$$\mathbf{P} = \chi\varepsilon_0\mathbf{E} \quad (2.16)$$

where  $\chi$  is the electric susceptibility and  $\varepsilon_0$  is the free space permittivity.

Equation (2.16) assumes that the medium is homogenous. The optical properties of anisotropic materials can be quantified by the susceptibility tensor  $\chi^{(n)}$ , where

$n$  indicates the order of the tensor. In the linear regime, the linear susceptibility tensor  $\chi^{(1)}$  is responsible for the refractive index, birefringence and trirefringence.

In nonlinear optics, the underlying assumption of linear optics is no longer valid and equation 2.16 must be modified to include higher order terms, so that it becomes:

$$\mathbf{P} = \epsilon_0 (\chi^{(1)} \mathbf{E} + \chi^{(2)} \mathbf{E}^2 + \chi^{(3)} \mathbf{E}^3 + \dots) \quad (2.17)$$

where  $\chi^{(1)}$  is the linear susceptibility tensor and  $\chi^{(2)}$  and  $\chi^{(3)}$  are the second and third order nonlinear susceptibility tensors respectively.

The internal field that binds an atom and an electron together is typically  $E \sim 10^{10} \text{ V m}^{-1}$ . An incident intensity of  $I \sim 10^{14} \text{ Wcm}^{-2}$  is required to obtain an optical field of such a magnitude. While intensities of this order can, nowadays, be achieved by tightly focusing powerful mode-locked lasers, in fact most nonlinear effects have a far lower intensity threshold. This is because, in certain conditions, the small nonlinear effects of many atoms can add up constructively to create a sizeable nonlinear effect. This will occur when the atoms are in phase with each other. This is the so-called phase matching condition.

A medium illuminated by two high intensity waves with different frequencies and amplitudes will reemit light at the sum and difference frequencies of the input fields. This is commonly referred to as nonlinear frequency mixing. Processes involving the mixing of two waves are related to the second order susceptibility tensor,  $\chi^{(2)}$ . The most common example is degenerate sum

frequency mixing, which, of course, is the same as second harmonic generation or frequency doubling, in this case  $2\omega = \omega + \omega$ .

The frequency doubling process can work the other way round such that:  $\omega_1 + \omega_2 = \omega$  and is normally called down conversion. In this process, a single input wave creates two waves at different frequencies. It is clear that there is a wide range of frequencies that can be created. In fact any frequency that maintains the energy conservation condition, should, in theory, be generated. In practice it is found that unless the process occurs under phase matching conditions, the intensity emitted is almost non-existent.

Down conversion is a very interesting process as it is the underlying basis of parametric amplification. In parametric amplification, a weak beam, called the signal, at frequency  $\omega_s$ , can generate a field at frequency  $\omega_i$ , normally called the idler, when there is a strong pump field at frequency  $\omega$  according to:  $\omega_i = \omega - \omega_s$ . The idler field increases the signal field amplitude (through mixing with the pump field). Thus, under phase-matching conditions, it is possible to transfer power from the pump field to the signal and idler fields. The degenerate case is the opposite of second harmonic generation.

The parametric amplification process can lead to parametric oscillation if the nonlinear crystal is placed inside a cavity with high reflectivity mirrors for the signal and idler frequencies. Thus through frequency mixing it is possible to obtain a tuneable “laser” or optical parametric oscillator (OPO) from a fixed wavelength laser. In subsequent chapters, an example of such a device will be used in the experimental set up. The Travelling wave Optical Parametric

Amplifier of Superfluorescence or TOPAS for short will be used as a tuneable pump laser.

The components of the second order susceptibility tensor  $\chi^{(2)}$  are zero for isotropic media, such as Centro-symmetric crystals or fluids due to isotropic media having inversion symmetry. This makes third order nonlinear process very important for isotropic media, as they are the lowest order nonlinear process available on such media. Third order nonlinear processes are generally referred to as four wave mixing processes and are related to the third order susceptibility tensor  $\chi^{(3)}$ . All the experimental data presented in this thesis involve third order nonlinear effects.

The optical Kerr effect<sup>10</sup> is arguably the most important third order nonlinear process. It is responsible for phase conjugate reflection, self focusing, soliton propagation, self phase and frequency modulation.

The optical Kerr effect involves four beams with the same frequency and is sometimes known as degenerate four wave mixing. Because the nonlinear polarization field has the same frequency as the input fields, there are no phase-matching conditions to be met.

One of the most important consequences of the optical Kerr effect is that the refractive index depends on the intensity of the input beam such that:

$$n(I) = n_0 + n_2 I \quad (2.18)$$

where the nonlinear refractive index  $n_2$  takes the form (for isotropic media):

$$n_2 = \frac{1}{n_0^2 c \epsilon_0} \chi^{(3)} \quad (2.19)$$

The optical Kerr effect is a virtual nonlinear effect. This means that no actual net transfer of energy takes place. A very interesting consequence of this is that the effect, i.e. the change in the refractive index, will only last for as long as the pump beam is on. This has profound implications for all-optical switching devices. Experimental evidence of the optical Kerr effect will be shown in chapter 5.

One of the consequences of the optical Kerr effect is self phase modulation. This is a change of the phase of an optical pulse due to the change in the refractive index caused by the same pulse. The magnitude of the phase shift after a distance  $l$ , is given by:

$$\phi = \frac{\omega_0 n_2 I}{c} l \quad (2.20)$$

The intensity varies throughout the pulse, and thus different parts of the pulse will have different phase shifts, leading to a frequency shift or chirp in the pulse, which is proportional to the distance travelled.

The instantaneous frequency is then:

$$\omega(t) = \omega_0 + \delta\omega(t) \quad (2.21a)$$

$$\text{where } \delta\omega = -\frac{d\phi}{dt} \quad (2.21b)$$

Using a constant phase, i.e. chirp free, hyperbolic secant pulse

$$I(t) = I_0 \text{sech}^2\left(\frac{t}{\tau}\right) \text{ and inserting into equation 2.20 we obtain 2.22a which,}$$

then gives 2.22b after substitution into 2.21b:

$$\phi(t) = \frac{\omega_0 n_2 I_0 \operatorname{sech}^2\left(\frac{t}{\tau}\right)}{c} l \quad (2.22a)$$

$$\delta\omega(t) = 2n_2 l \left(\frac{\omega_0}{c\tau}\right) I_0 \operatorname{sech}^2\left(\frac{t}{\tau}\right) \tanh\left(\frac{t}{\tau}\right) \quad (2.22b)$$

The instantaneous frequencies of the trailing half of the pulse are raised, while those in the leading half are lowered, provided that  $n_2 > 0$ ; the opposite situation occurs for negative values of  $n_2$ . This can be seen in Figure 2-5 below. The frequency chirp leads to spectral broadening which becomes significant when the frequency spread exceeds the initial pulse bandwidth.

It should be noted that the treatment presented above assumes that  $\frac{d^2 k}{d\omega^2} = 0$ , i.e.

the medium is not dispersive, for normal dispersion i.e.  $\frac{d^2 k}{d\omega^2} > 0$ , we see an

enhanced pulse broadening.

Normal dispersion enhances the spectral broadening caused by self phase modulation, because, in linear optics, the pulse in dispersive media contains a spread of frequencies that is determined by its Fourier transform. By contrast, a medium with anomalous dispersion will reduce the spectral broadening caused by the self phase modulation.

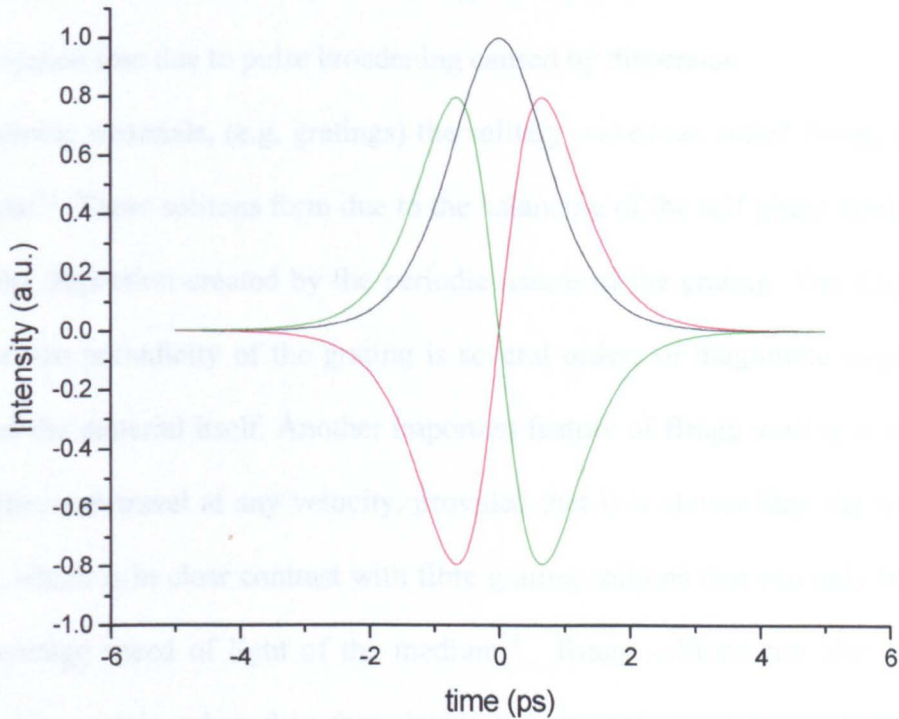


**Figure 2-5** Plot of a 1 ps hyperbolic secant pulse and  $\delta\omega(t)$  for positive and negative values of  $n_2$ , shown by red and green curves respectively. The black trace is the initial pulse.

A particularly interesting consequence of anomalous dispersion occurs when the anomalous dispersion in a media decreases the spectral broadening by the same amount that self phase modulation creates it, i.e. the spectral broadening is balanced out by the anomalous dispersion. This situation gives rise to optical solitons or solitary waves<sup>11,12</sup>.

One of the original goals of this thesis was the observation of solitons. These are waves that travel without spreading and were first discovered in water waves by John Scott Russell on the Union Canal outside Edinburgh. The implications for

telecommunications are very interesting, as solitary waves would not suffer information loss due to pulse broadening caused by dispersion.

In periodic materials, (e.g. gratings) the solitary waves are called Bragg grating solitons<sup>13</sup>. These solitons form due to the balancing of the self phase modulation and the dispersion created by the periodic nature of the grating. The dispersion due to the periodicity of the grating is several orders of magnitude larger than that of the material itself. Another important feature of Bragg grating solitons is that they can travel at any velocity, provided that it is slower than the speed of light, which is in clear contrast with fibre grating solitons that can only travel at the average speed of light of the medium<sup>13</sup>. Bragg solitons can also form in photonic crystals, when they form inside the photonic band gap and then they are called Gap solitons. These will be discussed in section 2.4.

The spectral broadening caused by self phase modulation is far from being a small effect and can be used for white light continuum generation or seeding optical parametric oscillators. White light continuum generation is widely used as a tunable femtosecond source and will be used for subsequent experiments in this thesis. This process relies on self phase modulation to spectrally broaden the laser pulse; self focusing will increase the intensity at the focus point and will trigger continuum generation. Field and avalanche ionization of the carriers reduces the intensity of the self focused pulse and thus limits the continuum bandwidth. Several materials are normally used to generate white light continuum, namely ethylene glycol<sup>14</sup>, sapphire, calcium fluoride, optic fibres<sup>15</sup>

and photonic crystal fibres<sup>16</sup>. Details of the technique used in this thesis are described in section 4.4.

The other important third order nonlinear effect for this thesis is two photon absorption. In two photon absorption, two photons are simultaneously absorbed to raise a valence electron to twice the photon energy into the conduction band. Since two photon absorption is a higher order process, its cross section is several orders of magnitude smaller than that of single photon absorption. Hence, two photon absorption normally occurs for high intensity laser beams with energies such that  $\hbar\omega < E_g < 2\hbar\omega$ , for which the material will be optically transparent.

Two photon absorption is known to induce changes in the refractive index via photo-generation of free carriers<sup>17</sup>. This makes two photon absorption an interesting process for all-optical switching devices in general and photonic crystal based all-optical switching devices in particular. In contrast to the optical Kerr effect, discussed previously in this section, this is a real or resonant nonlinear effect. In this type of nonlinear effect there is a net transfer of energy, and the effect persists for some time after the pump beam has been switched off. Despite this limitation, two photon absorption will be used extensively to generate free carriers that will alter the refractive index of photonic crystals, with the ultimate result of nonlinear shifting of the photonic resonances, as will be shown in chapter 4.

A schematic view of a typical two photon absorption process followed by radiative recombination is shown in Figure 2-6. A typical single photon absorption process is also shown for comparison.

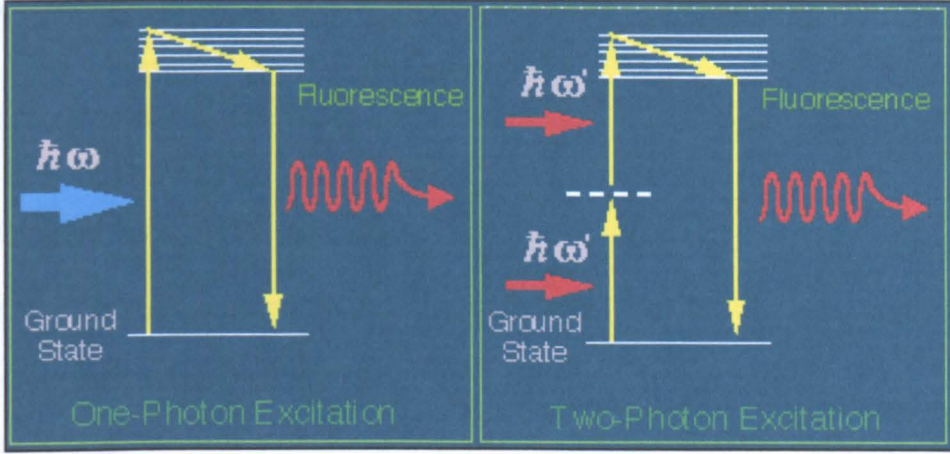


**Figure 2-6** Single and Two photon absorption processes followed by radiative recombination.

The two photon absorption coefficient  $\beta$  is defined by  $\frac{dI}{dz} = -\beta I^2$ . It is related

to the imaginary part of the third order nonlinear susceptibility tensor,  $\chi^{(3)}$ , by:

$$\beta = \frac{3\omega}{2\varepsilon_0 n^2 c^2} \text{Im}(\chi^{(3)}) \quad (2.23)$$

The free carrier density generated by a two photon absorption process can be calculated using<sup>18</sup>:

$$\frac{dN_e}{dt} = -\frac{N_e}{\tau} + \frac{\beta}{2\hbar\omega_p} I^2 \quad (2.24)$$

where  $I$  is the intensity of the pump beam,  $\omega_p$  is its angular frequency and  $\tau$  is the carrier lifetime.

If one assumes that the pulse duration,  $\tau_p$ , is much shorter than the carrier lifetime  $\tau$ , then the number of photo-generated carriers is<sup>19</sup>:

$$N = \frac{\beta I_0^2 \tau_p}{2\hbar\omega_p} \sqrt{\frac{\pi}{2}} \quad (2.25)$$

where the pulse is defined such that both the spatial and the temporal

distributions are included  $I(r, t) = I_0 \exp\left(-\frac{t^2}{\tau_p^2}\right) \exp\left(-\frac{r^2}{w^2}\right)$  where  $w$  is the

waist beam diameter at the sample.

Experimentally, the intensity of a Gaussian pulse is related to the average power  $P$  by the following relation<sup>19</sup>:

$$I_0 = \frac{P}{f_{rep} w^2 \pi^2 \tau_p} \quad (2.26)$$

where  $f_{rep}$  is the repetition rate of the pulsed source and  $w$  is the radius of the laser spot.

The refractive index change per carrier pair density can be estimated by<sup>20</sup>:

$$\sigma_N = \frac{e^2}{2\omega_{pr}^2 \epsilon_0 n_0 m_{eff}} \cdot \frac{E_g^2}{E_g^2 - (\hbar\omega_{pr})^2} \quad (2.27)$$

where  $\omega_{pr}$  is the angular frequency of the probe,  $m_{eff}$  is the reduced effective mass of the carriers, which is defined as  $m_{eff} = \frac{m_e \cdot m_h}{m_e + m_h}$ . It should be noted that

this equation refers to the free carrier nonlinearity only.

#### 2.4. Nonlinear effects in Photonic Crystals

The nonlinear properties of photonic crystals have been widely studied both theoretically and experimentally. The photonic band edge is one of the key properties of photonic crystals, perhaps more so, when it comes to nonlinear effects.

Second order nonlinear effects in photonic crystals, such as frequency doubling<sup>21</sup> or optical parametric processes<sup>22</sup>, are not studied in this thesis but are currently a very active area of research.

In this thesis I have concentrated in third order nonlinear processes in photonic crystals. Nonlinear shifts in the position of the photonic bands, can be achieved by changes in the refractive index due to the optical Kerr effect, or nonlinear refractive index, which can lead to bistability, and perhaps more importantly from an application point of view, to instantaneous all-optical switching devices. Similarly, the optical (ac) Stark effect can also produce instantaneous changes in the refractive index of a photonic structure. The optical Kerr effect and optical Stark effect will be discussed in sections 5.4 and 5.5 respectively. These two effects are virtual nonlinear effects, and therefore will only last for as long as the pump beam is on.

The carriers generated by single, two or three photon absorption can have the same effect on the refractive index, and consequently on the photonic bands. However, due to the nature of free carrier nonlinearities, i.e. real or resonant, these effects will present a rise time and a comparatively slow decay due to real carriers.

Changes in the refractive index are expected not only to shift the photonic band gap edges by several nanometres<sup>23</sup>, but also to change its bandwidth, as shown in Figure 2-7.

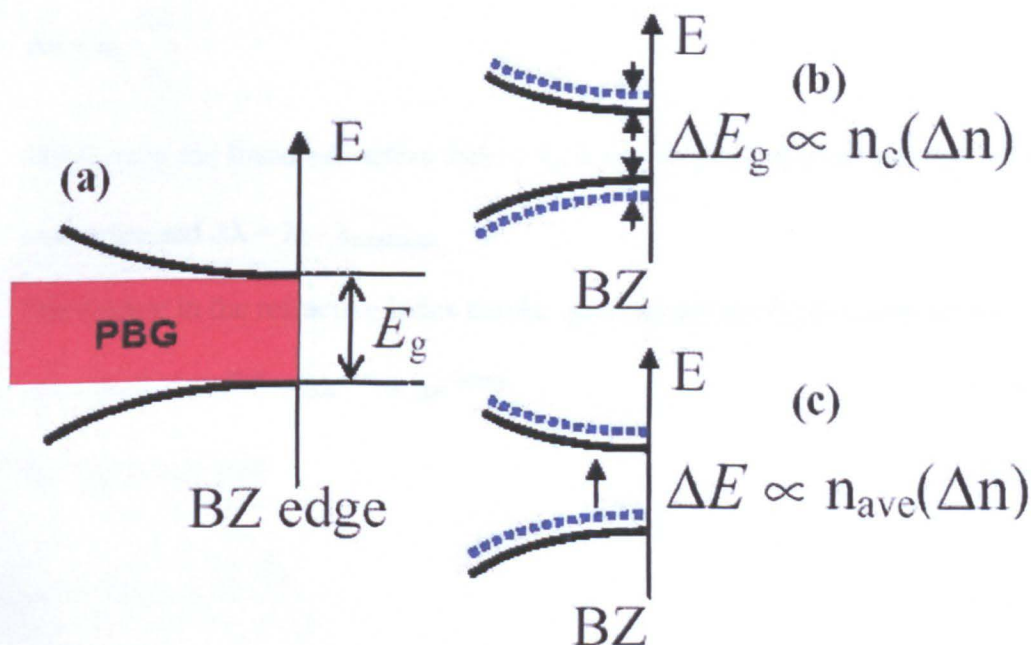


**Figure 2-7(a)** A schematic section of a photonic band structure close to the BZ edge. **(b)** Any change in the refractive index contrast ( $n_c$ ) will change the PBG ( $\Delta E_g$ ). **(c)** The effect  $\Delta n$  has on average refractive index of the core/cladding structure ( $n_{ave}$ ) and hence the entire shift of the band structure ( $\Delta E$ ).

There are two key parameters that should be considered: The refractive index

contrast between the core and cladding layers,  $n_c = \frac{n_{core}}{n_{cladding}}$ , henceforth  $n_c$ , and

the average refractive index of the core layer, henceforth  $n_{ave}$ .

$n_c$  and  $n_{ave}$  can be altered by using different lattice types, periods or air fill factors when patterning the structure.  $n_{ave}$  is inversely proportional to the air fill factor. The optical confinement of the waveguide will be affected by the changes of the refractive indices of the core and cladding.

The change in the refractive index and the shift of the photonic resonance are related by<sup>23</sup>:

$$\Delta n \approx n_0 \frac{\Delta \lambda}{\lambda_0} \quad (2.28)$$

where  $n_0$  is the linear refractive index,  $\lambda_0$  is the original spectral position of the resonance and  $\Delta \lambda = \lambda_0 - \lambda_{\text{nonlinear}}$ .

The change in the refractive index can be generalised, for high intensities to:

$$\Delta n = \Delta n^{fc} + \Delta n^{Stark} + \Delta n^{Kerr} + \Delta n^{thermal} \quad (2.29a)$$

$$\Delta n^{fc}(t) = \sigma_N \cdot N(t) \quad (2.29b)$$

$$\Delta n^{Stark}(t) \propto - \frac{|\mu \cdot E_p|^2}{\omega_p - \omega_{EX}} \quad (2.29c)$$

$$\Delta n^{Kerr}(t) = n_2 \cdot I(t) \quad (2.29d)$$

$$\Delta n^{Thermal}(t) = \frac{dn}{dT} \cdot \Delta T(t) \quad (2.29e)$$

Equation 2.29b refers to photo-generation of free carriers:  $\sigma_N$  is the change in the refractive index per carrier density, see equation 2.27, and  $N(t)$  is the number of photo-generated carriers. Equation 2.29c refers to the optical (ac) Stark effect, which will only occur for structures with large exciton strengths, i.e. samples that include multiple quantum wells, or other low dimensional structures.  $\mu$  is the exciton oscillator strength,  $E_p$  is the magnitude of the electric field,  $\omega_p$  is the pump angular frequency and  $\omega_{EX}$  is the exciton angular frequency.

Equation 2.29d, refers to the optical Kerr effect.  $n_2$  is the nonlinear refractive index and  $I(t)$  is the pump intensity. Finally, equation 2.29e refers to thermal effects, which should not be of any concern in this thesis due to their very long time constant.

Large densities of photo excited carriers ( $N \sim 10^{18}$ - $10^{19} \text{ cm}^{-3}$ ) will result in large changes in the refractive index  $\Delta n \approx 0.02$ <sup>23</sup>. Such a change in the refractive index will result in large changes in the photonic resonances. Using equations 2.27 and 2.25 a theoretical estimate of the change in refractive index due to two photon absorption can be achieved. This should allow us to estimate the change in the photonic crystal resonances and compare it with experimental results, as will be discussed in section 4.5.

Virtual carriers last only as long as the laser excitation lasts, and are therefore instantaneous. Examples of such instantaneous effects are the optical Kerr effect or the optical Stark effect<sup>24</sup>. The optical Kerr effect has been observed in low index contrast one dimensional photonic crystal (Bragg Mirror)<sup>25</sup>, and two dimensional silicon based photonic crystals<sup>26</sup>, but not in high contrast III-V based photonic crystals. The optical Stark effect has been observed in Bragg Mirrors<sup>27</sup> and in quartz based photonic crystals, using  $(\text{C}_6\text{H}_5\text{C}_2\text{H}_4\text{NH}_3)_2\text{PbI}_4$  also known as PEPI as the active semiconductor<sup>28</sup>.

In addition to ultrafast all-optical switching, third order nonlinear effects have several other applications in photonic band gap materials:

The nonlinear superprism effect, where the angle of refraction for a wave transmitted through the photonic crystal is changed by nonlinear shifts in the photonic band structure due to the nonlinear changes of the refractive index<sup>29</sup>.

Gap solitons<sup>30,31</sup>, these are a special case of Bragg grating solitons, as discussed before in section 2.3. Gap Solitons form in much the same way normal solitons form, i.e. when the group velocity dispersion balances the nonlinearity of the

medium, but all of this happens inside the photonic band gap. Gap solitons are very interesting solitary waves as they can travel at any speed, as long as it is not faster than the speed of light<sup>13</sup>, which is not the case for fibre solitons that can only travel at the speed of the medium. These effects are not considered further as they have not been studied in this thesis.

## 2.4 Conclusions

In this chapter a theoretical introduction to the linear and nonlinear properties of photonic crystals has been given. Only those effects of direct relevance to this thesis were discussed.

The Master equation, an equation that can be used to determine the modes sustained by the crystal, was derived from Maxwell's equations. The lack of a fundamental scale, naturally embedded in Maxwell's equations, is demonstrated to also be present in the Master equation. It was shown that the Master equation can be recast as an eigenvalue problem, with real eigenvalues, a consequence of the hermitian nature of the differential operator.

A brief discussion of symmetry showed that discrete translation symmetry can be used to define the Brillouin zone, which allows the crystal to be fully characterized by looking at a limited range of wavevectors. Rotational symmetry allows for a further reduction in the number of wavevectors necessary to characterize the crystal. Mirror reflection symmetry allows the Master equation to be solved differently for transverse electric, i.e. in-plane electric field, and transverse magnetic, in-plane magnetic field, polarizations.

It was established that the physical origin of the photonic band gap, in one dimensional photonic crystals, lies on the refractive index mismatch between the different component layers. In two dimensional photonic crystals the situation is more complicated, with the band gap also depending on the lattice topology.

In the introduction to nonlinear optics, particular emphasis was given to self phase modulation, and two photon absorption as these effects will play an important role in the experiments carried out in this thesis.

Finally, a general discussion of nonlinear effects in photonic crystals, showed the plethora of effects and possible applications of photonic crystals.

**References:**

1. J. D. Joannopoulos, R. D. Meade and J. N. Win, "Photonic Crystals: Molding the flow of light" (Princeton University press, 1995).
2. V. Berger, "Photonic crystals and photonic structures" *Current Opinion in Solid State and Materials Science* 4 209 (1999) and reference therein.
3. A Hermitian operator is defined such that  $f(\mathbf{r})$  and  $g(\mathbf{r})$  are well behaved functions of  $\mathbf{r}$ , so that  $\int f \hat{Q} g dt = \int g \hat{Q}^* f dt$ . The eigenvalues of such operators are always real. Every quantum mechanical operator representing an observable must be Hermitian.
4. C. Kittel, "Introduction to Solid State Physics," (1986) Wiley.
5. The first Brillouin zone is defined to be the Wigner-Seitz primitive cell of the reciprocal lattice, it can also be defined as the set of points in  $\mathbf{k}$  space that can be reached from the origin without crossing any Bragg plane.
6. See for instance, N. Ashcroft and N. D. Mermin, "Solid State Physics" Saunders College (1976).
7. A characteristic set of symmetry operations particular to a molecule, lattice, etc that leaves the molecule, lattice unchanged after the operation.
8. The MIT-Photonic band package website is <http://ab-initio.mit.edu/mpb/>
9. L.C. Andreani and Mario Agio, "Photonic Bands and Gap Maps in a Photonic Crystal Slab," *IEEE J. Quantum Electron.* Vol. XX, No Y, 1 (2001).
10. See for instance, Y.R. Shen, "The Principles of Nonlinear Optics" Wiley (1984).
11. D.N. Christodoulides, R.I. Joseph, "Discrete self-focusing in nonlinear arrays of coupled waveguides" *Opt. Lett.* 13, 794 (1988).
12. A.B. Aceves, C. De Angelis, S. Trillo, S. Wabnitz "Storage and steering of self-trapped discrete solitons in nonlinear waveguide arrays" *Opt. Lett.* 19, 332 (1994).
13. B. J. Eggleton, R.E. Slusher, C. M. de Sterke, P.A. Krug, J.E. Sipe, "Bragg Grating Solitons" *Phys Rev Lett.* 76(10) 1627 (1996).

14. R.L. Fork, C.V. Shank, C. Ifirlimann, R. Yen, W.J. Tomlinson "Femtosecond white light continuum pulses" Opt. Lett. Vol 8 1 (1983)
15. J.W. Nicholson, M.F. Yan, P. Wisk, J. Fleming, F. DiMarcello, E. Monberg, A. Yablon, C. Jorgensen, T. Veng, " All-fiber, octave spanning supercontinuum" Opt Lett Vol 28 643 (2003)
16. S. Coen, A.H.L. Chau, R. Leonhardt, J.D. Harvey, J.C. Knight, W.J. Wadsworth, and P.St.J. Russell, "White light supercontinuum generation with 60-ps pump pulses in a photonic crystal fiber," Opt Lett Vol 26 1356 (2001).
17. A. D. Bristow, J.-P. R. Wells, W. H. Fan, A. M. Fox, M. S. Skolnick, D. M. Whittaker, A. Tahraoui, T. F. Krauss, J. S. Roberts, "Ultrafast nonlinear response of AlGaAs two-dimensional photonic crystal waveguides" Appl Phys Lett 83, 851 (2003).
18. I. Androsch, P. Glas, "Influence of spatio-temporal refractive index changes in a GaAs etalon on the generation of ultrashort pulses in a Nd-phosphate glass laser" Opt. Comm. 105 125 (1994).
19. H. Folliot, M. Lynch, A.L. Bradley, T. Krug, L. A. Dunbar, J. Hegarty, J.F. Donegan, L.P. Barry, "Two photon induced photoconductivity enhancement in semiconductor microcavities: a theoretical investigation" J Opt Soc Am B Vol 19, No 10, 2396 (2002).
20. T. G. Ulmer, R. K. Tan, Z. Zhou, S. E. Ralph, R. P. Kenan, C. M. Verber and A. J. SpringThorpe, "Two-photon absorption induced self-phase modulation in GaAs-AlGaAs waveguides for surface emitted second harmonic generation" Opt Lett 24 756 (1999).
21. A.R. Cowan, J. F. Young, "Mode matching for second harmonic generation in photonic crystal waveguides", Phys. Rev. B 65, 085106 (2001).
22. A. D. Bristow, J. P. Mondia, H. M. van Driel, J. F. Young, "Enhanced parametric Processes in 2-D GaAs photonic crystal waveguides", *conference presentation*.

23. A. D. Bristow, D. O. Kundys, A. Z. García-Déniz, J.-P. R. Wells, A. M. Fox, M. S. Skolnick, D. M. Whittaker, A. Tahraoui, T.F. Krauss, J.S. Roberts, "Ultrafast nonlinear tuning of the reflection properties of AlGaAs photonic crystal waveguides by two photon absorption" *J. Appl. Phys.* **96** 4729 (2004).
24. A. Mysyrowicz, D. Hulin, A. Antonetti, A. Migus, W.T. Masselink, H. Morkoc, "Dressed excitons" in a multiple quantum well structure: Evidence for an optical stark effect with femtosecond response time" *Phys Rev Lett.* **56**(25) 2748 (1986).
25. S.R. Hastings, M.J.A. de Dood, H. Kim, W. Marshall, H.S. Eisenberg and D. Bouwmeester, "Ultrafast optical response of a high-reflectivity GaAs/AlAs Bragg mirror" *Appl Phys Lett* **86**, 031109, (2005).
26. H.W. Tan, H.M. van Driel, S.L. Schweizer, R.B. Wehrspohn, U. Gösele, "Nonlinear optical tuning of a two-dimensional silicon photonic crystal" *Phys. Rev. B* **70**, 205110 (2004).
27. J.P. Prineas, J.Y. Zhou, J.Kuhl, H.M. Gibbs, G. Khitrova, S.W. Koch, A. Knorr, "Ultrafast ac Stark effect switching of the active photonic band gap from Bragg-periodic semiconductor quantum wells" *Appl Phys Lett* **81**(23) 4332, (2002).
28. M. Shimizu, T. Ishihara, "Subpicosecond transmission change in semiconductor-embedded photonic crystal slab: Toward ultrafast optical switching" *Appl Phys Lett* **80**(16) 2836, (2002).
29. N. C. Panoiu, M. Bahl, R. M. Osgood, Jr., "Optically tunable superprism effect in nonlinear photonic crystals" *Opt. Lett.* **28**, 2503 (2003).
30. W. Chen, D.L. Mills, "Gap solitons and the nonlinear optical response of superlattices" *Phys. Rev. Lett.* **58**, 160 (1987).
31. N. Akozbek, S. John, "Optical Solitary waves in two- and three dimensional nonlinear photonic band gap structures" *Phys. Rev. E* **57** 2287 (1998).

# **Chapter 3: Linear and Nonlinear Measurements of 2-D Photonic Crystal Ridge Waveguides**

## **3.1. Introduction**

## **3.2. Sample Preparation**

### **3.2.1. Introduction to Materials**

### **3.2.2. In-Plane Transmission Geometry Samples**

### **3.2.3. Reflectivity Geometry Samples**

## **3.3. Linear Characterization Methods**

### **3.3.1. Experimental Techniques for Transmission Spectroscopy**

### **3.3.2. Experimental Set-Up and Samples**

### **3.3.3. Experimental Results**

## **3.4. Introduction to Nonlinear Measurements on Photonic Crystal Ridge Waveguides**

### **3.4.1. Nonlinear Measurements in Photonic Crystal Waveguides**

### **3.4.2. Experimental Results**

### **3.4.3. Perpendicular Pump-Probe Geometry**

## **3.5. Conclusions**

“Another victory like this and we are ruined”

*King Pyrrhus of Epirus*

### **3.1 Introduction**

In the previous chapter a theoretical introduction to photonic crystals was presented. The Master equation, an equation that can be used to determine the modes sustained by the crystal, was derived from Maxwell's equations. The properties of this equation were discussed. Analysis of the different crystal symmetries allows us to define the Brillouin zone, the irreducible Brillouin zone and to distinguish between transverse electric and transverse magnetic polarizations.

An introduction to nonlinear optics was also presented in the previous chapter, where self phase modulation and two photon absorption were explained in more detail as they will feature in the experimental results throughout this thesis, particularly two photon absorption.

In this chapter I report preliminary measurements on two dimensional photonic crystals embedded in ridge waveguides. Linear characterization measurements will reveal a photonic band gap. Nonlinear measurements will show evidence of symmetric and asymmetric spectral narrowing of the transmitted pulses.

In section 3.2 sample growth and fabrication techniques will be discussed. A description of photonic crystal waveguides and ridge waveguides will be given.

Section 3.3 will discuss the linear characterization methods used for two dimensional photonic crystals in this thesis. A detailed discussion of the samples

and experimental set-up used in this chapter will be followed by transmission measurements.

Finally, section 3.4 will attempt to repeat and improve an experiment carried out by Rahn *et al*<sup>1</sup>.

### **3.2 Sample Preparation**

In this section the fabrication methods used to manufacture the photonic crystals samples measured in this thesis will be discussed.

#### **3.2.1 Introduction to Materials**

Silicon has been the mainstay of the semiconductor industry for many years, perhaps due to its abundance on the earth's crust; therefore it is not surprising that some photonic crystals are manufactured using Silicon, typically Silicon on Insulator (SOI)<sup>2</sup> or Silicon Nitride<sup>3</sup>. Despite its advantages, Silicon lacks a simple mechanism to alter its refractive index gradually at the time of manufacture. Silicon alloys, like silicon nitride, are also not lattice matched to unalloyed silicon. Silicon also lacks good light emission properties, due to its indirect band gap. For these reasons, in this thesis I concentrate on GaAs based photonic crystals.

GaAs is a very good light emitter and possesses a simple mechanism to alter the refractive index, while remaining lattice matched to GaAs, through the introduction of aluminium into the GaAs crystal. This causes the refractive index of the crystal to decrease and makes GaAs(Al<sub>x</sub>Ga<sub>1-x</sub>As) a very interesting material for the study of photonic crystals.

Additionally, GaAs is robust, has a large optical nonlinearity and its electronic band gap edge is located at 1.424 eV at room temperature.

At room temperature the refractive index of  $\text{Al}_x\text{Ga}_{1-x}\text{As}$  and the band gap energy are as follow:

$$n = 3.59 - 0.7x + 0.15x^2 \quad \text{at } 900 \text{ nm} \quad (3.1)$$

$$E_g = 1.424 + 1.247x \text{ eV} \quad x < 0.45 \quad \text{Direct Energy Band Gap} \quad (3.2a)$$

$$E_g = 1.9 + 0.125x + 0.143x^2 \text{ eV} \quad x > 0.45 \quad \text{Indirect Energy Band Gap} \quad (3.2b)$$

In this thesis, two different experimental geometries will be used, namely in-plane transmission (discussed in this chapter), and external coupling reflectivity (discussed in chapters 4 and 5). Each will require somewhat different samples. I will start by considering the fabrication of photonic crystals for in-plane transmission measurements.

### **3.2.2 In-Plane Transmission Geometry Samples**

In order to realize a practical two dimensional photonic crystal, a slab waveguide needs to be created; this should not be confused with a ridge waveguide which is also used for the samples measured for this chapter. Figure 3-1 below, shows the difference between a slab waveguide, figure 3-1 a)-c) and a ridge waveguide figure d)-e). Note how the ridge waveguide is a simple optic fibre like waveguide. Without the slab waveguide light would leak out of the sample in the out of plane direction, while the ridge waveguide ensures that in-plane light is guided inside it via total internal reflection<sup>4</sup>. Thus the simultaneous

use of both types of waveguides create a simple and efficient way to confine light inside the sample in all three dimensions, so that it interacts with the photonic crystal which will be embedded in the ridge waveguide.

Due to the small size of the photonic crystal samples,(typical areas are several thousand square micrometers), transmission measurements are more complicated than with semiconductor wafers, in which light is shone on any area of the wafer and then collected after it has gone through the sample. Some micro-positioning system is required, as well as a means of identifying the photonic crystal itself from the rest of the wafer. The main approach used to solve this problem adopted in this thesis is to place the photonic crystal in a slab waveguide as well as in a ridge waveguide.

A slab waveguide consists of a central layer of semiconductor, known as the core, normally grown by epitaxial methods, surrounded by a material with lower refractive index, for instance: air or another semiconductor. Slab waveguides can be classified as either symmetric, if the material surrounding the core is the same on both sides, see figure 3-1 b)-c), or asymmetric, when the material on either side of the core is different, normally air on the top side and a different semiconductor on the lower side, see figure 3-1 a).

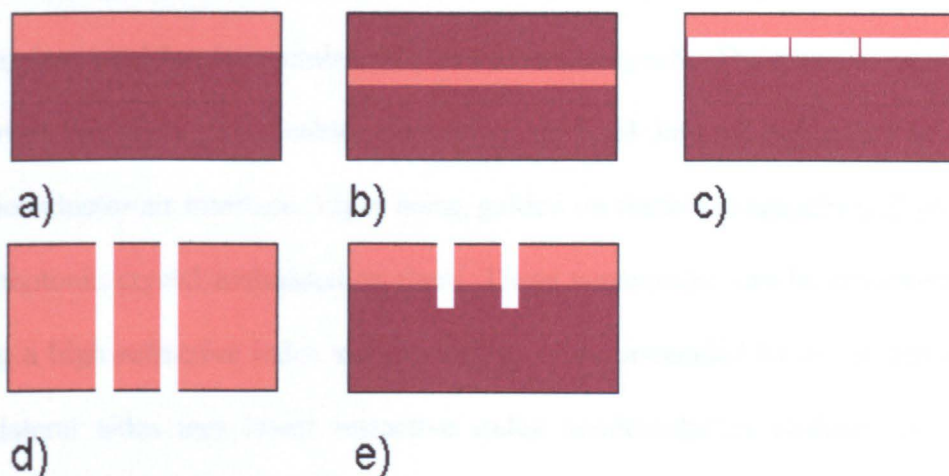


**Figure 3-1 a)-c)** Lateral views of an asymmetrical slab waveguide, a symmetrical slab waveguide and air bridge structure, respectively, see text for further details. The core layer is orange ( $n \sim 3.5$ ) The cladding is brown ( $n \sim 3.2$ ). **d)** Top view of a typical ridge waveguide. **e)** Lateral view of a typical ridge waveguide.

Placing the photonic crystal in a symmetric photonic crystal slab waveguide<sup>5</sup> with the photonic crystal in the centre layer or core will confine light to the core layer and thus, will probe the photonic crystal. This is illustrated in figure 3-2 b), where the red arrow shows the direction in which light travels. The light coupled to the waveguide is free to roam the plane where the photonic crystal is located. This limits the amount of light that will reach the photonic crystal, unless the sample is cleaved to impractically small dimensions. Another disadvantage of this type of symmetric waveguide is that the confinement can also be fairly limited as the refractive index contrast between the layers is not very large  $\Delta n \sim 0.3$ . These type of slab waveguides are, however, very simple to manufacture.

A more elegant solution consists of patterning a ridge waveguide, in which a photonic crystal has been embedded, in a slab waveguide. The ridge waveguide behaves like fibre optic cables and relies on total internal reflection at the semiconductor/air interface. Light being guided on these waveguides will probe the photonic crystal embedded on them. These waveguides can be asymmetric, using a high refractive index semiconductor core surrounded by air on top and the lateral sides and lower refractive index semiconductor cladding on the bottom layer, or can be symmetric and have air as the top, bottom and side cladding. The former will be used in this thesis, whereas the latter are normally referred to as air bridge structures<sup>6,7</sup>. Air bridge structures, see figure 3-1 c), have the higher confinement degree of all waveguides, but are fragile and complicated to fabricate.

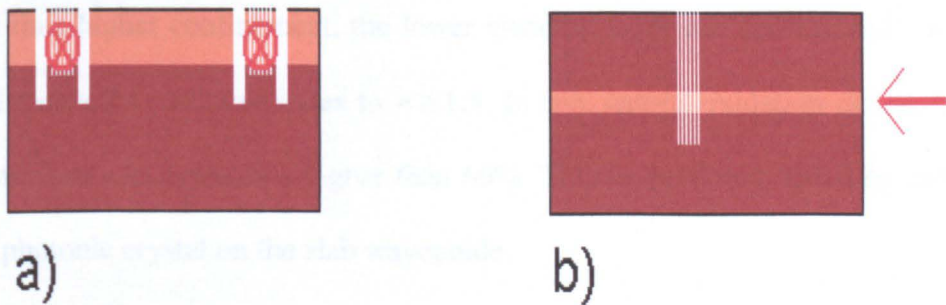


**Figure 3-2 a)** Side view of a photonic crystal embedded on a ridge waveguide in an asymmetric slab waveguide. **b)** Side view of a photonic crystal in a symmetric slab waveguide. Red arrows indicate direction of propagation of light.

A ridge waveguide patterned in an asymmetric slab waveguide represents a good compromise between ease of fabrication, performance and robustness. Such a

photonic crystal embedded on a ridge waveguide inside an asymmetric slab waveguide is shown in figure 3-2 a).

The slab waveguides used throughout this thesis are asymmetric<sup>8</sup> in nature, with the top cladding layer being air  $n \cong 1$ , the core typically composed of a 200 to 400 nm thick layer of high refractive index GaAs or  $\text{Al}_x\text{Ga}_{1-x}\text{As}$ ; GaAs is not normally used for the core as its electronic band edge gives rise to absorption at wavelengths shorter than 870 nm. A low Aluminium concentration  $\text{Al}_x\text{Ga}_{1-x}\text{As}$  layer is used instead; with Aluminium concentrations ranging from 10% to 20% (e.g.  $\text{Al}_{0.20}\text{Ga}_{0.80}\text{As}$  has a refractive index  $n \sim 3.45$  at 900 nm).

The bottom cladding layer is normally made of a higher aluminium concentration  $\text{Al}_x\text{Ga}_{1-x}\text{As}$ , where the concentrations can, typically, range from 35% to 90% or even AlAs (e.g.  $\text{Al}_{0.60}\text{Ga}_{0.40}\text{As}$  has a refractive index  $n \sim 3.22$  at 900 nm). In order to achieve an even higher refractive index contrast, and thus higher confinement, the lower cladding layer can be oxidized<sup>9</sup>, which will reduce its refractive index to  $n \cong 1.5$ . In fact, natural oxidation can occur for aluminium concentrations higher than 60%. This is, no doubt, aided by etching the photonic crystal on the slab waveguide.

The growth of the slab waveguide wafers was carried out by the EPSRC National Centre for III-V Technologies at the University of Sheffield using Metal Organic Vapour Phase Epitaxy (MOVPE). Once the slab waveguide has been grown, the photonic crystal must then be processed to create a Photonic Crystal Waveguide. The processing of the samples has been done at the University of St Andrews, by the Photonic Crystal research group.

In this thesis the relevant range of the electromagnetic spectrum is the very near infrared. This requires feature sizes of the order of 1  $\mu\text{m}$ . It is, therefore, not surprising that the samples are patterned using electron beam lithography, as feature sizes of tens of nanometres are easily achievable. It is, however, possible to pattern photonic crystals using deep ultraviolet photolithography<sup>10,11</sup>.

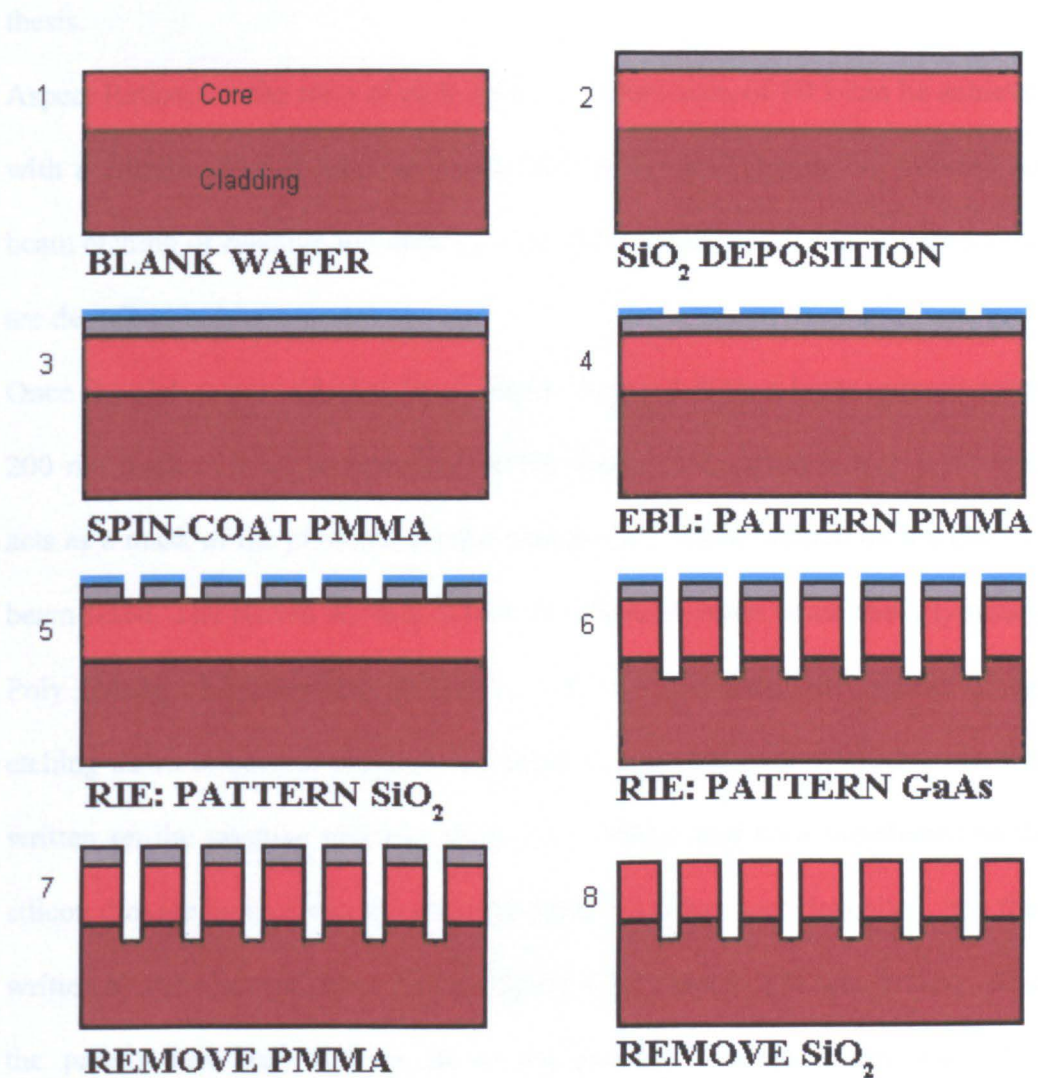


**Figure 3-3** Schematic sequence of the processing of a photonic crystal waveguide. (See text for details)

Dry etching methods are normally used to etch photonic crystal patterns. This is due to the requirements of a good photonic crystal, namely highly parallel cylindrical or square holes. In order to achieve this, anisotropic etching is required and thus wet etching methods are of little use. Chemically assisted ion beam etching or reactive ion etching is used in the samples measured in this thesis.

Aspect Ratios, i.e. the ratio of etch depth to feature size, of 10:1 can be achieved with a combination of electron beam lithography and chemically assisted ion beam etching or reactive ion etching. The steps in the processing of the samples are described below.

Once the slab waveguide has been grown, figure 3-3(1), a layer approximately 200 nm thick of SiO<sub>2</sub> is deposited on the waveguide, figure 3-3(2). This layer acts as a mask of the photonic crystal pattern that will be written on the electron beam resist. The reason for this is that, the electron beam resist used, typically, Poly (Methyl Methacrylate) (PMMA), will not withstand the rigours of dry etching down to several hundred nanometres. Thus the pattern needs to be first written on the positive electron resist, i.e. PMMA and then transferred to the silicon dioxide layer. Once the electron beam resist has been deposited, it is then written by the electron beam, figures figure 3-3(3) and 3-3(4) respectively. After the pattern has been written on to the positive electron beam resist it is developed on IPA:MIBK<sup>12</sup> for approximately 30 seconds. The pattern is then transferred to the SiO<sub>2</sub> layer using reactive ion etching with CHF<sub>3</sub> and into the waveguide using reactive ion etching with SiCl<sub>4</sub> or SiF<sub>4</sub>, figures 3-3(5) and 3-

and 3-3(6) respectively. Once the pattern has been etched into the waveguide, forming a photonic crystal waveguide, the PMMA and the SiO<sub>2</sub> layers are removed, as shown in figures 3-3(7) and 3-3(8).

The photonic crystal waveguide can now be checked by means of a scanning electron microscope; this allows us to check the period, air fill factor, the etch depth and how parallel the air cylinders are. In order to check the etch depth and air cylinder shape, a test sample is normally cleaved. The only way to check the shape of the air cylinders is by cleaving a sample.

Figure 3-4 a) below shows a typical example of a two dimensional photonic crystals with period  $a = 250$  nm and air fill factor  $f = 37\%$ . Figure 3-4 b) shows a typical two dimensional ridge waveguide sample, where there are ten ridge waveguides for each lattice direction and crystal length, of which eight contain a photonic crystal, and the outer two, not shown, are blank waveguides, used for normalization purposes. The photonic crystals shown here are 16  $\mu\text{m}$  long and the lattice direction is  $\Gamma\text{-K}$ . A typical sample comprises of four sets of ten such waveguides. There are two sets of ten ridge waveguides for each crystal length, 16 and 4  $\mu\text{m}$ , respectively, and each set has a different lattice direction. Each semiconductor chip comprises two such samples. In order to appropriately identify each ridge waveguide and waveguide set, the photonic crystal parameters are etched above the first waveguide of each set. Each ridge waveguide is then assigned a number from one to ten, with one being the first blank ridge waveguide below the photonic crystal information and ten being the

last blank ridge waveguide which surrounds the ridge waveguides containing photonic crystals, which go from two to nine.

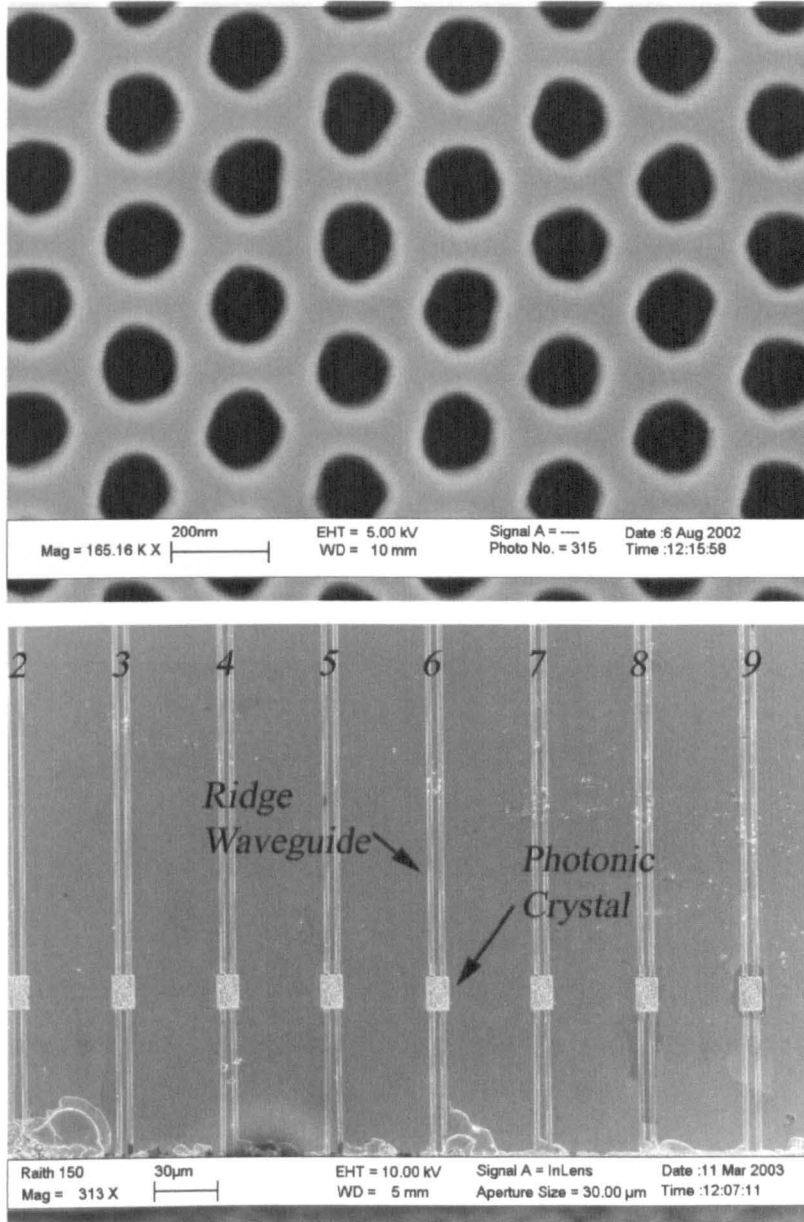


**Figure 3-4** Scanning electron microscopy micrographs. **a)** High resolution image of a two dimensional triangular lattice with period  $a = 250$  nm and air fill factor  $f = 37\%$ . **b)** Lower resolution image of a typical photonic ridge waveguide sample with several photonic crystals embedded in ridge waveguides. The length of the photonic crystal is  $16 \mu\text{m}$ .

Figure 3-5 shows a side view of a typical ridge waveguide. The etch depth,  $d \cong 2 \mu\text{m}$ , is significantly longer than used for photonic crystals, which is normally less than  $1 \mu\text{m}$ . This is done to ease the coupling of the laser light to the ridge waveguide. The bent trenches are an artefact of the micrograph.

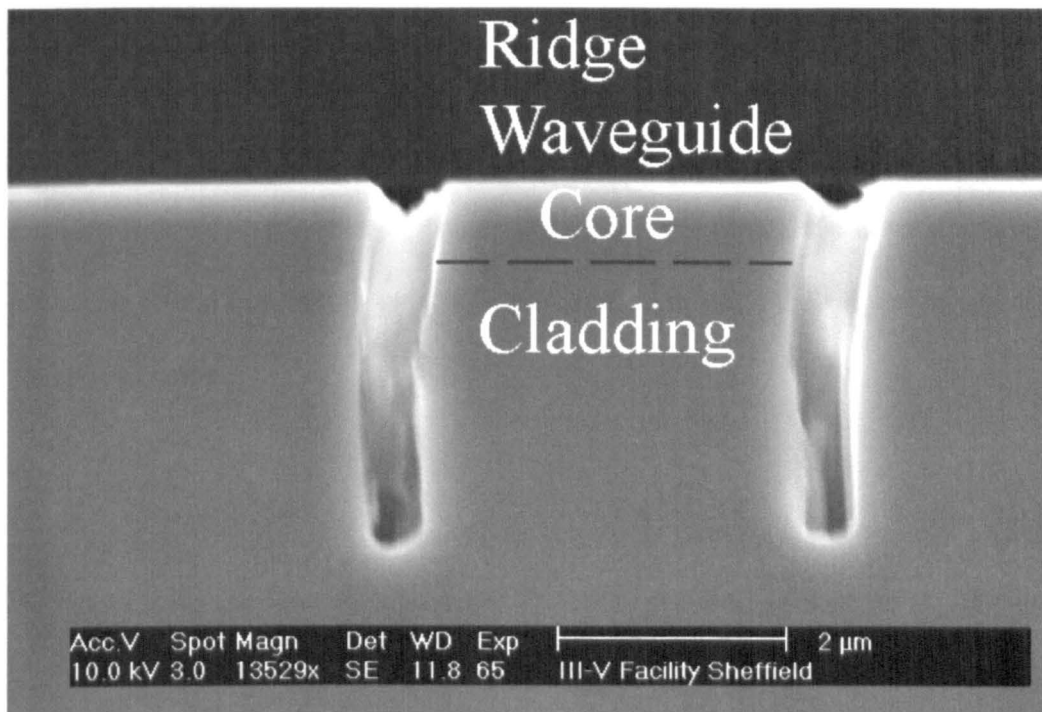


**Figure 3-5** Cross Sectional view of a typical ridge waveguide. The dashed black line indicates the boundary between the core and the cladding (not to scale).

The ridge waveguides in which the photonic crystals are embedded, are processed in a similar way to the photonic crystals themselves. The only difference lies in the accuracy setting of the electron beam lithography process, set to low accuracy for the ridge waveguide, and high for the photonic crystal itself. This is down to time constraints as it would take an inordinate amount of time to write a 1.5 mm long ridge waveguides at high resolution.

In the samples used in this chapter, i.e. photonic crystals embedded in ridge waveguides, light could propagate on the region of semiconductor in between the ridge waveguides containing the photonic crystals, see figure 3-6 b). In order to prevent this from happening, a series of chevrons have been patterned and etched in the same way as the ridge waveguides themselves, see figure 3-6 a). These chevrons behave like light barriers that prevent light from propagating through the semiconductor region between each waveguide. At the semiconductor/chevron interface light will be reflected back due to total internal reflection. This ensures that only light transmitted through the ridge waveguides will be collected.

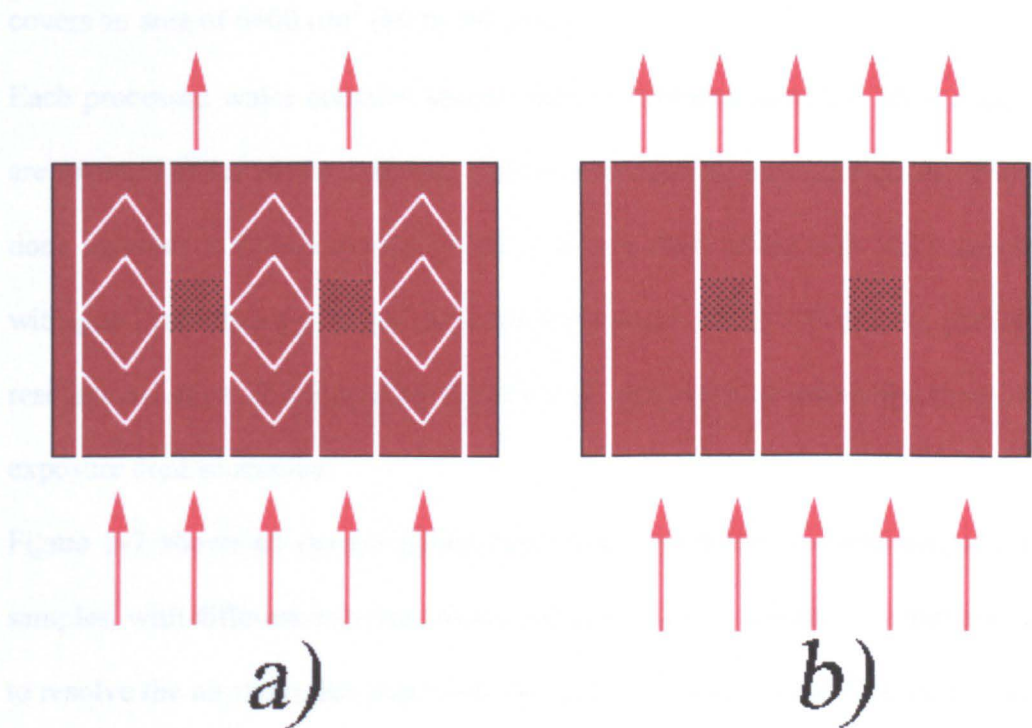


**Figure 3-6** Schematic drawing of a typical sample with several ridge waveguides with a) and without b) chevrons intercalated between the ridge waveguides. The chevrons effectively stop light from propagating.

### **3.2.3 Reflectivity Geometry Samples (1-D Photonic Crystal Waveguides)**

The samples designed for reflectivity measurements, discussed in chapters 4 and 5, are significantly different from the samples used for in-plane transmission measurements, presented in this chapter.

While the processing of the actual photonic crystal is the same regardless of the experimental geometry, the different experimental geometry means that a ridge waveguide is not needed for these samples. Samples processed for reflectivity measurements are square shaped surrounded by a deep air trench, 20  $\mu\text{m}$  in width. The air trench is present to avoid light from the unpatterned wafer being accidentally collected. The photonic crystal used in reflectivity measurements covers an area of  $6400 \mu\text{m}^2$  (80 by 80  $\mu\text{m}$ ).

Each processed wafer contains several dozens different samples. Most samples are exposed twice or three times, with ever increasing exposure doses. This is done in order to obtain a satisfactory exposure dose which will yield samples with good morphology. In practice, most exposure doses will present photonic resonances, even if the quality factors and spectral positions vary from one exposure dose to another.

Figure 3-7 shows an optical photograph of a typical wafer containing several samples, with different exposure doses and periods. The resolution is not enough to resolve the air moat that surrounds the each photonic crystal. The period and, sometimes, the air fill factor are etched above each sample to allow easy identification of the correct sample.

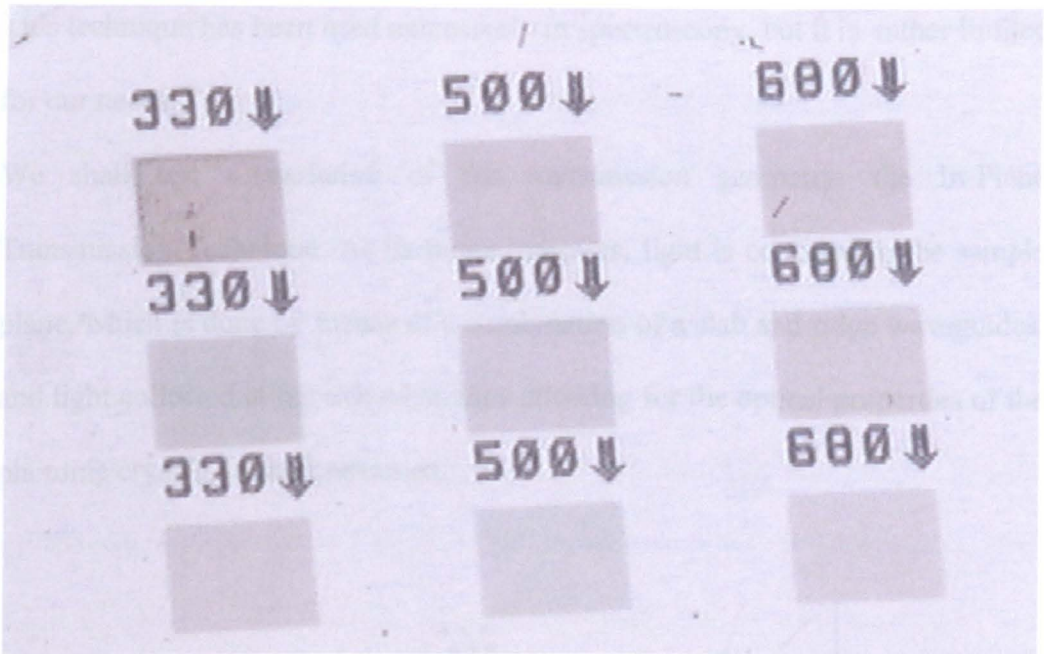


**Figure 3-7** Optical photograph of a typical “reflectivity” wafer. Three different periods, each processed at three different exposure doses are shown.

### 3.3 Linear Characterisation Methods

Investigation of the photonic band structure of a photonic crystal can be achieved by two different types of techniques, namely: Transmission spectroscopic techniques and reflection spectroscopic techniques. Transmission techniques will be discussed in this chapter, whereas reflectivity techniques will be discussed at length on chapter 4.

#### 3.3.1 Experimental Techniques for Transmission Spectroscopy

In transmission spectroscopy light is shone on one side of the sample and collected on the other, thus allowing us to determine where the stop gaps of the photonic crystals are by measuring the transmitted light versus the wavelength.

This technique has been used extensively in spectroscopy, but it is rather limited for our needs.

We shall use a variation of the transmission geometry: the In-Plane Transmission Technique. As its name indicates, light is confined to the sample plane, which is done by means of a combination of a slab and ridge waveguides, and light collected at the exit edge, thus allowing for the optical properties of the photonic crystals to be determined.

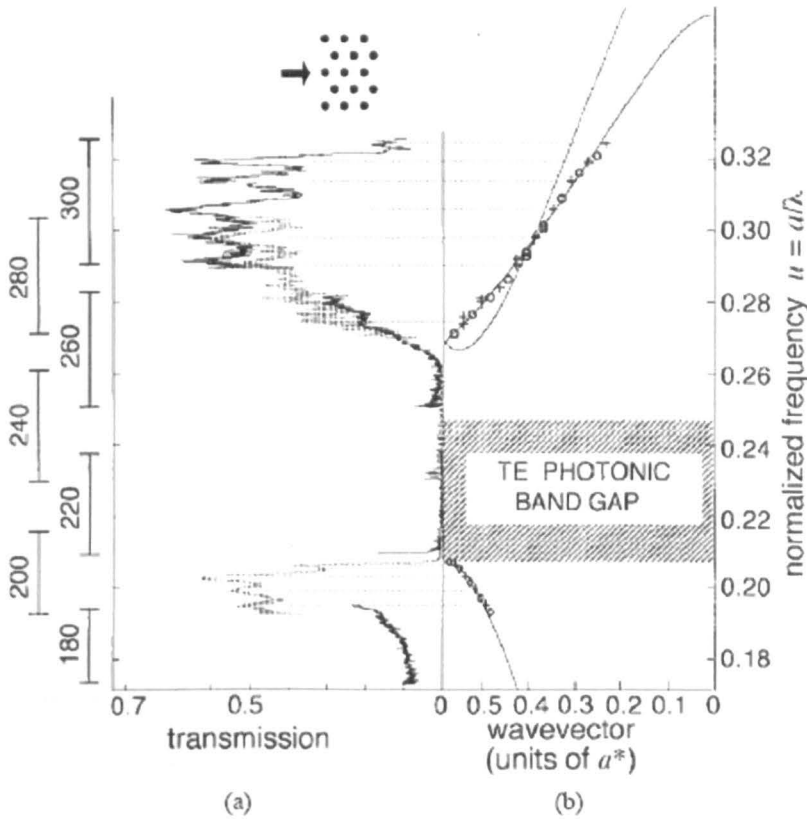


**Figure 3-8 a)** Transmission spectrum of 2D hexagonal lattice photonic crystal for TE polarization along the  $\Gamma$ -K direction **b)** Corresponding photonic band structure. Extracted from reference 5.

A photonic band gap will be accompanied by a reduction of the amount of light transmitted as the diagram in figure 3-8 shows. However the converse is not always true, i.e. a reduction of the transmission does not necessarily mean that there is a photonic band gap at that wavelength<sup>13</sup>.

The probing light used in this technique can either be externally coupled to the sample<sup>14</sup>, or an internal source can be created from the photoluminescence emitted by either quantum dots<sup>15</sup> or quantum wells<sup>16</sup> excited by a laser. The main disadvantage of the internal source approach is the lack of sufficient power from the light source to go into the nonlinear regime; this is why we lack a real choice, if one is to attempt nonlinear experiments. Another disadvantage is the limited emission range offered by quantum dots and quantum wells.

The in-plane transmission geometry allows the study of interesting structures such as point and line defects. The former can be used as a microcavity<sup>17,18</sup> that can be used to obtain low threshold lasers<sup>18</sup> whereas the latter can be used as a waveguide<sup>17,19</sup>, which can be engineered to incorporate bends<sup>20</sup> with radius of the same order of magnitude as the wavelength of operation.

### **3.3.2 Experimental Set-Up and Samples**

The experimental setup used to carry out the in-plane transmission measurements in this chapter, is schematically shown in figure 3-9 (the imaging system is not shown for simplicity). The experimental set-up uses a mode locked Ti:sapphire laser tuneable from 700 nm to 1000 nm with a repetition rate of 80 MHz (Tsunami® by Spectra Physics) and pulses lasting 100 fs. The laser is

monitored by means of a spectrum analyzer connected to an oscilloscope. The output of the laser is vertically polarized; a half wave plate is used to rotate the polarization of the laser beam if and when required. (When the polarization of the laser matches the required polarization, the half wave plate is removed). Light is coupled to the sample by means of a microscope objective lens with an approximate magnification of 60X and  $NA = 0.85$  mounted on a three dimensional micropositioning stage. The sample is mounted on a two dimensional stage, which also features tilting controls. Light is then collected from the sample by means of an objective lens with magnification 40X and  $NA = 0.65$ , again mounted on a three dimensional micropositioning stage. Both objective lenses are sold by Optics For Research. This objective is also used to focus the collected light on to an optic fibre. The optic fibre holder is adjustable in the xy plane, thus simplifying the coupling significantly. The fibre has a dual purpose here; firstly, it acts as a spatial filter, thus ensuring that only light that is coming out of the waveguide and not the surrounding semiconductor or the air above the waveguide is collected and secondly it guides the collected light from the waveguide on to the spectrograph. Light can also be guided using mirrors, but a pinhole is then required, thus making it slightly more complicated than the approach used here. Before hitting the spectrograph, the light is collimated by a plano-convex lens of focal distance  $f = 10$  cm and then focused on to the spectrograph by means of a similar plano-convex lens, both made of BK7 glass. The spectrograph is equipped with charged coupled device acting as a light detector, remotely controlled by a computer. In order to ease the coupling of the

light in and out of the sample, an imaging system is incorporated. This consists of a white light source that illuminates the edge of the sample. On the input side, back reflected light is directed by means of a beam splitter on to an imaging camera, which is plugged into a TV monitor. A similar arrangement incorporating two mirrors is used on the output side. Neither are shown in figure 3-9.

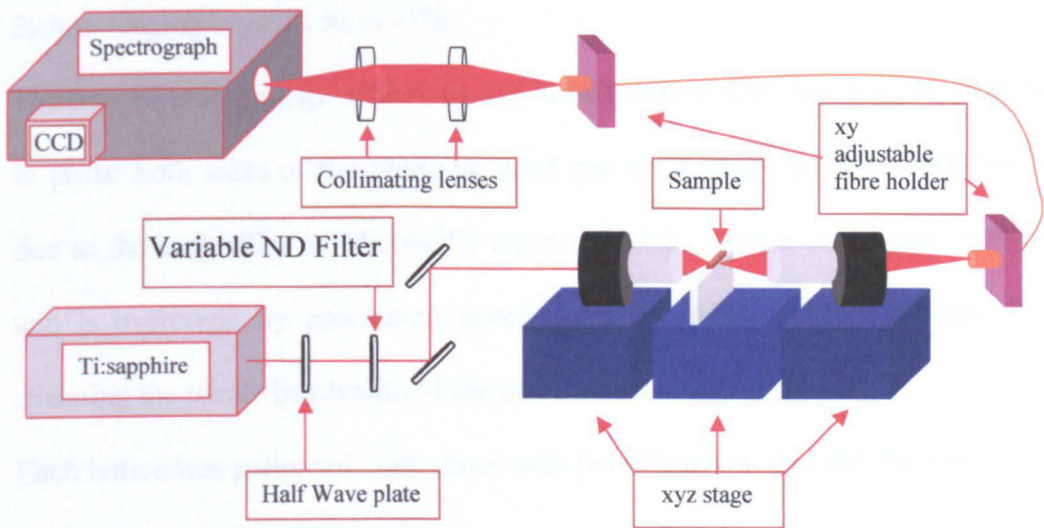


**Figure 3-9** Schematic view of the experimental set-up for in-plane transmission measurements on photonic crystals embedded in ridge waveguides samples.

The sample used for the transmission measurements is the AT218. This is in fact a set of semiconductor chips each containing two different periods as explained in page 56. There are forty ridge waveguides per period. There are two different photonic crystal lengths, namely 4 and 16  $\mu\text{m}$  and for each length there are two different lattice directions,  $\Gamma$ -K and  $\Gamma$ -M, each with ten ridge waveguides, for a total of twenty ridge waveguides per photonic crystal length.

The period, fill factor, lattice direction and crystal length are all etched above each mini-set to unambiguously identify each mini-set.

The core of AT218 consists of a 400 nm thick layer of  $\text{Al}_{0.13}\text{Ga}_{0.87}\text{As}$ , while the cladding is a 2  $\mu\text{m}$  thick layer of  $\text{Al}_{0.60}\text{Ga}_{0.40}\text{As}$ . The samples are etched to an approximate depth of 800 nm. The whole structure has been grown on a 350  $\mu\text{m}$  thick GaAs substrate. The two dimensional lattice is a triangular or hexagonal lattice, with periods ranging from 250 nm to 350 nm in 20 nm steps and air fill factors ranging from 35 % to 41%.

The limited tuning range offered by our laser source means that it is not possible to probe both sides of the photonic band gap on a single sample. Fortunately, due to the scalability of Maxwell's equations, this is not a significant problem and is overcome by processing several samples with different periods, thus spanning the whole bandwidth of the photonic band gap.

Each lattice was patterned eight times with two blank waveguides flanking them. This is done in order to allow measurements that permit us to separate the response of the waveguide from that of the photonic crystal itself by comparing a blank to a photonic crystal containing waveguide. In order to probe both high symmetry directions, i.e.  $\Gamma$ -K and  $\Gamma$ -M, different lattices had to be processed as there is no way of rotating the lattice in a ridge waveguide to access the high symmetry directions.

### **3.3.3. Experimental Results**

In this section the linear properties of the AT218 sample set will be probed. The main objective of this section is to use the in-plane transmission experimental set up, as described above, to observe a photonic band gap. It is expected that the transmission will decrease sharply as the wavelength is tuned into this photonic band gap.

During the measurements the spectrum analyzer is used to check where the laser wavelength is set. The pulse bandwidth is normally set to 10 nm full width half maximum and kept constant as much as possible. This value can be modified, but maintaining the laser mode-locked becomes somewhat of a challenge for smaller widths at the edges of the tuning range.

Once the wavelength has been set, the appropriate waveguide is selected by means of either the in-coupling lens stage or the sample stage, or both. Then using the out-coupling lens stage light is collected from the appropriate waveguide. This is normally trivial, as there is only one waveguide transmitting light due to the chevrons patterned on the sample. Finally light is detected by the detector after it has been dispersed by the spectrograph. A typical output of a blank waveguide is shown in figure 3-10.

Since our laser system lacks the sufficient pulse energy to generate a white light continuum, we are forced to do a step by step characterization of the samples, by changing the laser wavelength and taking a measurement at several wavelengths, normally from 860 nm to 930 nm, at 10 nm intervals.

A piece wise plot of the transmission can be created from the maxima of all the individual transmission spectra at nominally low powers.

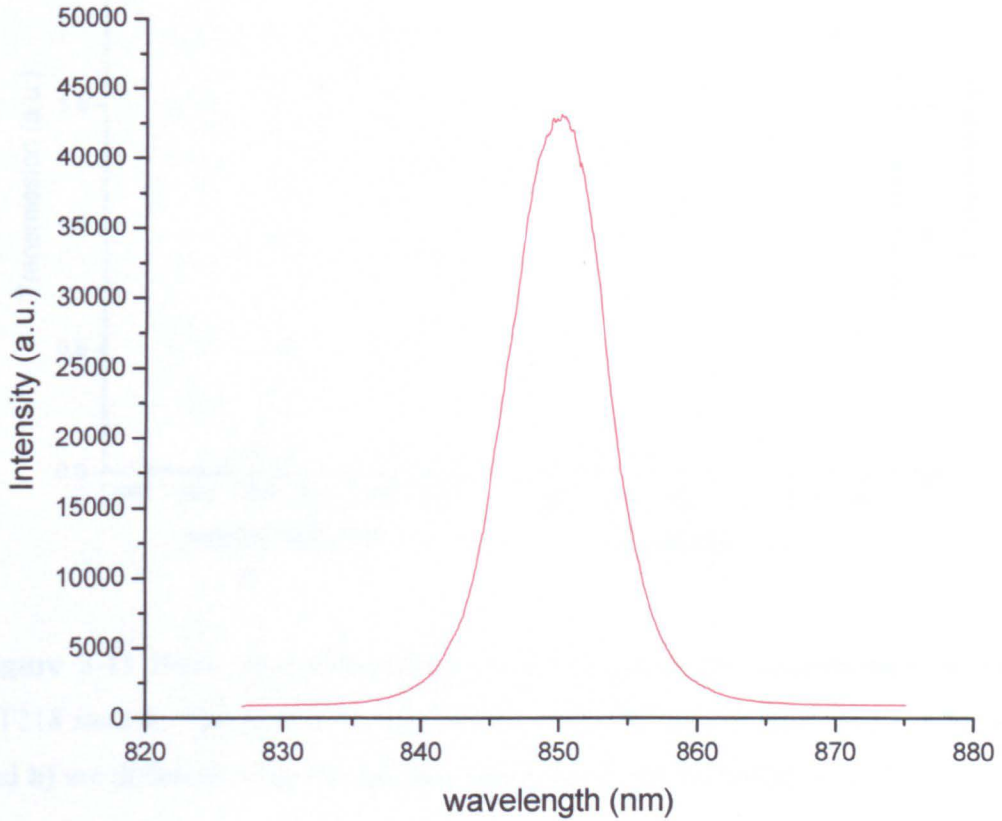


**Figure 3-10** Typical transmission spectra from a blank waveguide (AT218). The laser wavelength is centred at 850 nm and the average laser power is 125  $\mu$ W.

The spectral shape of the transmitted laser pulse can be somewhat misleading as it can deviate somehow from a Gaussian like shape typical of the transmitted spectrum of a blank waveguide. It, nonetheless, portrays a fairly good picture of the transmission properties of every sample. The measurements shown in this thesis are all taken on 4  $\mu$ m long photonic crystals. The lattice orientation is always  $\Gamma$ -K and the polarization is TE unless otherwise stated.

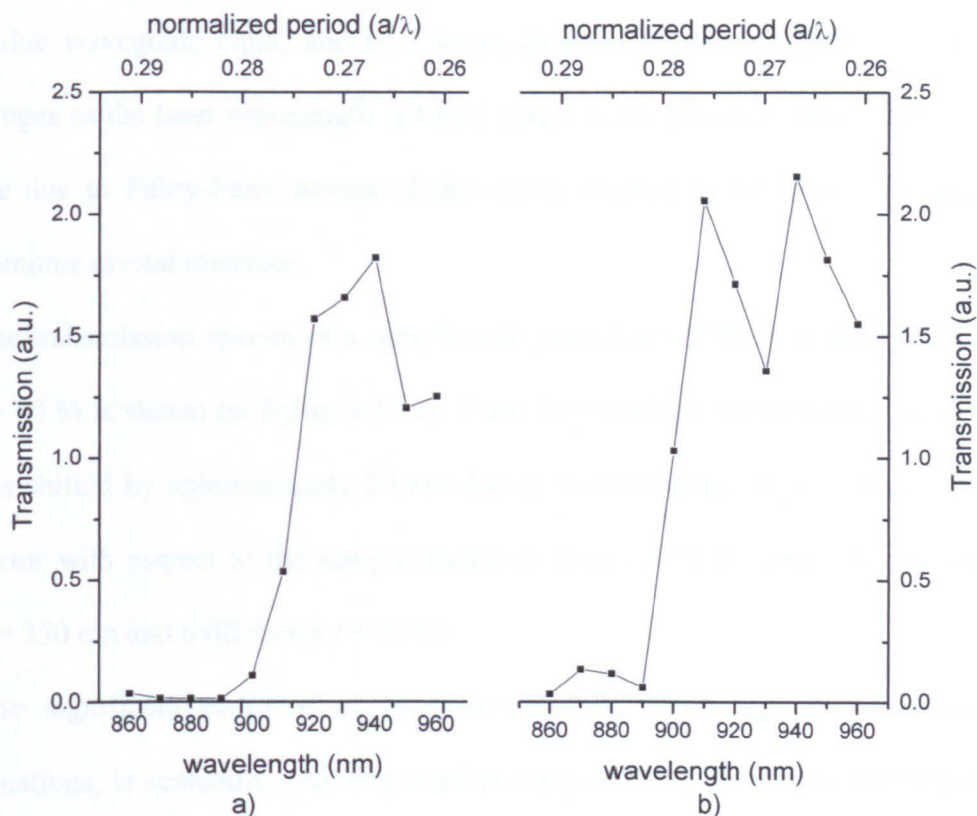


**Figure 3-11** Piece wise composition of the transmission measurement of the AT218 sample. The period is  $a = 250$  nm while the air fill factor is  $f \sim 37\%$ . **a)** and **b)** are different ridge waveguides, numbers 5 and 8 respectively.

Figure 3-11 above, shows a typical piecewise composition of the transmission spectrum of AT218 for a period  $a = 250$  nm for ridge waveguides five and eight, figures 3-11 a) and b) respectively. The transmission drops significantly for centre wavelength of approximately  $\lambda = 910$  nm. This is an edge of the photonic band gap. There is a slight mismatch (about 1%) between the locations of the photonic band edge on both waveguides; this is most likely due to differences on the samples due to the inherent imperfection of the fabrication process. It should be noted that the transmission of these photonic crystals containing ridge waveguides on a passband is approximately 1%.

Ridge waveguide eight, and to a lesser degree, ridge waveguide five, shows fringes as the laser wavelength is tuned closer to the photonic band edge. These are due to Fabry-Perot modes of the cavity created by the ridge waveguide/photonic crystal interface.

The transmission spectra of a sample with period  $a = 270$  nm and air fill factor  $f = 40\%$  is shown on figure 3-12 a). It can be seen how the photonic band edge has shifted by approximately 50 nm due to the difference in period and air fill factor with respect to the sample shown in figure 3-11 b), which had a period  $a = 250$  nm and a fill factor  $f = 37\%$ .

One significant property of photonic crystals, stemming from Maxwell's equations, is scalability. As discussed in section 2.2.1, there is no fundamental length scale. This is demonstrated in figure 3-12 b), where a piecewise composition of the transmission measurement of two different waveguides with different periods, namely ridge waveguide eight from a sample with period  $a = 250$  nm and ridge waveguide seven from a sample with period  $a = 270$  nm, both of the AT218 sample set, have been plotted on the same graph. When the scale is set to normalized wavelength<sup>i</sup>, it can be clearly seen how the photonic band edge lies on the same normalized wavelength. The agreement between both periods is remarkable. This is the sample with the longest period that shows the short normalized wavelength edge of the photonic band gap, i.e. the dielectric band, with our set-up. In order to see the long normalized wavelength edge of the photonic band gap, i.e. the air band, longer periods are required.

---

<sup>i</sup> Normalized wavelength is defined here as  $u = a/\lambda$ .

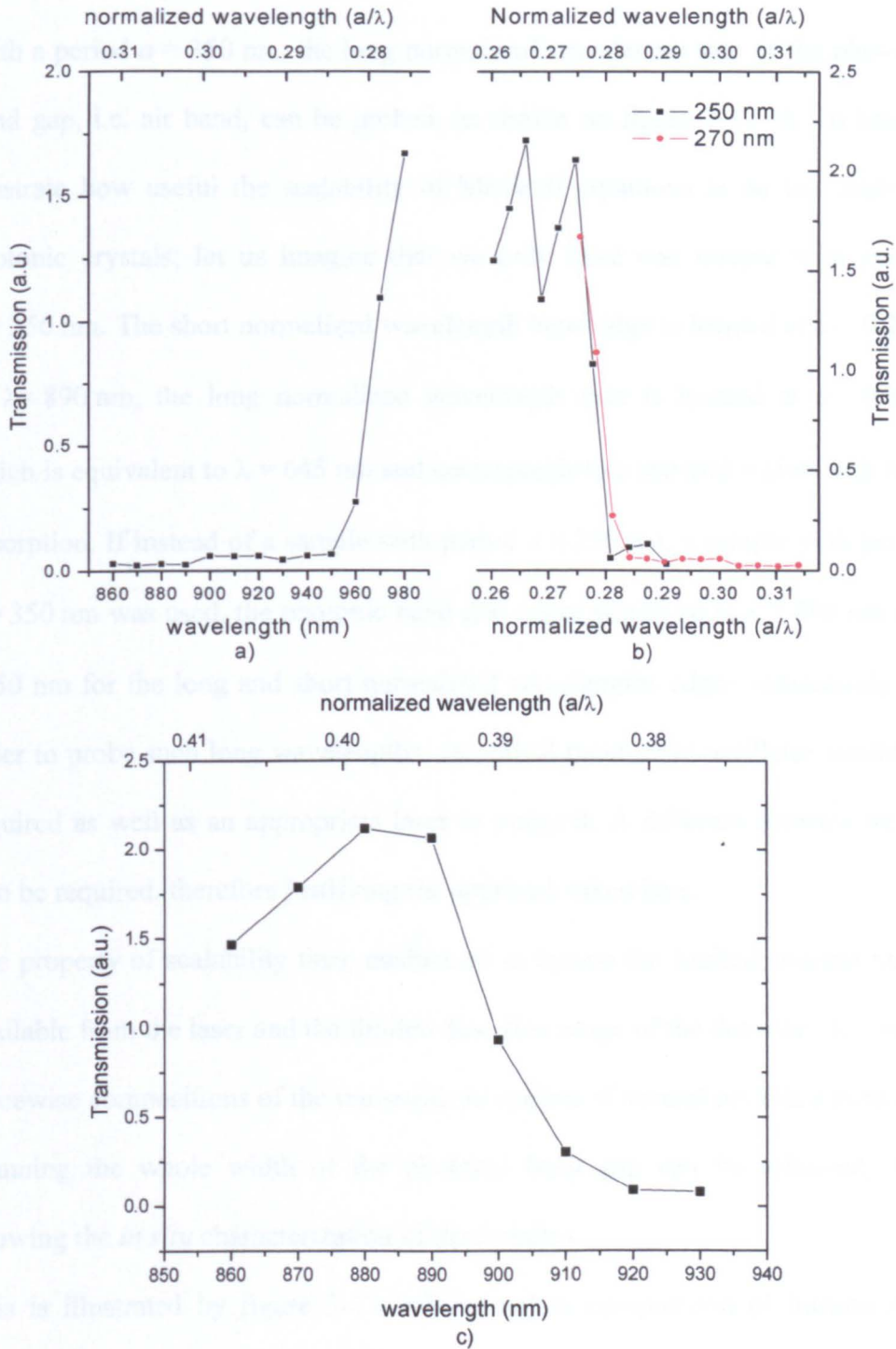


**Figure 3-12** Transmission spectra of AT218. **a)** The period is  $a = 270$  nm, air fill factor  $f = 40\%$ , waveguide 7. **b)** Comparison of transmission spectra for periods 250 and 270 nm respectively, waveguides 8 and 7 respectively. **c)** The period is  $a = 350$  nm and the air fill factor  $f = 39\%$  waveguide 8

With a period  $a = 350$  nm, the long normalized wavelength side of the photonic band gap, i.e. air band, can be probed, as shown on figure 3-12 c). To further illustrate how useful the scalability of Maxwell equations is on the study of photonic crystals; let us imagine that we only have one sample with period  $a = 250$  nm. The short normalized wavelength band edge is located at  $u = 0.274$ , or  $\lambda = 890$  nm, the long normalized wavelength side is located at  $u = 0.388$ , which is equivalent to  $\lambda = 645$  nm and corresponds to a spectral region with high absorption. If instead of a sample with period  $a = 250$  nm, a sample with period  $a = 350$  nm was used, the photonic band gap edges would be at  $\lambda = 890$  nm and 1250 nm for the long and short normalized wavelengths edges respectively. In order to probe such long wavelengths, an optical parametric oscillator would be required as well as an appropriate laser to pump it. A different detector would also be required, therefore justifying the approach taken here.

The property of scalability thus, enables us to bypass the limited spectral range available from the laser and the limited detection range of the detector. By using piecewise compositions of the transmission spectra of several periods a snapshot spanning the whole width of the photonic band gap can be achieved, thus allowing the *in situ* characterization of the samples.

This is illustrated by figure 3-13, where such a composition of transmission spectra has been created by plotting together the piecewise composition of all the periods available, i.e.  $a = 250 - 350$  nm

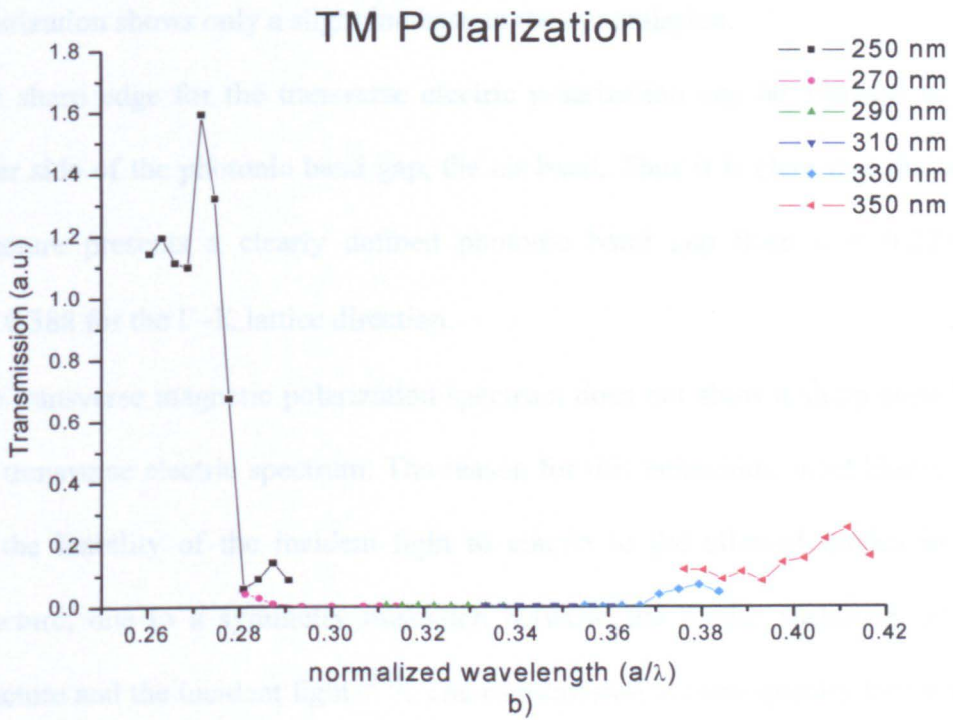
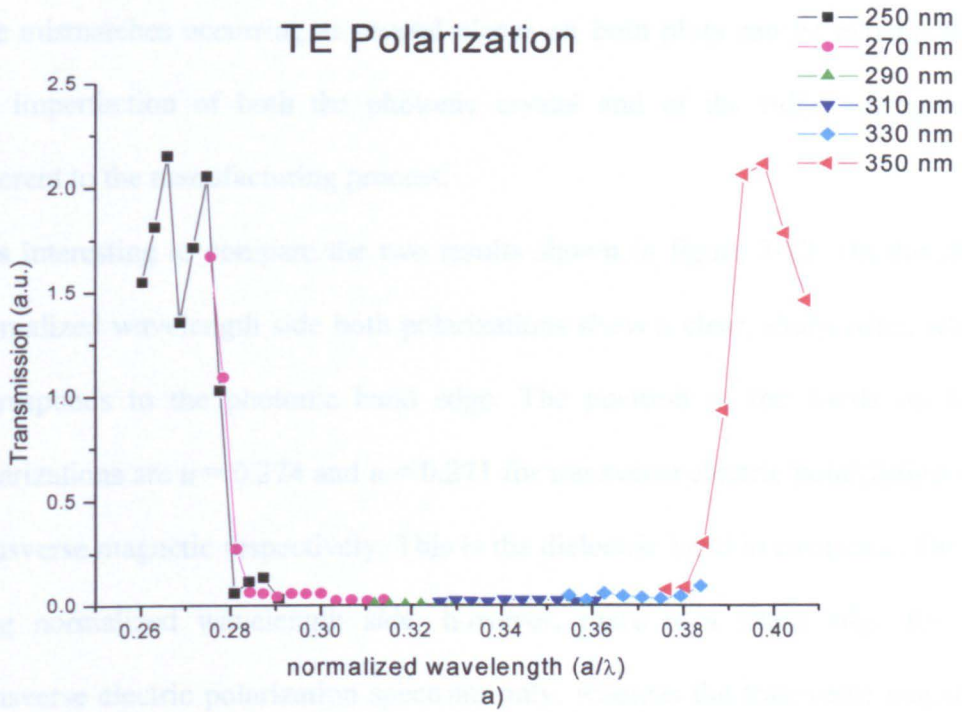


**Figure 3-13** AT218 sample transmission spectrum composed from the transmission spectra of periods  $a = 250\text{-}350$  nm. The polarization is TE and TM for a) and b) respectively.

The mismatches occurring at several places on both plots can be explained by the imperfection of both the photonic crystal and of the ridge waveguides, inherent to the manufacturing process.

It is interesting to compare the two results shown in figure 3-13. On the short normalized wavelength side both polarizations show a clear, sharp edge, which corresponds to the photonic band edge. The position of the bands on both polarizations are  $u = 0.274$  and  $u = 0.271$  for transverse electric polarization and transverse magnetic respectively. This is the dielectric band in each case. On the long normalized wavelength side, however, there is a sharp edge for the transverse electric polarization spectrum only, whereas the transverse magnetic polarization shows only a slight increase in the transmission.

The sharp edge for the transverse electric polarization can be ascribed to the other side of the photonic band gap, the air band. Thus it is clear that the band structure presents a clearly defined photonic band gap from  $u = 0.274$  to  $u = 0.388$  for the  $\Gamma$ -K lattice direction.

The transverse magnetic polarization spectrum does not show a sharp edge like the transverse electric spectrum. The reason for this behaviour, most likely, lies on the inability of the incident light to couple to the allowed modes in the structure, due to a symmetry mismatch between the modes sustained by the structure and the incident light<sup>13,21</sup>. The transmission is consequently lower than what would be expected. The range affected starts at around  $u = 0.37$ , where an increase in the transmitted light begins, and continues all the way to  $u = 0.42$  and possibly beyond. The amount of transmitted light is somewhat higher than on

the band gap region. This is due to the fact that the crystal is not infinite in size and therefore the symmetry mismatch is broken to some degree.

### **3.4. Introduction to Nonlinear Measurements on Photonic Crystal Ridge Waveguides**

In this section the nonlinear properties of the AT218 sample set will be explored. The main objective of this section is to see a shift and broadening, or narrowing, of the photonic band gap. This shift is caused, as discussed in sections 2.3 and 2.4, by a change in the refractive index induced by excited carriers, whether virtual or real. The nonlinear properties of the ridge waveguide itself will be studied as well as the photonic crystal ridge waveguide system.

An attempt to separate the response of the photonic crystal from that of the ridge waveguide was made, however it proved unsuccessful. The reasons for this lack of success will be discussed.

A successful attempt to change the refractive index via photo excitation of carriers will be discussed in chapters 4 and 5.

#### **3.4.1. Nonlinear Measurements in Photonic Crystal Waveguides**

The experimental set-up used is the same set-up as used to carry out the linear characterization of the samples. The nonlinear measurements only involve changing the coupling power to reach the nonlinear regime, which can be easily accomplished by changing the laser attenuation with the neutral density filter wheel, as shown in figure 3-9

The work carried out by M.D. Rahn *et al.* (reference 1) is very similar to the work presented here. The main difference resides in the samples, which not only are of a different material, but have a different design. In reference 1, symmetric and asymmetric spectral narrowing was observed for blank and photonic crystal waveguides respectively. This was attributed to self phase modulation and two photon absorption coupled with small amounts of chirp in the overall optical system. Two photon absorption induced optical limiting was also reported. The overall nonlinear response of the samples was dominated by the ridge waveguide and the nonlinear response of the photonic crystal itself was very small, due to the low intensity that reached the photonic crystal. This was due to the length of the ridge waveguide, approximately 0.75 mm long on each side of the photonic crystal, compared to the 4  $\mu\text{m}$  long photonic crystal, which means, that the pulses would have propagated through approximately 0.75 mm of  $\text{Al}_{0.13}\text{Ga}_{0.87}\text{As}$  before reaching the actual photonic crystal.  $\text{Al}_{0.13}\text{Ga}_{0.87}\text{As}$  has a non negligible nonlinear refractive index  $n_2 = 4 \cdot 10^{-13} \text{ cm}^2 \text{ W}^{-1}$  at  $\lambda = 900\text{nm}$ . This fact, along with, the very high intensities, due to the tight focusing required to couple the laser beam into the waveguide, mean that it is very possible that any nonlinear response from the photonic crystal will be dwarfed by that of the ridge waveguide. The length of the waveguide after the photonic crystal is not critical as the intensity of the light beam reaching this waveguide is not enough to go into the nonlinear regime.

In the light of the results presented in reference 1, there is a big question mark over this experimental setup as a valid method for measuring the nonlinear

response of our photonic crystal ridge waveguides samples. This is an intrinsic problem of our samples which can be solved either at the manufacturing level, by making either longer photonic crystals and/or shorter waveguides, or at the experimental level, by using a different experimental set-up.

Let us concentrate first on the sample design. The first idea, namely, lengthening the photonic crystal has a main drawback, and that is fabrication time. It would take an inordinate amount of time to create a photonic crystal of comparable size to the waveguide itself. While a longer photonic crystal, around 50  $\mu\text{m}$ , is feasible. These would not only suffer huge transmission losses, but their nonlinear response would almost certainly still be dwarfed by that of the ridge waveguide. The second idea, namely to shorten the ridge waveguide, is not without its drawbacks either, as leaving the photonic crystal closer to the edge increase the probability of damage when cleaving.

This was verified by using a shorter ridge waveguide, approximately 1 mm long, instead of the usual 1.5 mm. The embedded photonic crystals were patterned to be as long as 50  $\mu\text{m}$  and were placed at approximately 0.1 mm from one of the edges. Unfortunately, this distance proved not to be long enough and the sample was damaged beyond use during the cleaving process.

For these reasons it was eventually decided to take the second approach and design a different experimental set-up. This will be described in section 3.4.3. First experimental results for longitudinal pumping similar to the experiment of Rahn *et al* will be discussed.

### 3.4.2. Experimental Results

In this section a set of nonlinear measurements for blank and photonic ridge waveguides will be presented. It will be shown that the response of the blank ridge waveguide is very interesting as it becomes nonlinear at high intensities, showing spectral narrowing, optical limiting and negative differential transmission. Similar effects are observed in photonic ridge waveguides. The spectral narrowing shown by photonic crystal ridge waveguides is markedly different from that shown by blank ridge waveguides; the former being asymmetric while the latter is symmetric.

The nonlinear optical response of blank waveguides was measured first. While these waveguides do not contain photonic crystals, they are made of  $\text{Al}_{0.13}\text{Ga}_{0.87}\text{As}$  which as discussed in the previous section will behave nonlinearly at high enough intensities. The laser polarization is set to TE polarization throughout this section.

Figure 3-14 shows the spectrum transmitted through a blank waveguides for different input intensities. The first noticeable effect is a spectral narrowing of the pulses as the input intensity is increased from  $1 \text{ GW}\cdot\text{cm}^{-2}$  to  $87.6 \text{ GW}\cdot\text{cm}^{-2}$ . The average power ranges from  $125 \mu\text{W}$  to  $10 \text{ mW}$  and the laser pulse width is 100 femtoseconds. The laser spot radius is taken to be  $r = 0.5 \mu\text{m}$ , which seems a reasonable figure for a ridge waveguide etched to approximately 900 nm. It should be noted that the coupling coefficient is quite low,  $c_c \sim 4\%$ , but sensible for a ridge waveguide of these dimensions. Furthermore the observed spectral narrowing seems to be fairly symmetric as can be seen in figure 3-14.

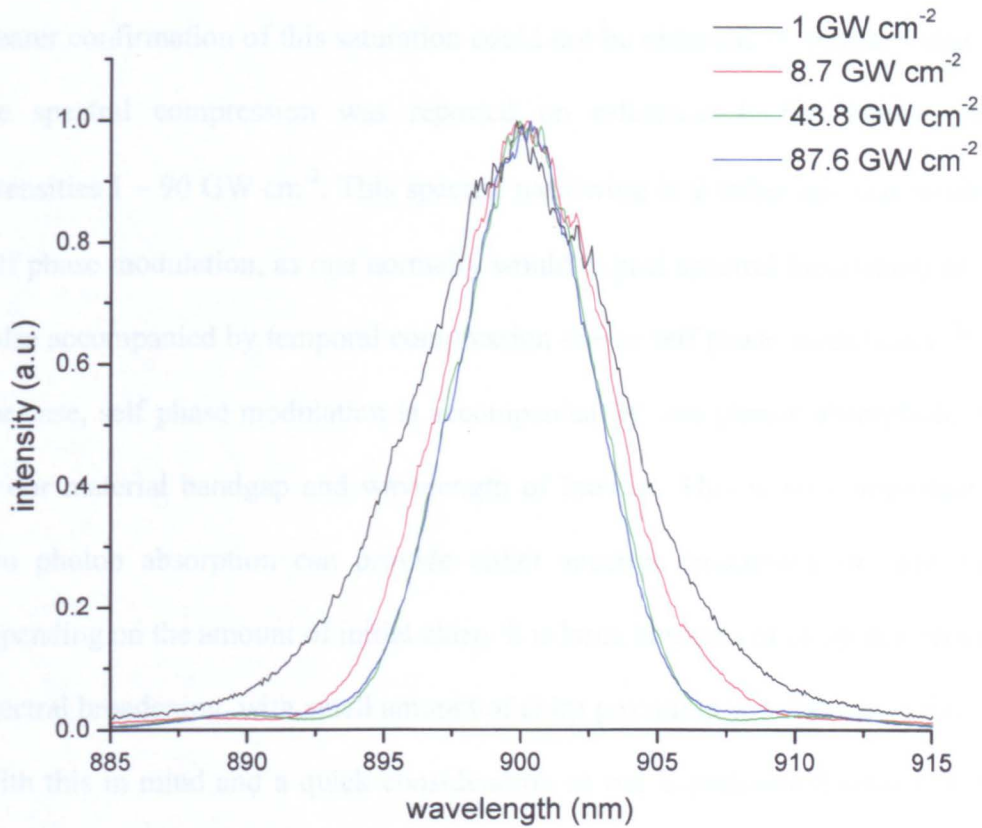


**Figure 3-14** Transmitted spectra for different input intensities for AT218. The waveguide is a blank ridge waveguide containing no photonic crystal. Ridge waveguide number 10 of the 350 nm period  $\Gamma$ -K  $4\mu\text{m}$  set. Laser wavelength is centred at  $\lambda = 900$  nm.

The spectral narrowing can be as large as 39 %, when measured at its full width half maximum value, for an input intensity of  $I = 87.6 \text{ GW}\cdot\text{cm}^{-2}$ . Interestingly, the spectral compression of the pulse is approximately 38% at full width half maximum for an intensity  $I = 43.8 \text{ GW}\cdot\text{cm}^{-2}$ . This suggests that further increases in intensity will not result in any increases in the compression of the pulse suggesting some saturation of the process. Unfortunately, further increases of the

intensity (values above  $87.6 \text{ GW}\cdot\text{cm}^{-2}$ ) appeared to damage the waveguide, so a clearer confirmation of this saturation could not be obtained. A similar value for the spectral compression was reported on reference 1, for similar input intensities  $I \sim 90 \text{ GW}\cdot\text{cm}^{-2}$ . This spectral narrowing is a rather unusual result of self phase modulation, as one normally would expect spectral broadening of the pulse accompanied by temporal compression due to self phase modulation<sup>1,22</sup>. In our case, self phase modulation is accompanied by two photon absorption, due to our material bandgap and wavelength of interest. This is very important as two photon absorption can provide either spectral broadening or narrowing depending on the amount of initial chirp. It is large amounts of chirp that provide spectral broadening, with small amount of chirp providing spectral narrowing<sup>1</sup>. With this in mind and a quick consideration of our experimental set-up, which only presents the coupling lens as a major source of chirp before the pulse enters the sample. Two photon absorption coupled with self phase modulation and the small initial chirp lead to a symmetric spectral narrowing, as can be quite clearly seen in Figure 3-14.

Figure 3-15 shows a typical output power versus input power plot. Negative differential transmission<sup>23,24</sup> is observed in addition to optical limiting<sup>25</sup>. It is interesting to see how the output power is approximately linear up to 1 mW input power, it then becomes sublinear as the input power increases up to 5 mW and finally decreases for higher powers ( $>5 \text{ mW}$ ). The reduction at the highest input power is roughly 40 % of the plateau value.

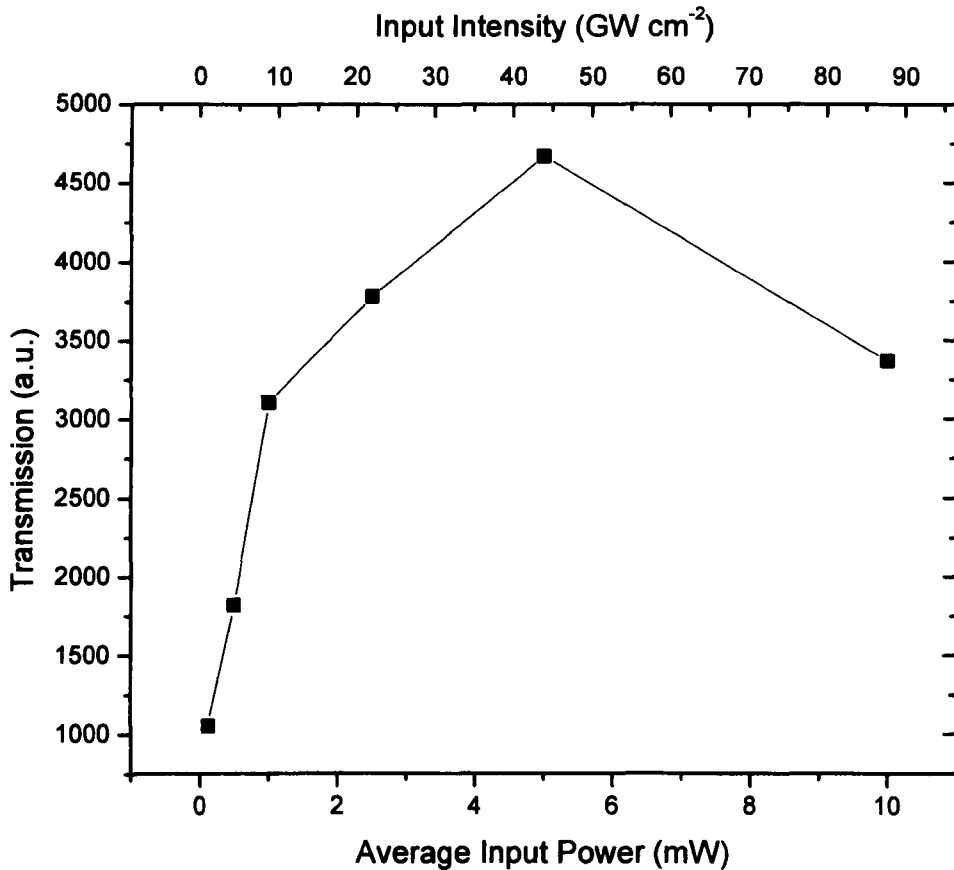


**Figure 3-15** AT218 Transmitted laser power versus input power plot. The ridge waveguide is a blank waveguide. Ridge waveguide number 1 of the 350 nm period  $\Gamma$ -K 4  $\mu\text{m}$  set. Centre wavelength is  $\lambda = 870$  nm.

Cowan *et al* have reported a decrease of the amount of light transmitted, with increasing power, to be as high as five times<sup>23</sup>. This behaviour is attributed to the combined effects of both two photon absorption and free carrier absorption<sup>24</sup>. The free carriers are generated through two photon absorption. At low intensities, the effect of two photon absorption dominates due to the smaller density of free carriers but at higher intensities, with a larger free carrier density, free carrier absorption dominates and is responsible for the decrease in the

transmission. This differential negative transmission effect is reported, in reference 23, to require at least a 200  $\mu\text{m}$  long waveguide, this is shorter than the ridge waveguides used in the AT218 sample set (ridge waveguides length  $\sim 1500 \mu\text{m}$ ) and therefore negative differential transmission is observed.

A study of the transmitted power versus input power for different wavelengths reveals negative differential transmission at different wavelengths, see figure 3-16.

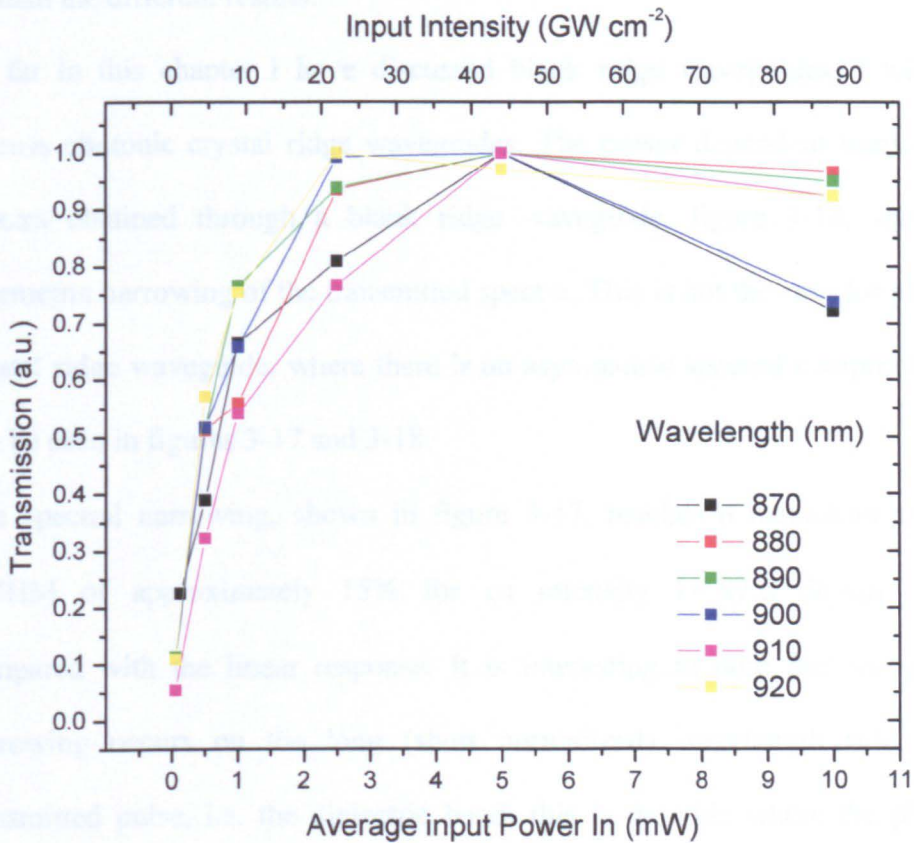


**Figure 3-16** AT218 Power input versus power output for a centre wavelength ranging from  $\lambda = 870\text{-}920\text{nm}$ . Ridge waveguide number 1 of the 350 nm period  $\Gamma\text{-K}$  4  $\mu\text{m}$  set.

Figure 3-16 clearly shows that negative differential transmission occurs for the whole range of investigated wavelengths, namely from  $\lambda = 870$  nm to 920 nm. The reduction in the transmission ranges from: little more than 3%, for a centre wavelength of  $\lambda = 880$  nm, to almost 40 %, for centre wavelengths of  $\lambda = 870$  nm and 900 nm. The data in figure 3-16 shows no clear dependence of the reduction in the transmission with input wavelength. The difference in coupling efficiency for the different wavelengths along with disparities in the input power might explain the different results.

So far in this chapter I have discussed blank ridge waveguides, I will now discuss photonic crystal ridge waveguides. The power dependent transmission spectra obtained through a blank ridge waveguide, figure 3-14, showed a symmetric narrowing of the transmitted spectra. This is not the case for photonic crystal ridge waveguide, where there is an asymmetric spectral compression, as can be seen in figures 3-17 and 3-18.

The spectral narrowing, shown in figure 3-17, reaches a maximum value at FWHM of approximately 15% for an intensity  $I = 87.6 \text{ GW}\cdot\text{cm}^{-2}$ , when compared with the linear response. It is interesting to note that the spectral narrowing occurs on the long (short normalized) wavelength side of the transmitted pulse, i.e. the dielectric band; this is the side where the photonic band edge is.

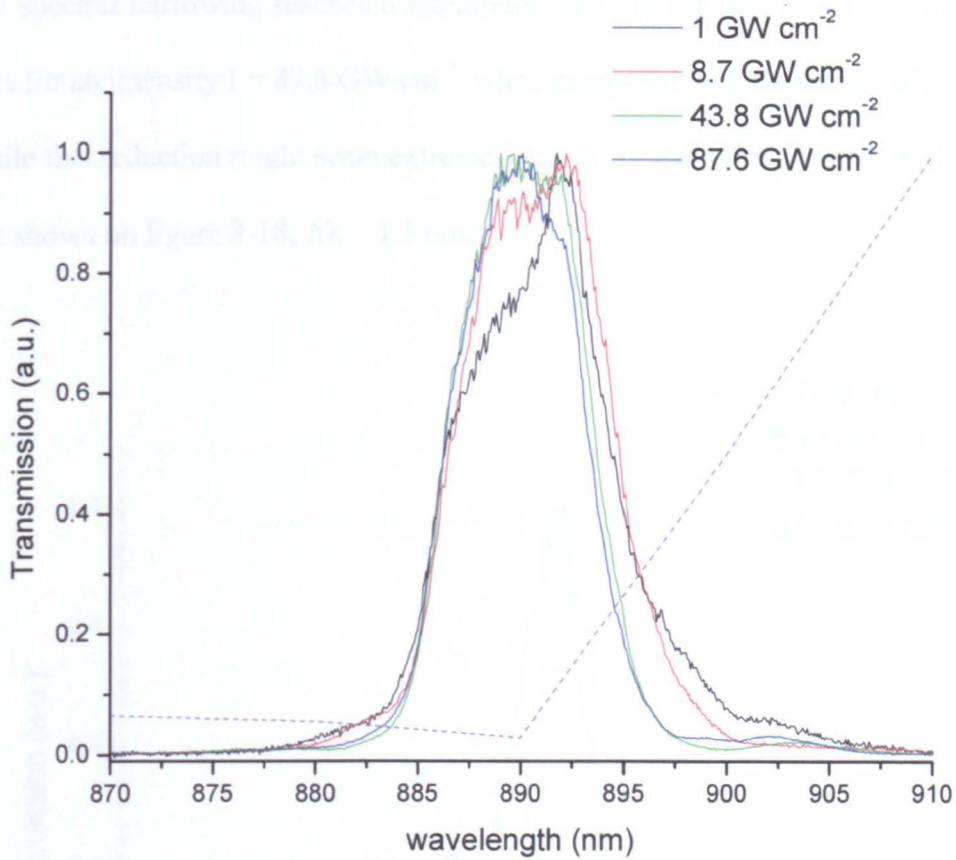


**Figure 3-17** AT218 Spectral power dependence for a photonic crystal ridge waveguide. Ridge waveguide number 8 of the 250 nm period  $\Gamma$ -K  $4\mu\text{m}$  set. The laser wavelength is centred at  $\lambda = 890$  nm. The dashed violet line represents the normalized transmission of the sample.

Figure 3-18 shows a similar plot to figure 3-17, but this time it is the short (long normalized) wavelength edge of the photonic band gap that is being probed as opposed to the long normalized one, i.e. the air band as opposed to dielectric band. Again an asymmetric spectral narrowing occurs, but this time the spectral narrowing occurs on the short (long normalized) wavelength side of the transmitted laser pulse, but this is perhaps not surprising as the photonic band edge is on that side.

The spectral narrowing reaches a maximum value at FWHM of approximately 60% for an intensity  $I = 87.6 \text{ GW}\cdot\text{cm}^{-2}$ , when compared with the linear response. While this reduction might seem extremely large, in real terms is very similar to that shown on figure 3-18,  $\Delta\lambda \sim 1.3 \text{ nm}$ .

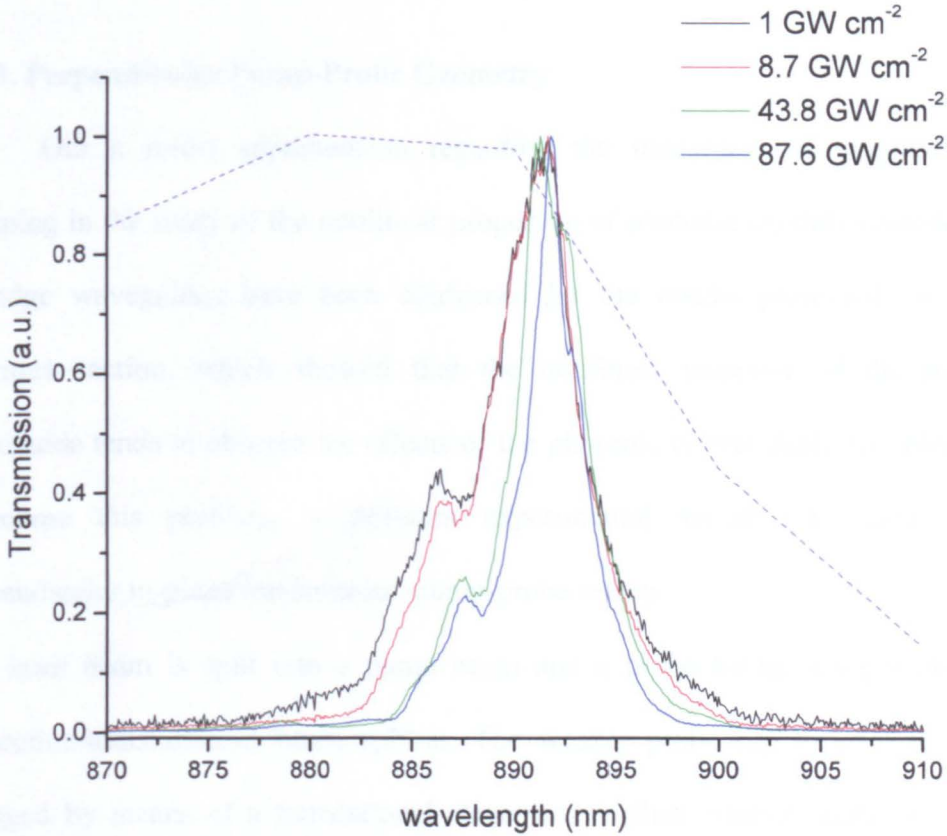


**Figure 3-18** AT218 Spectral power dependence for a photonic crystal ridge waveguide. Ridge waveguide number 9 of the 350 nm period  $\Gamma$ -K  $4\mu\text{m}$  set. The laser wavelength is centred at  $\lambda = 890 \text{ nm}$ . The dashed violet line represents the normalized transmission of the sample.

The origin of the asymmetric narrowing of the transmitted pulse is similar to the symmetric narrowing in blank waveguides, but the photonic crystal acts as a

spectral filter that reduces the power of the pulse on one side of the pulse. This reduced power in one side of the pulse means that no spectral narrowing occurs on this side, while the other side of the pulse, with its higher intensity, is spectrally compressed, resulting in an asymmetrically compressed pulse. This was observed by Rahn *et al* on the dielectric band edge of the photonic bandgap.

### **3.4.3. Perpendicular Pump-Probe Geometry**

Our a priori apprehension regarding the usefulness of longitudinal pumping in the study of the nonlinear properties of photonic crystals embedded in ridge waveguides have been confirmed by the results presented on the previous section, which showed that the nonlinear response of the ridge waveguide tends to obscure the effects of the photonic crystal itself. In order to overcome this problem, a different experimental set-up was used; the perpendicular in-plane transmission pump-probe set-up.

The laser beam is split into a pump beam and a probe beam, using a 30/70 (reflection/transmission) beam splitter. The weaker probe has its path length changed by means of a translational stage, and is then steered, using several mirrors into the coupling microscope objective, through the sample and then collected onto a detector. This part of the experimental set-up is identical to that used in the previous set-up, see figures 3-9 and 3-19.

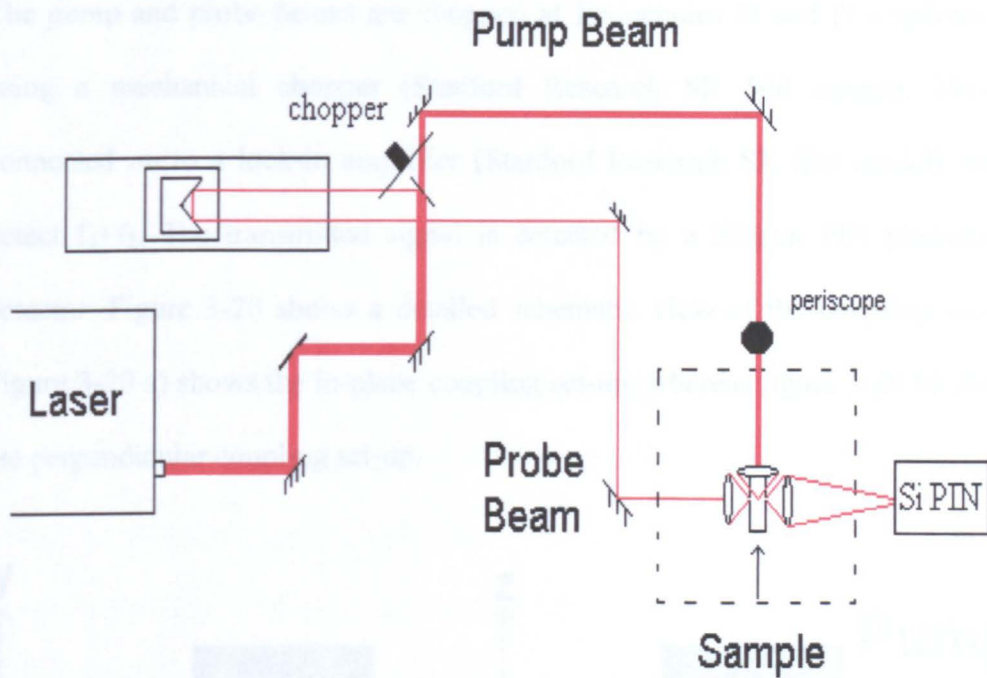


**Figure 3-19** Schematic view of the experimental set-up as laid out on the optical bench. The thin red line represents the probe beam, while the thick red line represents the pump beam.

The strong pump beam is raised by means of a periscope and the focused on to the top surface of the sample using a long working distance objective lens from Nikon; a long working distance is critical because the objective lenses used for coupling the probe in and out of the sample are very close to it, thus making it impossible to get closer to the sample than one centimetre. The magnification is 50X and  $NA = 0.45$ . The objective lens is mounted on a three dimensional stage, to allow accurate micro positioning of the pump beam on to the sample. An imaging system is also set up so that the top of the sample can also be seen, as well as the side. This is critical, as accurate micro positioning of the pump beam is crucial to be able to pump the photonic crystal only.

The pump and probe beams are chopped at frequencies  $f_1$  and  $f_2$  respectively, using a mechanical chopper (Stanford Research SR 540 model). This is connected on to a lock-in amplifier (Stanford Research SR 830 model) set to detect  $f_1+f_2$ . The transmitted signal is detected by a Silicon PIN photodiode detector. Figure 3-20 shows a detailed schematic view of the coupling set-up. Figure 3-20 a) shows the in-plane coupling set-up, whereas figure 3-20 b) shows the perpendicular coupling set-up.

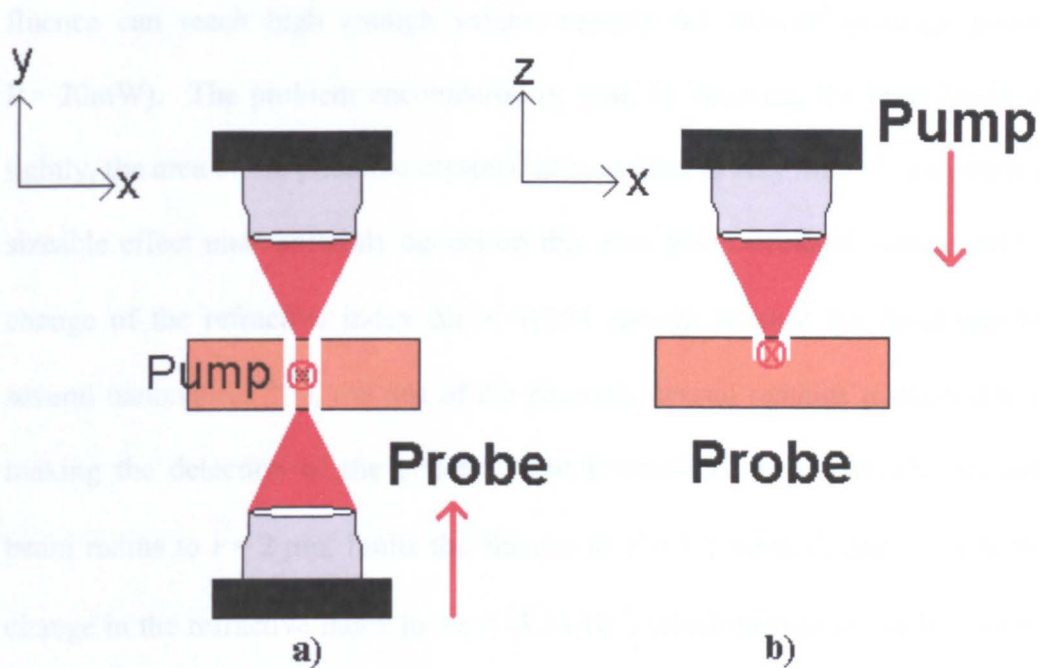


**Figure 3-20** Schematic view of the in-plane transmission perpendicular pump probe set-up. a) Top view. The pump coupling lens is not shown for clarity. b) Side view with the probe coupling lenses omitted for clarity. The probe is directed perpendicular to the plane of the page.

While the set-up is designed to be used for degenerate pump-probe measurements, non degenerate pump-probe can also be used by doubling the pump beam after it has been split by means of a doubling crystal.

Despite many different attempts, it was not possible to observe any nonlinear changes in the transmission in any of the samples tried. While there is evidence of nonlinear interaction, there is nothing to suggest a nonlinear change in the refractive index due to the optical Kerr effect or more probably due to two photon absorption.

The reason why no nonlinear effect was observed was the lack of enough fluence from the laser. For a very tightly focused pump beam,  $r = 1 \mu\text{m}$ , the fluence can reach high enough values, namely  $4.5 \text{ mJ/cm}^2$  (average power  $P = 20\text{mW}$ ). The problem encountered is, that, by focusing the laser beam so tightly, the area of the photonic crystal that is excited is very limited, and while a sizeable effect must certainly occur on this area (the calculated values yield a change of the refractive index  $\Delta n = -0.054$  enough to shift the band gap by several nanometres<sup>26,27</sup>), the rest of the photonic crystal remains unexcited thus making the detection of the effect all but impossible. Increasing the focused beam radius to  $r = 2 \mu\text{m}$ , limits the fluence to  $F = 1.1 \text{ mJ/cm}^2$ , this reduces the change in the refractive index to  $\Delta n = -3.24 \cdot 10^{-3}$ , which proves not to be enough for a detectable effect. This is not surprising as a similar experiment<sup>26</sup> on a similar material system only yielded a nonlinear shift  $\Delta\lambda = 1 \text{ nm}$ , for a change in the refractive index almost twice as large, namely,  $\Delta n = -6.056 \cdot 10^{-3}$ <sup>27</sup>.

The lack of fluence from the laser is the ultimate damper on achieving a nonlinear shift of the band gap edge.

An attempt to overcome these difficulties is planned to take place in the near future. A white light continuum will be generated by a photonic crystal fibre,

which boasts a reduced continuum threshold, approximately  $2nJ$ , which is well within the energy range of the laser system. An added advantage of using a white light continuum is that it will be possible to continuously probe the photonic band structure in a single measurement in sharp contrast to the piece wise composition used in this thesis which was quite time consuming.

### 3.5 Conclusions

Using an in plane transmission set-up, a limited portion of the photonic band structure of the sample, AT218 was characterised. The limited spectral range extends from  $u = 0.26$  to  $u = 0.42$ , which was sufficient to find a photonic band gap. Owing to the limitations in our experimental equipment, namely the tuning range of the laser system used, several samples were used to produce a meaningful picture of the sample transmission profile. This was possible due to the scalability naturally embedded in Maxwell's equations.

Measurements were taken for different lattices in order to probe the two high symmetry directions possessed by a two dimensional crystal with a triangular lattice. No results have been presented for the  $\Gamma$ -M symmetry direction as this direction lacked a photonic band gap in the probed range for either polarization.

The transmission profile of the sample for the other high symmetry direction, i.e.  $\Gamma$ -K, is markedly different for the two possible polarizations. For the transverse electric polarization, the transmission profile shows two clear and sharp drops of transmission at the band edges  $u = 0.274$  and  $u = 0.388$  respectively, which are indicative of a photonic band gap for that polarization between those values.

This is not the case for transverse magnetic polarization, where there is a sharp edge on the short normalized wavelength side at  $u = 0.271$ , but there is not a sharp edge on the long normalized wavelength side. This is most likely due to a symmetry mismatch between the parity of the incoming beam and that of the photonic band. This symmetry mismatch is responsible for the low value of the transmission from  $u = 0.37$  to  $u = 0.42$  and very possibly at longer normalized wavelengths.

Despite the symmetry mismatch, some light does couple to the photonic band. This is due to the finite size of the crystal, which allows some coupling to the photonic band as the symmetry mismatch is not complete.

The first conclusion that can be reached from the set of nonlinear experiments carried out, is that in the nonlinear regime, the response of the photonic crystal was mostly dwarfed by the response of the long waveguide that the laser beam sees before interacting with the photonic crystal.

Optical limiting was observed. This is due to two photon absorption, which becomes important at high intensities. However, more interestingly, negative differential transmission was also observed at higher intensities. This behaviour was attributed to the combined effect of free carrier absorption and two photon absorption. The two photon absorption generated free carriers induce absorption in the ridge waveguide. This effect becomes dominant at very high intensities and ultimately decreases the transmission at those very high intensities.

A very interesting effect was also observed on blank waveguides, and that is spectral narrowing of the transmitted pulse, which is exactly the opposite one

would expect from self phase modulation. In our samples two photon absorption dominates self phase modulation. This is due to the former being a real carrier nonlinear process and thus involving real transitions while the former is a virtual transmission that only excites virtual carriers. The combined effects of self phase modulation, two photon absorption and small amounts of chirp lead to spectral narrowing, which is symmetric in blank waveguides, but interestingly it is asymmetric for photonic crystal ridge waveguides. This is due to the fact that the photonic crystal acts as a spectral filter, limiting the pulse intensity on one side of the pulse. The limited intensity pulse side therefore does not have enough intensity to be spectrally compressed, whereas the other side has, leading to asymmetric spectral compression.

To sum up, we have to admit that while we observed some nonlinear behaviour from the photonic crystal itself, there has not been any evidence of any nonlinear shift of the photonic band gap, thus confirming our a priori apprehension about our experimental set-up. Use of the in-plane transmission perpendicular pump-probe set-up does not improve the situation. This is due to the fact that the laser system used lacks the sufficient fluence to obtain a sizeable effect on a large area of the photonic crystal, and thus renders the nonlinear shift undetectable. Further attempts to shift the band edge of two dimensional photonic crystals using a modified in-plane transmission perpendicular pump-probe set-up have been planned for the near future. The modifications involve generating a femtosecond white light continuum with a photonic crystal fibre and using a more powerful laser.

In order to observe a carrier induced refractive index change, it was decided to use a different set up, based on reflection geometry, with a laser capable of generating a white light continuum on sapphire, which requires pump energies ranging from 1 to 1.5  $\mu\text{J}$ , for stable single filament operation. These experiments will be discussed in the next chapter.

**References:**

1. M. D Rahn, A. M. Fox, M. S. Skolnick, T. F. Krauss, "Propagation of ultrashort non-linear pulses through two dimensional AlGaAs high contrast photonic crystal waveguides," J Opt Soc Am B Vol 19, No 4, 716 (2002).
2. M. Patrini, M. Galli, F. Marabelli, M. Agio, L.C. Andreani, D. Peyrade and Y. Chen, "Photonic bands in patterned Silicon on Insulator waveguides," IEEE J. Quantum Electron. Vol. 38, No 7 (2002).
3. M.C. Netti, M.D.N. Charlton, G.J. Parker and J.J. Baumberg, "Visible photonic band gap engineering in silicon nitride waveguides," Appl Phys Lett 76, 991 (2000).
4. On going from medium  $a$  to medium  $b$ , a light wave will experience total internal reflection if and only if  $n_a > n_b$ , where  $n_a$  and  $n_b$  are the refractive indices of the respective media.
5. H. Benisty, C. Weisbuch, D.Labilloy, M. Rattier, C.J.M. Smith, T.F. Krauss, R.M. De la Rue, R. Houdre, U.Oesterle, C. Jouanin, and D. Cassagne "Optical and confinement properties of two-dimensional photonic crystals" J. Lightwave Tech. 17, 2063 (1997).
6. M. Kanskar, P. Paddon, V. Pacradouni, R. Morin, A. Busch, Jeff F. Young, S. R. Johnson, Jim Mackenzie, and T. Tiedje, "Observation of leaky slab modes in an air-bridged semiconductor waveguide with a two-dimensional photonic lattice," Appl Phys Lett 70 1438 (1997).
7. Kuo-Yi-Lim, D.J. Ripin, G.S. Petrich, L.A. Kolodziejski, E.P. Ippen, M. Mondol, H. I. Smith, P.R. Villeneuve, S. Fan, J. D. Joannopoulos, "Photonic band-gap waveguide microcavities: Monorails and air bridges" J. Vac Sci Technol B 17(3) 1171 (1999).
8. V.N.Astratov, R.M.Stevenson, I.S.Culshaw, D.M.Whittaker, M.S.Skolnick, T.F.Krauss, R.M. De La Rue, "Resonant Coupling of Near-Infrared Radiation to Photonic Band Structure Waveguides" J. Lightwave Tech. 17, 2050m (1997).
9. N. Kawai, K. Inoue, N. Ikeda, N.Carlsson, Y.Sugimoto, K.Asakawa, S. Yamada and Y. Katayama, "Transmittance and time-of-flight study of

- AlxGal<sub>1-x</sub>As-based photonic crystal waveguides,” *Phys Rev B*, **63** 153313 (2001).
10. W. Bogaerts, D. Taillaert, R. Baets, V. Wiaux, S. Beckx, M. Maunhoudt, G. Vanderberghe, “SOI Photonic Crystal Fabrication Using Deep UV Lithography,” conference presentation.
  11. P. Dumon, W. Bogaerts, V. Wiaux, J. Wouters, S. Beckx, J. Van Campenhout, D. Taillaert, B. Luysaert, P. Bienstman, D. Van Thourhout, R. Baets, “ Low-loss SOI Photonic Wires and Ring Resonators Fabricated with Deep UV Lithography,” *IEEE Photonics Technology Letters*, **16**(5), p.1328-1330 (2004).
  12. IPK:MIBK is isopropyl-alcohol and methyl-iso-butyl-ketone in a 3:1 ratio mixture.
  13. T. Ochiai and K. Sakoda, “Dispersion relation and optical transmittance of a hexagonal photonic crystal slab,” *Phys. Rev. B* **63**, 125107 (2001).
  14. T. F. Krauss, R. M. De La Rue, S. Brand, “Two dimensional photonic bandgap structures operating at near infrared wavelengths,” *Nature*, Vol **383**, 699 (1996).
  15. D.Labilloy, H. Benisty, C. Weisbuch, T.F. Krauss, R. Houdre and U.Oesterle,” Use of guided spontaneous emission of a semiconductor to probe the optical properties of a two dimensional photonic crystal” *Appl Phys Lett* **71**, 738 (1997).
  16. T. Baba and T. Matsuzaki, ”Polarization change in spontaneous emission from GaInAsP/InP 2-dimensional photonic crystals”, *Electron. Lett.*, Vol. **31**, 20, pp. 1776-1778, (1995).
  17. J. D. Joannopoulos, R. D. Meade and J. N. Win, “Photonic Crystals: Molding the flow of light” (Princeton University press, 1995).
  18. C. Reese, C. Becher, A. Imamoglu, E. Hu, B.D. Gerardot, P.M. Petrof, “Photonic crystal microcavities with self-assembled InAs quantum dots as active emitters” *Appl Phys Lett* **78**, 2279 (2001).
  19. M. Notomi, K. Yamada, A. Shinya, J. Takahashi, C. Takahashi, and I. Yokohama, “Extremely Large Group-Velocity Dispersion of Line-Defect

- Waveguides in Photonic Crystal Slabs “ Phys Rev Lett. **87**(25) 253902 (1999).
20. A. Talneau, L. Le Gouezigou, N. Bouadma, M. Kafesaki, C.M. Soukoulis, M. Agio “Photonic-crystal ultrashort bends with improved transmission and low reflection at 1.55  $\mu\text{m}$ ” Appl Phys Lett **80**, 547 (2002).
  21. W.M. Robertson, G. Arjavalingam, R.D. Meade, A. Rappe, K. Brommer, and J.D. Joannopoulos, "Measurement of Photonic Band structure in a Two-Dimensional Periodic Dielectric Array." Phys. Rev. Lett. **68**, 2023 (1992).
  22. See for instance, Y.R. Shen, “The Principles of Nonlinear Optics” Wiley (1984).
  23. A. R. Cowan, G.W. Rieger, J.F. Young, “Nonlinear transmission of 1.5  $\mu\text{m}$  pulses through single mode silicon on insulator waveguide structures” Optics Express Vol. **12** No. 8, 1611 (2004).
  24. G.W. Rieger, K. S. Virk, J.F. Young, “Nonlinear propagation of ultrafast 1.5  $\mu\text{m}$  pulses in high-index-contrast silicon-on-insulator waveguide” Appl Phys Lett **84**, 900 (2003).
  25. E. W. Van Stryland, Y. Y. Wu, D. J. Hagan, M. J. Soileau, Kamjou Mansour, “Optical limiting with semiconductors” J Opt Soc Am B Vol **5**, No 9, 1980 (1988).
  26. A. D. Bristow D. O. Kundys, A. Z. García-Déniz, J.-P. R. Wells, A. M. Fox, M. S. Skolnick, D. M. Whittaker, A. Tahraoui, T.F. Krauss, J.S. Roberts, “Ultrafast nonlinear tuning of the reflection properties of AlGaAs photonic crystal waveguides by two photon absorption” J. Appl. Phys. **96** 4729 (2004).
  27. Values calculated using the parameters in: A.D. Bristow, “Optical investigation of AlGaAs photonic crystal waveguides”, PhD thesis, University of Sheffield, (2003).

# **Chapter 4: Real Carrier Nonlinear Properties of 1D Photonic Crystal Waveguides**

## **4.1. Introduction**

## **4.2. Introduction to Semiconductor Quantum Wells**

## **4.3. Experimental Methods**

### **4.3.1. Samples**

### **4.3.2. Reflectivity Measurements**

### **4.3.3. Modelling of Reflectivity Spectra**

## **4.4. Linear Characterization**

## **4.5. Time-Resolved Pump-Probe Reflectivity Measurements**

### **4.5.1. Experimental Details**

### **4.5.2. Single and Two photon absorption tuning of photonic resonances**

### **4.5.3. Two and Three photon absorption tuning of photonic resonances**

## **4.6. Conclusions**

“No plan survives contact with the enemy”

*Hemulth Von Moltke the Elder*

#### 4.1 Introduction

In the previous chapters, two dimensional photonic crystals embedded in a ridge waveguide have been discussed. In this chapter, I shall concentrate on one dimensional photonic crystals; these are like Bragg stacks or similar multilayer structures but they are constructed by etching a pattern of stripes on a slab waveguide, as described in the previous chapter for two dimensional photonic crystals.

The samples used in this chapter include multiple quantum wells, in clear contrast to sample AT218 used in chapters 2 and 3, which was a passive sample. This means that it lacked an active gain material, such as quantum wells or quantum dots. The inclusion of quantum wells was done in order to attempt to obtain a resonant nonlinear shift of a photonic mode by means of the optical (ac) Stark effect<sup>1</sup>, which is an instantaneous effect where only virtual carriers are involved. The inclusion of multiple quantum wells enhances the nonlinear response of the samples, due to the real carrier nonlinearity presented by these systems. This will increase the nonlinear change of the refractive index and thus, the shift of the photonic features.

In this chapter experimental results will be presented, showing all-optical tuning of photonic resonances caused by real carriers excited by single and two photon absorption acting together, by two photon absorption in the near infrared and in

the infrared and by three photon absorption in the infrared. Virtual carrier nonlinearities will be discussed in chapter 5.

In section 4.2 a brief introduction to semiconductor quantum wells will be given. In section 4.3, the samples used in this, and the following, chapter, will be discussed. A discussion of the external coupling technique in reflectivity geometry will be given along with a discussion of the modelling of the reflectivity spectra obtained using this technique. Section 4.4 will show linear measurements of the samples used, for the purposes of characterization. Section 4.5 will discuss all-optical tuning of photonic resonances. Sub section 4.5.1 will concentrate on single and two photon absorption when pumping near the bandgap, whereas sub section 4.5.2 will concentrate on two and three photon absorption with pumping at longer wavelength. Finally, section 4.6 will sum up the results and conclusions from the experimental results obtained in this chapter.

## **4.2. Introduction to Semiconductor Quantum Wells**

The simplest possible quantum well consists of a layer of semiconductor material, sandwiched by another material with a larger band gap. A widely used material is GaAs, which is then doped with aluminium (to form  $\text{Al}_x\text{Ga}_{1-x}\text{As}$ ) to constitute the quantum well barriers<sup>2</sup>. A schematic example of the band structure of a typical GaAs/AlGaAs quantum well can be seen in figure 4-1.

By reducing the size of the quantum well to values comparable to the electron wavelength, i.e. 1 to 10 nm, the electrons are effectively confined to move on a two dimensional plane. This confinement will lead to quantization effects, which will result in discrete energy bands; the energy of these bands is dependent on the height and width of the barrier.

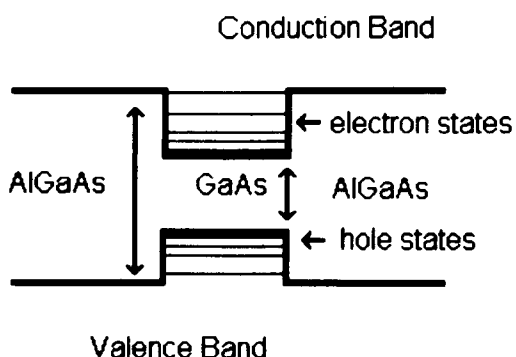


**Figure 4-1** Schematic drawing of a GaAs/AlGaAs single quantum well.

The quantized energy levels, are responsible for the step wise density of states function, in clear contrast to the bulk semiconductor that depends on the square root of the energy, as shown on figure 4-2 b). This reduction in size to the order of the electronic wavelength can be extended to two or three dimensions, which will create quantum wires and quantum dots, respectively.

Bound electron-hole pairs are normally referred to as excitons<sup>3</sup>. The dipole moment of an exciton is resonant at an energy  $E_{ex} = E_g + E_b$ , where  $E_g$  is the band gap energy of the material and  $E_b$  is the binding energy of the exciton. A clear signature of the exciton can be seen through absorption spectroscopy in the shape of a clear and sharp peak at  $E = E_{ex}$  as can be seen in figure 4-2 a) at  $E \sim 1.47$  eV.

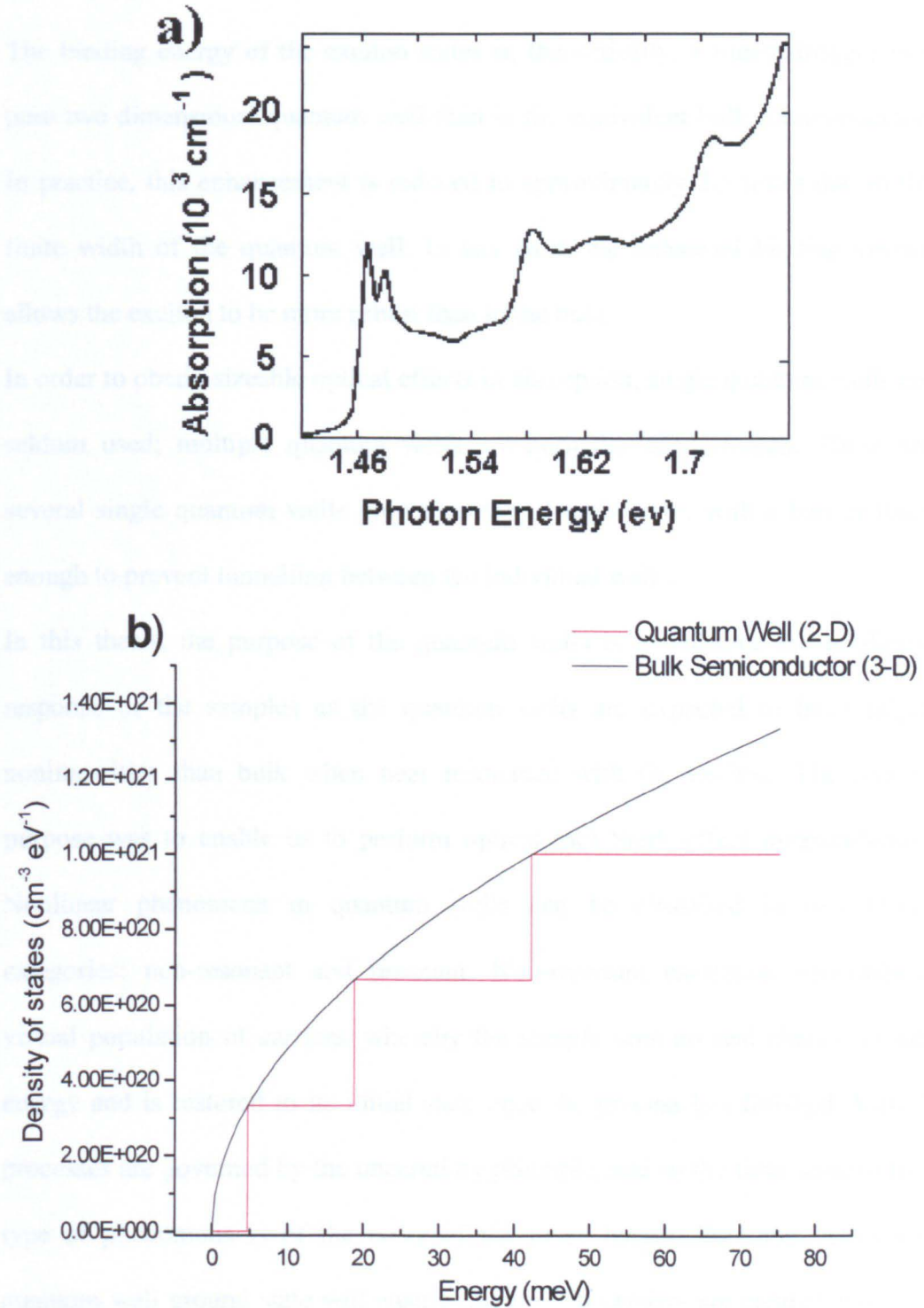


**Figure 4-2 a)** Absorption spectra of GaAs/AlGaAs multiple quantum wells<sup>4</sup>. **b)** Density of states function for a 10 nm quantum well with infinite barriers and bulk semiconductor. The effective mass is  $m^* = 0.8 m_0$ , where  $m_0$  is the electron rest mass, see table 4.3

The binding energy of the exciton states is, theoretically, 4 times stronger in a pure two dimensional quantum well than in the equivalent bulk semiconductor. In practice, this enhancement is reduced to approximately 2.5 times due to the finite width of the quantum well. In any case, the enhanced binding energy allows the exciton to be more robust than in the bulk

In order to obtain sizeable optical effects in absorption, single quantum wells are seldom used; multiple quantum wells are normally used instead. These are several single quantum wells grown on top of each other, with a barrier thick enough to prevent tunnelling between the individual wells.

In this thesis, the purpose of the quantum wells is to enhance the nonlinear response of the samples as the quantum wells are expected to have larger nonlinearities than bulk when near resonance with the exciton. The second purpose was to enable us to perform optical (ac) Stark effect measurements. Nonlinear phenomena in quantum wells can be classified in two broad categories: non-resonant and resonant. Non-resonant excitation generates a virtual population of carriers, whereby the sample sees no real change of net energy and is restored to its initial state once the process has finished. Virtual processes are governed by the uncertainty principle, and so the time scale of this type of phenomena is of the order of the pulse length. Pumping below the quantum well ground state will ensure that no real carriers are created and thus the phenomenon will be non-resonant or virtual.

If, on the other hand, resonant pumping is used, i.e. above the quantum well ground state, a population of real carriers will be created. This population of real

carriers has a finite lifetime, which is related to the relaxation time of the carriers and is different for every particular material system. Hence resonant nonlinearities are expected to be slower than the pulse width.

In this chapter real carrier nonlinear effects will be studied, virtual carrier nonlinearities will be studied in the next chapter.

### **4.3 Experimental Methods**

In this section a brief description of the samples used will be given as well as a comprehensive description of the experimental set-up. A short introduction to the modelling of the reflectivity of patterned one-dimensional photonic crystals will also be given.

#### **4.3.1 Samples**

In contrast with chapter 3, the samples used in this chapter are one dimensional photonic crystals. However, these one dimensional samples are not a simple alternating sequence of dielectric layers in the form of a dielectric mirror, which has been known for many years, but are photonic crystals etched on a slab waveguide, fabricated in much the same way as the samples used in chapter 3. The reason for opting to use one dimensional photonic crystals rather than two dimensional photonic crystals as used so far in this thesis, lies in the fact that one dimensional photonic crystals have sharper photonic resonances than two dimensional photonic crystals. Sharper photonic resonances make detecting nonlinear effects easier, this will be discussed further in section 4.4

There is one more key difference, other than dimensionality, between the samples used so far and the samples used in this chapter, and that is the inclusion of quantum wells on the core of the slab waveguide. The main reason behind this decision is an attempt to improve the nonlinear response of the samples as discussed in the previous section.

The sample used is from wafer QT1737b. It consists of 5  $\text{In}_{0.12}\text{Al}_{0.20}\text{Ga}_{0.68}\text{As}$  quantum wells, with an approximate thickness of 9.6 nm, with barriers made of  $\text{Al}_{0.20}\text{Ga}_{0.80}\text{As}$  and thickness 10 nm. The room temperature photoluminescence emission is at approximately  $\lambda = 799$  nm. The core consists of the multiple quantum wells, sandwiched by two layers of  $\text{Al}_{0.20}\text{Ga}_{0.80}\text{As}$  with a total thickness of 0.4  $\mu\text{m}$ . The cladding is a single layer of  $\text{Al}_{0.60}\text{Ga}_{0.40}\text{As}$  1.5  $\mu\text{m}$  thick. A 10 nm capping layer of GaAs is deposited on top of the sample in order to prevent oxidation. The optical effects of this capping layer are negligible due to its small thickness.

There are three different etch depths: 100, 200 and 850 nm. The samples are periodically patterned in just one dimension. The periods range from 330 nm to 880 nm, while the air fill factor ranges from 10 to 30%. There are also two exposure doses, which will be referred to as High and Low exposure doses or HX and LX respectively.

A schematic drawing of a typical sample can be seen in figure 4-3 below. The inset shows the multiple quantum wells embedded in the slab waveguide more clearly.

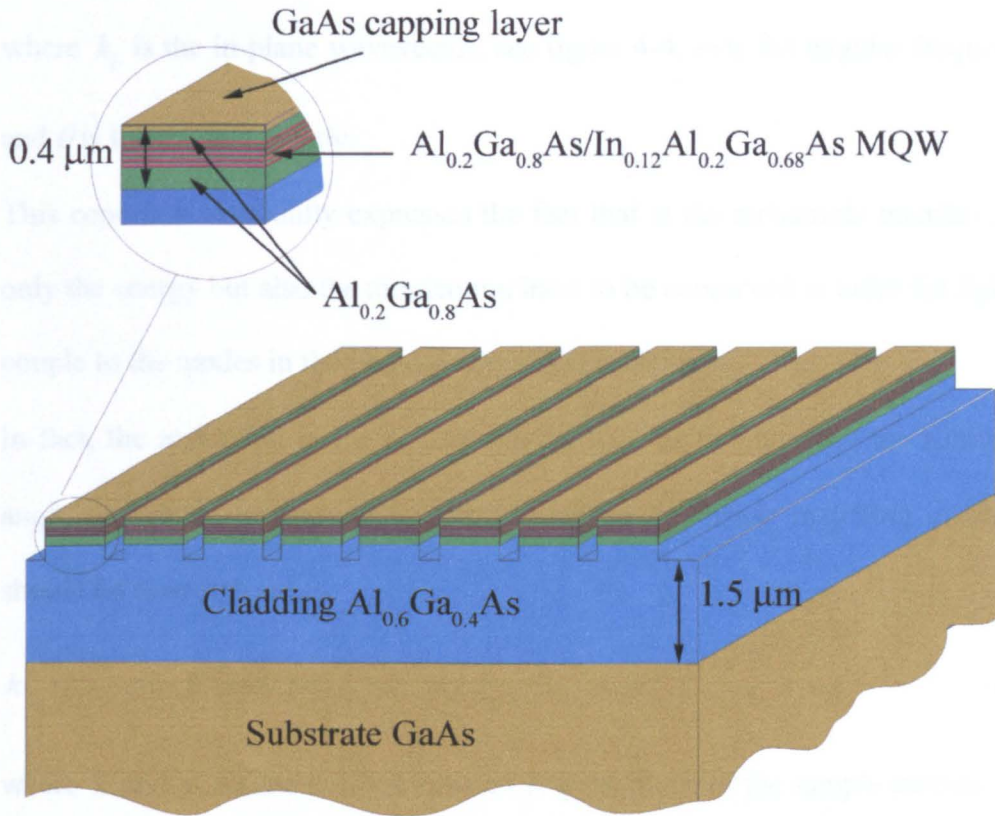


**Figure 4-3** Schematic drawing of a typical sample. Note the multiple quantum wells on the inset.

### 4.3.2 Reflectivity Measurements

In contrast to the previous chapter, the experimental technique used in this chapter to investigate the samples is the external coupling reflectivity method. This technique has been widely used to indirectly measure the band structure of photonic crystals<sup>5,6</sup>. This is possible because the technique allows us to vary the incoming light wavevector almost at will; the phase matching condition is, normally, expressed as follows:

$$k_{\parallel} = \frac{\omega}{c} \sin \theta \quad (4.1)$$

where  $k_{\parallel}$  is the in-plane wavevector, see figure 4-4,  $\omega$  is the angular frequency, and  $\theta$  is the coupling angle.

This condition essentially expresses the fact that at the air/sample interface, not only the energy but also the momentum have to be conserved in order for light to couple to the modes in the photonic crystal at each angle.

In fact, the azimuthal angle  $\phi$  also plays a role, as by changing the azimuthal angle the lattice orientation is rotated, and so the phase matching condition should be rewritten as:

$$k_{\parallel} = \frac{\omega}{c} \sin \theta (\cos \phi \hat{x} + \sin \phi \hat{y}) \quad (4.2)$$

where  $\hat{x}$  and  $\hat{y}$  are the unit vectors defining the plane of the sample surface.

In practice measurements tend to be made along high symmetry directions and the azimuthal angle plays no role along high symmetry directions, therefore the phase matching condition can be taken to be equation 4.1.

The reflectivity technique couples only to the leaky modes of the structure as incoming light lacks sufficient momentum<sup>7</sup> to couple to the guided modes. Note how this was not the case in the samples in the previous chapter, where the butt coupling from the ridge waveguides provided the necessary additional in-plane momentum.

The photonic band structure of the samples can be obtained by changing the coupling, or polar angle; by doing this, the in-plane wavevector is changed and so the photonic band structure can be mapped out.

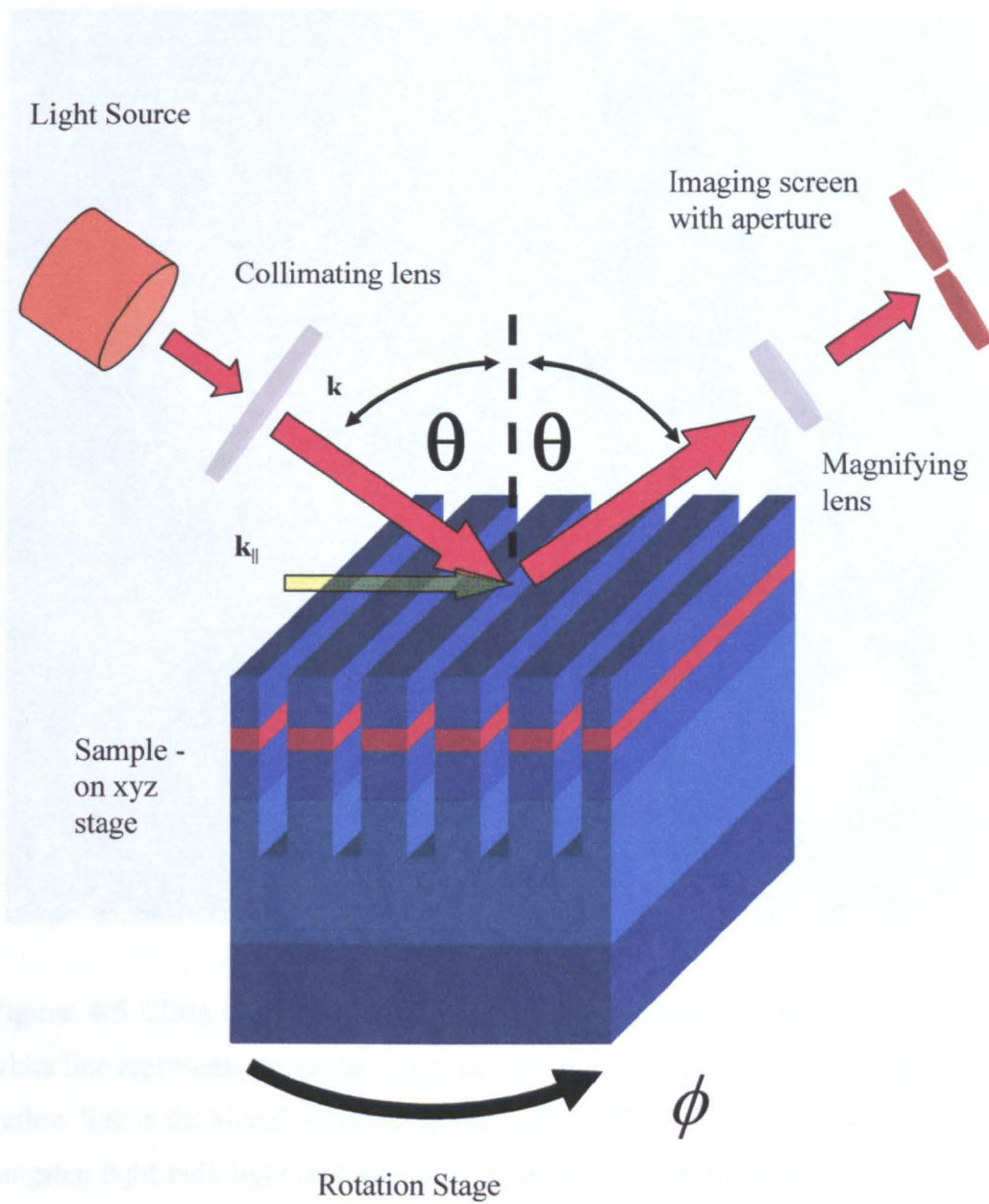
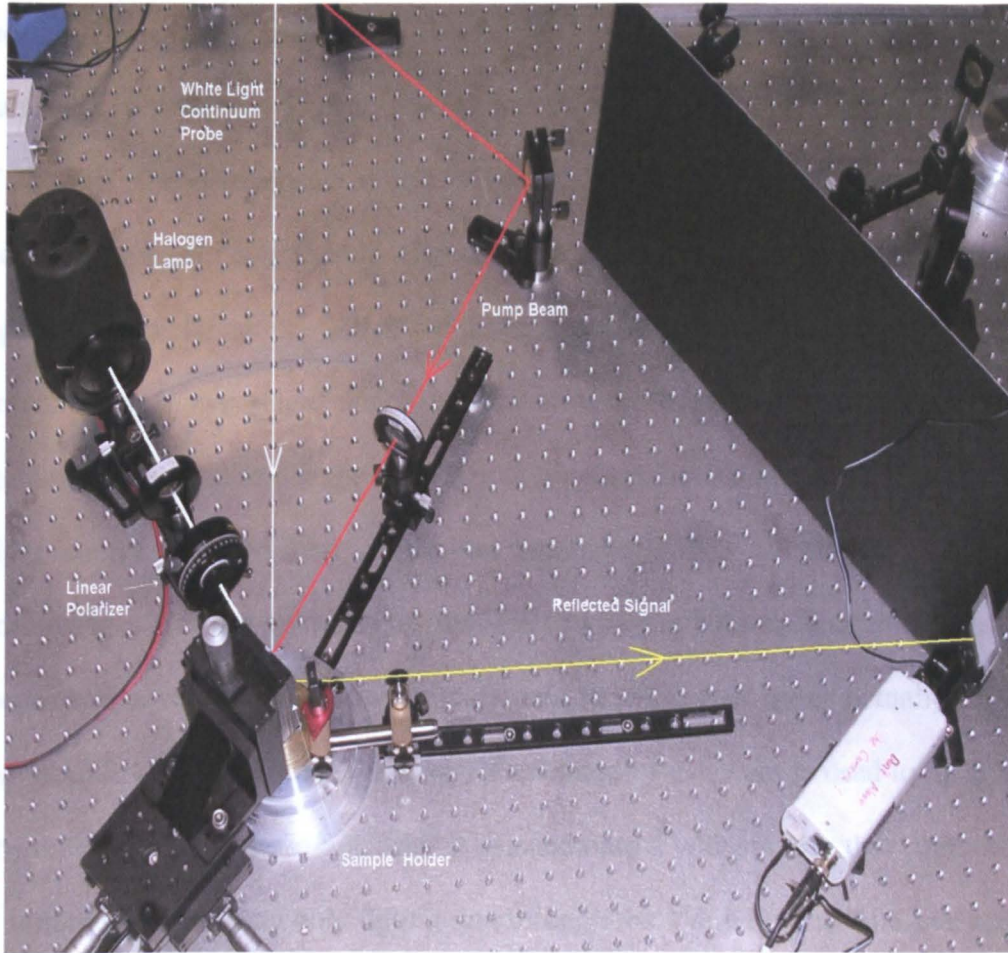


**Figure 4-4** Schematic drawing of the external coupling reflectivity set-up. The polarizing optics are omitted for clarity.



The reflection from the sample as used in the experiment.

**Figure 4-5** Close up photograph of the experimental set-up as used. The thin white line represents the probe beam, the red line represents the pump beam. The yellow line is the signal reflected by the sample. Thick white line represents the tungsten light bulb light (not set up for measurements in the picture). The probe beam angle is set to  $45^\circ$ , and the pump beam angle is set to  $30^\circ$ . Note how the sample holder is set at an angle of  $45^\circ$ .

The experimental set-up used for linear characterization is fairly simple. Figure 4-4 shows a schematic drawing of the underlying basis of the set up, while figure 4-5 is a photograph of the actual experimental set-up used. A tungsten halogen lamp is used as the light source due to its good spectral output in the visible and

near infrared; the output power is 150 W. The output light from the tungsten lamp is collimated by a plano-convex lens, made of BK7 and with focal length  $f=10$  cm. The divergence of the beam is  $<2^\circ$ , which is important to obtain accurate spectra. A rotatable Glan-Thomson polarizer is used to select the appropriate polarization. After the polarizer, light hits the sample which is mounted on a xyz stage, which in turn is mounted onto a goniometre. The goniometre is used to change the angle of the sample, as well as the angle of the light source. This system allows accurate positioning of the sample on a millimetre scale. It would also be possible to mount a Helium flow micro-stat to perform measurements at low temperatures but this was never actually done. Another BK7 Plano convex lens with focal length  $f=1.5$  cm is used to magnify the reflection from the sample; this is imaged onto a white screen that contains a 1 mm hole. In this way only light going through the 1 mm hole will be analyzed. The reflection from the sample is magnified approximately 40 times, in order to allow careful positioning of the sample. A closed circuit television camera with a charged coupled device sensor is used to image the magnified reflection from the sample. This is not really necessary for linear characterization, as there is enough visible light from the tungsten lamp itself but it will be extremely helpful when working with weaker near infrared sources, i.e. the femtosecond white light continuum.

After the selecting screen, light is directed via several steering mirrors towards a Triax 320 spectrograph. Light was coupled to the spectrograph using a cylindrical lens with focal lens  $f = 10$  cm made of BK7 glass. Several other

lenses with similar focal lengths were used with no appreciable benefit or detriment in performance. The detector used is a silicon charged coupled device detector manufactured by Andor that has good responsivity around 800 nm.

In time resolved reflectivity measurements, the halogen lamp is moved out of the way. However it is not completely removed as it provides an easy and reliable way to double check the wavelengths of the photonic resonances. The time resolved pump probe set up uses a regenerative Ti:sapphire amplifier system (Spitfire by Spectra Physics) with limited tuneability from 750 to 850 nm, but up to 1 mJ pulse energy, giving a maximum power of 1 W at a repetition rate of 1 kHz, with a pulse length of 130 fs. A schematic drawing of the Spitfire regenerative compression process is shown in figure 4-6. The Spitfire is seeded by a mode-locked Ti:sapphire laser, called the Mai Tai. The beam from the Mai Tai is stretched before entering the amplifier cavity to avoid optical damage to the gain medium which would occur from the high peak powers resulting from amplified very short pulses. The pulse is stretched by the stretcher stage which consists of a centrally mounted grating that chirps the seed pulse.

The pump laser, the aptly named Merlin<sup>i</sup>, is a Q-switched frequency doubled Nd:YLF laser with pulse energy of 10mJ at  $\lambda = 527$  nm, which for a repetition rate of 1kHz yields 10 W. Both pump and seed beams overlap in the Ti:sapphire crystal within the Spitfire cavity.

---

<sup>i</sup> The engine used in the Second World War fighter plane Supermarine Spitfire, was the Rolls Royce made Merlin.

The Pockel cells, PC1 and PC2 in figure 4-6, control the number of round trips the pulse makes inside the amplifier cavity, before exiting via the output coupler, OC in figure 4-6. This can be monitored through the signal of an optical detector, RX, connected to an oscilloscope. The resulting pulse is compressed on the compressor stage to return the pulse to its initial pulse length.

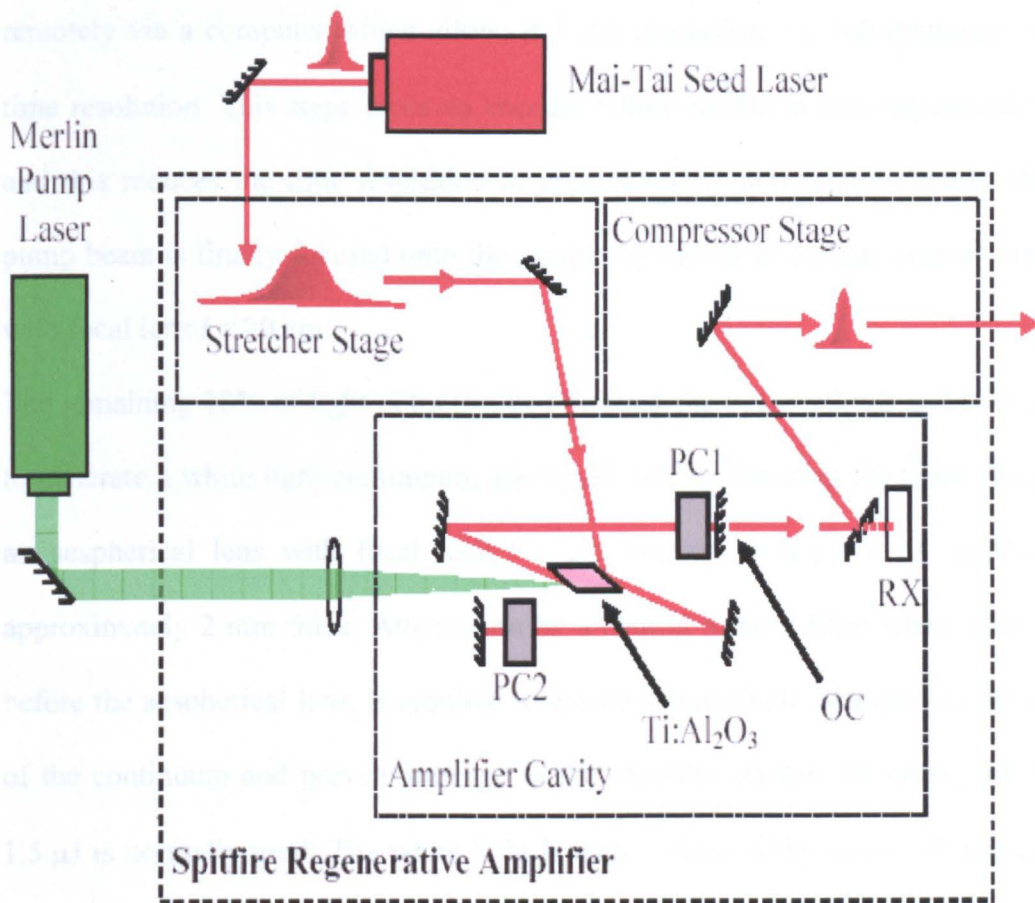


**Figure 4-6** Schematic of the Spitfire regenerative amplifier laser system. See text for details.

The output from the Spitfire is split by a beam splitter in the ratio 90/10, (reflection/transmission). The reflected beam pumps a Travelling wave Optical Parametric Amplifier of Super fluorescence, or TOPAS OPA, with tuneable range from 240 nm to 20  $\mu\text{m}$ . The output of the TOPAS OPA is used to pump the sample and is guided on to the sample by a set of mirrors. The path length of the pump beam can be altered by a motorized translation stage controlled remotely via a computer which allows a 1  $\mu\text{m}$  resolution, i.e. 6.6 femtosecond time resolution. This stage lacks an encoder which results in poor repeatability and this reduces the time resolution to approximately 300 femtoseconds. The pump beam is finally focused onto the sample by means of a plano-convex lens with focal lens  $f = 20$  cm.

The remaining 10% of light is transmitted through the beam splitter and is used to generate a white light continuum, see figure 4-7, by focusing the beam using an aspherical lens with focal lens  $f = 2.5$  cm, on to a piece of sapphire approximately 2 mm thick. Attenuation by a neutral density filter wheel placed before the aspherical lens, is required to ensure stable single filament operation of the continuum and prevent damage to the sapphire crystal. An energy of 1-1.5  $\mu\text{J}$  is normally used. The white light is then collimated by means of a small focal length  $f = 1.5$  cm lens, and guided on to the sample. This continuum of light will be used as the probe beam. Both the sapphire crystal and collimating lens are placed on one dimensional translation stages to ease the focusing and collimating process. The femtosecond white light continuum is, perhaps, the most critical part of the set-up and will be further discussed in section 4.4.

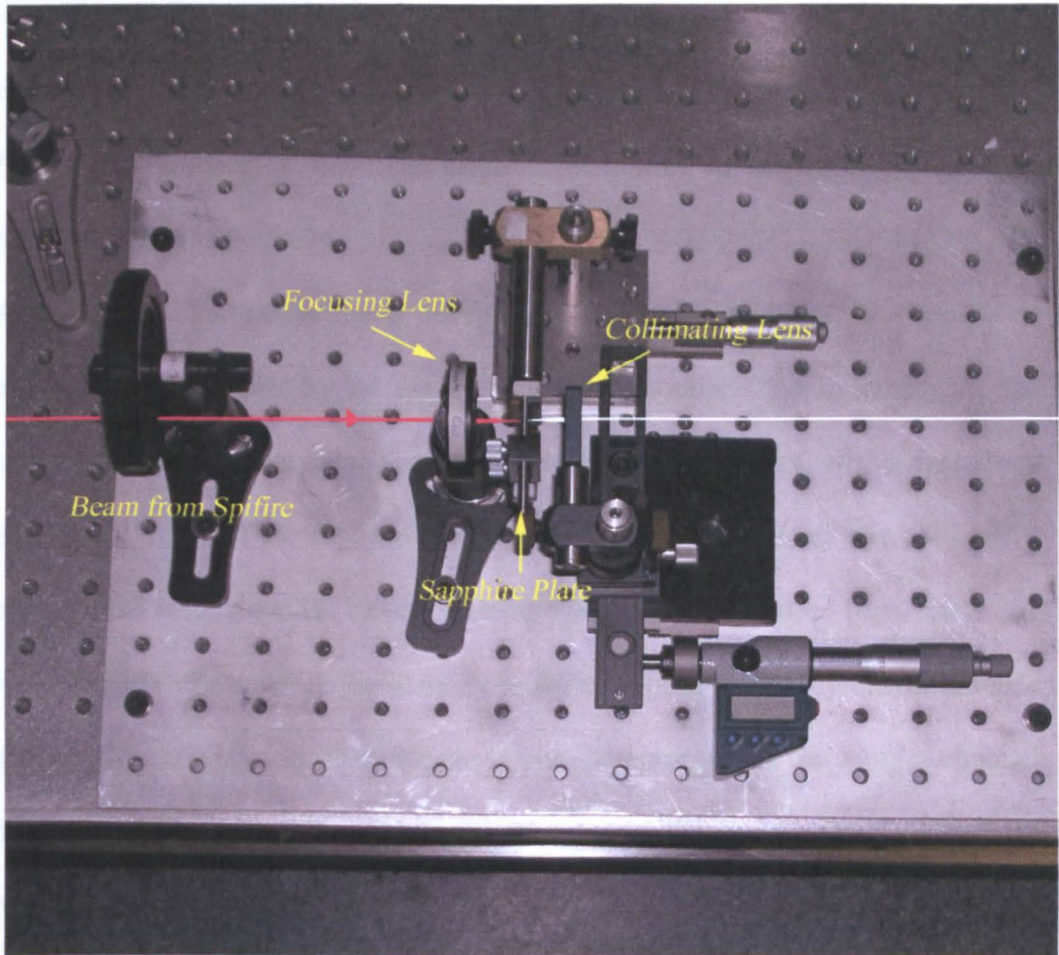


**Figure 4-7** Femtosecond white light continuum generation apparatus. See text for details.

The detection techniques are quite different depending on the detector used. The charged coupled device detector allows us to use a reference beam, which is obtained by means of a 90/10 Transmission/Reflection beam splitter placed after the white light continuum generator, to normalize the signal in real time. This is done by dividing the detector chip into two tracks, and focusing the reference onto one track and the signal onto another. A simple division allows us to remove intensity fluctuations of the white light continuum. The rest of the set-

up is identical to the linear characterization set-up, except for the lens used to couple light to the spectrometer; this was changed to a plano-convex lens with  $f=10$  cm, in order to allow the different beams to be focused onto different tracks on the detector chip.

A lock-in technique is used for single channel detection. The probe is mechanically chopped by an opto-mechanical chopper. The frequency of the chopper is set such that it is synchronous with the laser pulses, with a frequency of 500 Hz, i.e. half the repetition rate of the laser. This means that only every other pulse will actually hit the sample. A lock-in amplifier then reads the reflected light detected by the detector at the chopping frequency only and feeds this modified signal to a computer. The detector used for single channel detection was an ultra sensitive liquid nitrogen cooled germanium detector sold by Edinburgh Instruments.

It should be noted that the white light continuum is significantly weaker than the halogen white light source, and therefore the use of the television camera is crucial in order to select the appropriate sample.

It is also possible to use the TOPAS OPA to generate the white light continuum. This will be used for experiments carried out in the next chapter. The alterations of the experimental set-up required for this configuration will be discussed in section 5.2.

### 4.3.3 Modelling of Reflectivity Spectra

Modelling of unpatterned photonic structures, e.g. distributed Bragg reflectors or one dimensional microcavities, can be accomplished by the transfer matrix method. The transfer matrix is calculated independently for each in-plane vector by expanding the field in each layer in terms of plane waves with its corresponding perpendicular wavevector and using electromagnetic boundary conditions at the interfaces.

This method works less well for patterned structures because the substrate of the structures is significantly different from the structures themselves, i.e. unpatterned substrates versus patterned structures. This, then calls, for an alternative approach. Our simulations will use the scattering matrix method. This method is similar to the transfer matrix method in that it considers the incoming waves and outgoing waves at either side of the structure. In the scattering matrix method the outgoing waves at the surface and in the substrate are related to the amplitudes of the incoming waves on either side of the structure. In contrast, in the transfer matrix method, the amplitudes of the incoming and outgoing waves are expressed in terms of the amplitude of the waves in the substrate.

A full discussion on both methods is beyond the scope of this thesis. It is, however, interesting, to discuss in further detail how reflectivity spectra are modelled as this will be our main use of this modelling tool. A fully detailed account of the scattering matrix method is given in reference 8, while a basic description of the transfer matrix method can be found in many optics text books<sup>9</sup>.

The reflectivity spectra were calculated using a suite of programs developed by D.M. Whittaker. In order to calculate a reflectivity spectrum, firstly the photonic band structure is resolved and then a layer by layer field profile is assembled using the band structure. Forward and backward propagating waves are used to express these field profiles. Boundary conditions are then imposed upon the field profiles at each interface. By relating the fields between adjacent layers the scattering matrix is constructed and is applied to an expression for the incoming light and thus the reflectivity is obtained.

The scattering matrix method can also provide information on the electromagnetic energy density for a particular wavelength at a certain coupling angle, i.e. energy and wavevector. Two possible calculations can be performed: In-plane average energy density as a function of depth or the in-plane values of fields and densities across the unit cell at a particular depth. The average energy density is significantly higher when a mode is sustained by the photonic crystal. The scattering matrix calculations will give information on the confinement order of the mode, i.e. whether it is first order, second order, etc and the in-plane distribution in the photonic crystal lattice.

A comparison between the modelling and the experimental data will be given in the next section.

#### **4.4 Linear Characterization**

In order to have a good grasp of what the spectral response of every sample is before attempting time resolved measurements, it is good practice to

measure the linear response of the samples; this will help identify suitable photonic resonances, and thus will make the time resolved measurements significantly faster and easier. The measurements use the linear characterization experimental set-up as described in section 4.3.2 and consist of a set of angle dependent spectra taken from  $20^\circ$  to  $45^\circ$ , in  $5^\circ$  steps. While the set-up allows for a polar angle range of  $12.5^\circ$  to  $65^\circ$ , the samples have been designed to have photonic resonances close to the exciton energy for angles around  $35^\circ$  to  $45^\circ$ , which are the optimal angles for the experimental set-up. The reason for this requirement is that the optical (ac) Stark effect strongly depends on the wavelength detuning. Therefore it will be advantageous to have photonic resonances close to the exciton at the optimal angles for the set-up. The optical Stark effect will be discussed in the next chapter in section 5.5.

The main objective of these set of measurements is to locate a suitable photonic resonance. This has to be reasonably sharp, a quality factor<sup>10</sup> around 70 should suffice, and ideally be some spectral distance away from 800 nm as the white light continuum is generated at 800 nm and thus the resonances are impossible to make out clearly. The reasons for this will be discussed in section 4.4.

A typical example of an experimental set of data is shown in figure 4-8 a), where angle dependent spectra have been measured for a sample from the high exposure dose with the following parameters: Period  $a = 435$  nm, air fill factor  $f = 30\%$  and etch depth  $d = 100$  nm while a corresponding set of angle dependent modelled spectra is shown in figure 4-8 b).

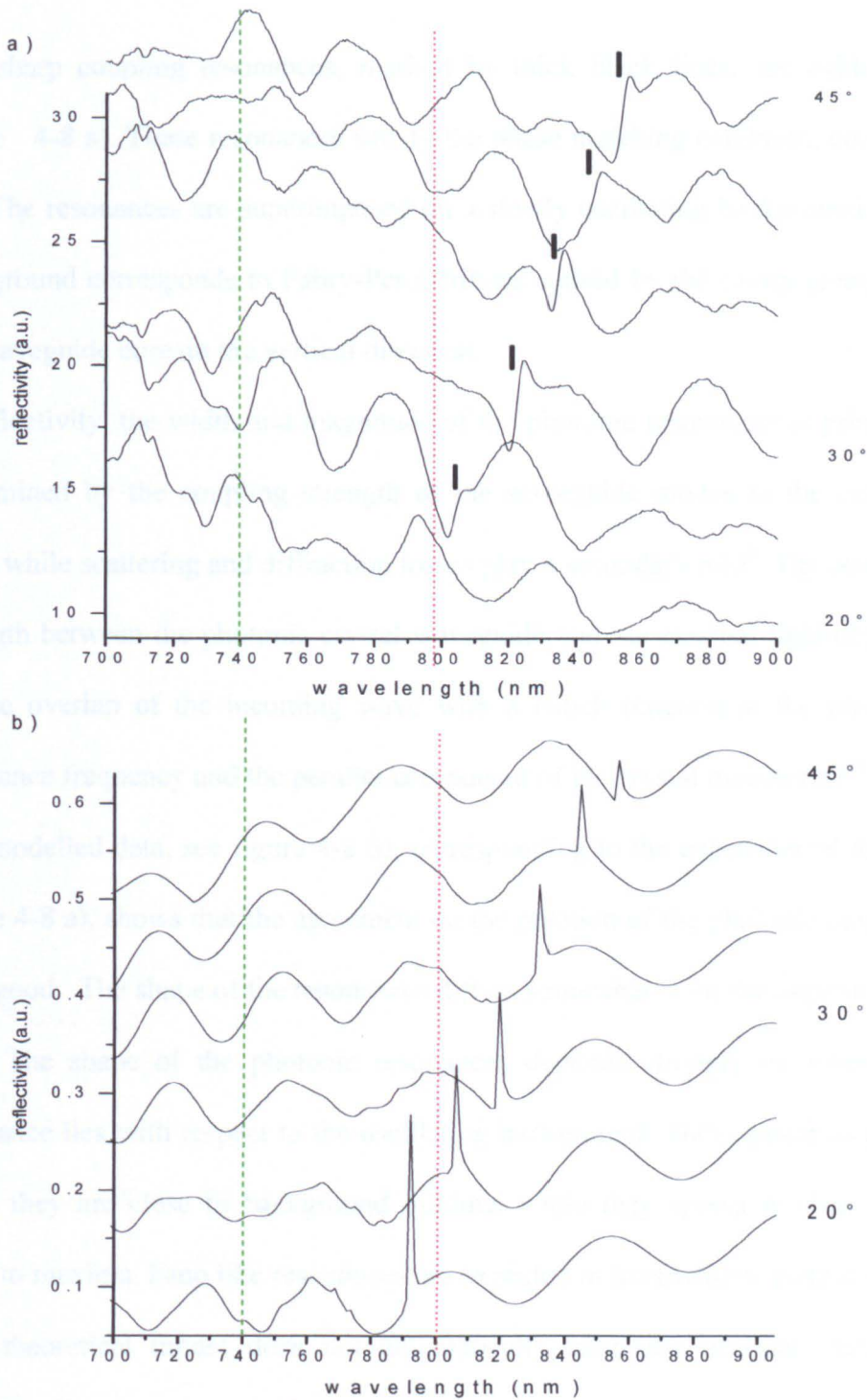


**Figure 4-8** Experimental, a), and modelled, b) angle dependent reflectivity spectra. The sample details are as follows:  $a = 435$  nm,  $f = 30\%$  and  $d = 100$  nm. The green dashed line indicates the position of the electronic band gap of  $\text{Al}_{0.20}\text{Ga}_{0.80}\text{As}$ , while the red dotted line indicates the position of the exciton. The thick black lines indicate the approximate position of the photonic resonances.

The sharp coupling resonances, marked by thick black lines, are evident in figure 4-8 a). These resonances satisfy the phase matching condition, equation 4.1. The resonances are superimposed on a slowly oscillating background. This background corresponds to Fabry-Perot fringes caused by the cavity created by the waveguide core on the vertical direction.

In reflectivity, the width and magnitude of the photonic resonances is primarily determined by the coupling strength of the waveguide modes to the external light, while scattering and diffraction losses play a secondary role<sup>5</sup>. The coupling strength between the photonic crystal waveguide and the external light depends on the overlap of the incoming wave with a Bloch function at the photonic resonance frequency and the parallel component of the crystal momentum<sup>11</sup>.

The modelled data, see figure 4-8 b), corresponding to the experimental data in figure 4-8 a), shows that the agreement on the position of the photonic modes is very good. The shape of the resonances differs somewhat from the experimental data. The shape of the photonic resonances depends strongly on where the resonance lies with respect to the oscillating background. They appear as peaks when they are close to background minima, while they appear as dips when close to maxima. Fano like resonances are expected in intermediate positions<sup>5</sup>.

This theoretical model does not automatically take into account interband absorption effects. It is possible, however, to incorporate absorption by altering the imaginary refractive index, which can help model absorption effects such as interband absorption.

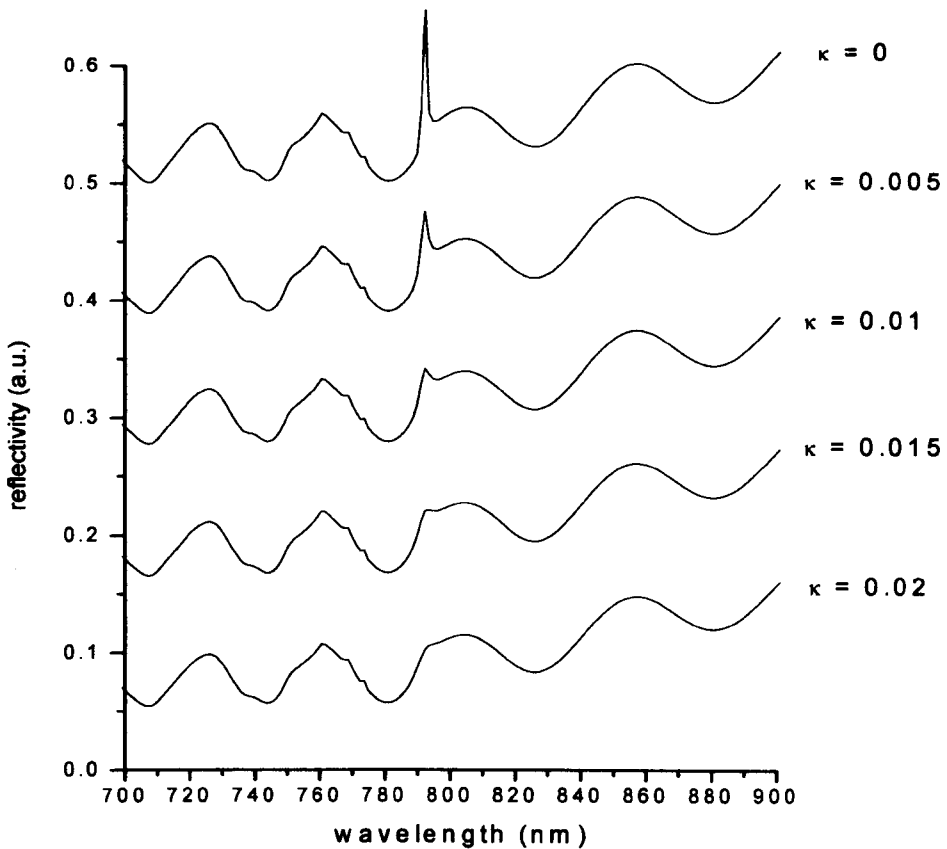


**Figure 4-9** Modelled reflectivity spectra at  $20^\circ$  for non-zero complex refractive index. The sample details are as follows: Period  $a = 435$  nm, air fill factor  $f = 30\%$  and etch depth  $d = 100$  nm.

The effects of the imaginary refractive index can be seen on figure 4-9; where the increasing imaginary refractive index results in a progressive decrease of the photonic resonance strength. This effect will have a marked impact on the time resolved measurements in the following sections.

Care should be exercised when looking at resonances close to the exciton wavelength, i.e. 799 nm marked by a red dotted line in figure 4-8 a), due to single photon absorption associated with the exciton. This absorption explains

why the photonic resonance in figure 4-8 a), present at all coupling angles from  $45^\circ$  down to  $25^\circ$ , disappears at  $20^\circ$ .

#### **4.5 Time-Resolved Pump-Probe Reflectivity Measurements**

In this section time-resolved reflectivity measurements will be discussed. Wavelength dependent as well as power dependent time resolved measurements will be discussed.

##### **4.5.1. Experimental Details**

The experiments were performed by pump-probe spectroscopy. Pump-probe spectroscopy, is conceptually very simple. A high intensity laser beam is split into two components by a beam splitter: a high intensity pump beam and a low intensity probe beam. A time delay is introduced between the two beams, and the linear response is measured for negative time delay, when the probe arrives before the pump, and there is therefore no nonlinear response. At zero time delay, the nonlinear effect will be largest and its time evolution will then be observed as the time delay increases and the nonlinear effect decays.

The use of a femtosecond white light continuum, coupled with a charged coupled device detector, allows us to perform spectrally resolved measurements as well as time resolved measurements at the same time. There are however certain limitations to this technique. The main limitation is the useful spectral region obtainable from the femtosecond white light continuum. The useful spectral region is limited in two ways:

Firstly, close to the continuum centre wavelength, (800 nm throughout this chapter) the instability of the white light continuum means that photonic resonances spectrally close to this wavelength are impossible to make out with clarity. This effectively excludes any photonic resonance located between 770nm and 830 nm from being measured. A simple way to overcome these difficulties will be discussed in the next chapter.

Secondly, the useful spectral region is further limited by the intensity of the continuum far away from the centre wavelength. For the long wavelength case, and bearing in mind the limitations imposed by the Andor charged coupled device detector used, the useful spectral region is limited to approximately 950 nm. So the useful spectral range available is from 830 nm to 950 nm. This is shown in figure 4-10. At longer wavelengths than approximately 950 nm, the signal is the background noise due to the many accumulations used to take the spectrum.

Due to the extra noise associated with nonlinear processes that generate it, the white light continuum has to be constantly monitored. Regular changes in the compression of the seeded pulse on the Spitfire laser system are necessary in order to clearly ascertain the presence of a photonic resonance, as the spectral shape of the continuum can make the resonances impossible to detect. Different continuum spectral shapes will lead to somewhat different shapes for the same photonic resonance.

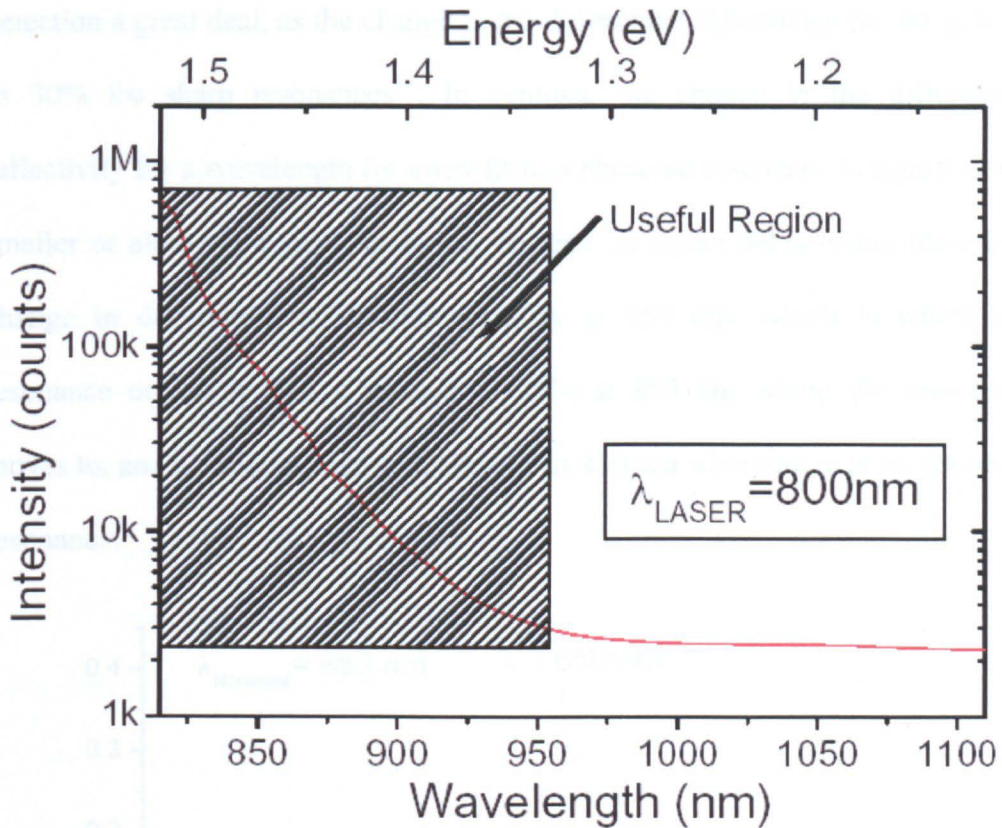


**Figure 4-10** Spectrum of the femtosecond white light continuum. The hatched area represents the useful spectral region. The laser wavelength is 800 nm.

Whenever appropriate, differential reflectivity spectra will be presented as well as reflectivity. Differential reflectivity describes the change in reflection with respect to a background reflection signal,  $R_0$ . This is taken to be a reflection spectrum at negative time, and the differential reflectivity is defined as  $\Delta R/R = (R - R_0)/R_0$ .

It is interesting to note that photonic resonances of similar linewidth to those at  $30^\circ$  and  $35^\circ$  in figure 4-8 are the type of feature that will facilitate time resolved measurements; in actual fact, every single feature will show some degree of change under optical pumping, but a sharper photonic resonance will ease the

detection a great deal, as the change in the differential reflectivity can be as high as 30% for sharp resonances<sup>12</sup>. In contrast, the change in the differential reflectivity for a wavelength far away from a photonic resonance is significantly smaller or almost non-existent as can be seen on figure 4-11, where there is a change in differential reflectivity of 30% at 859 nm, which is where the resonance originally lies, a change of 20% at 853 nm where the resonance moves to, and an almost negligible change at 870 nm where there is no photonic resonance.

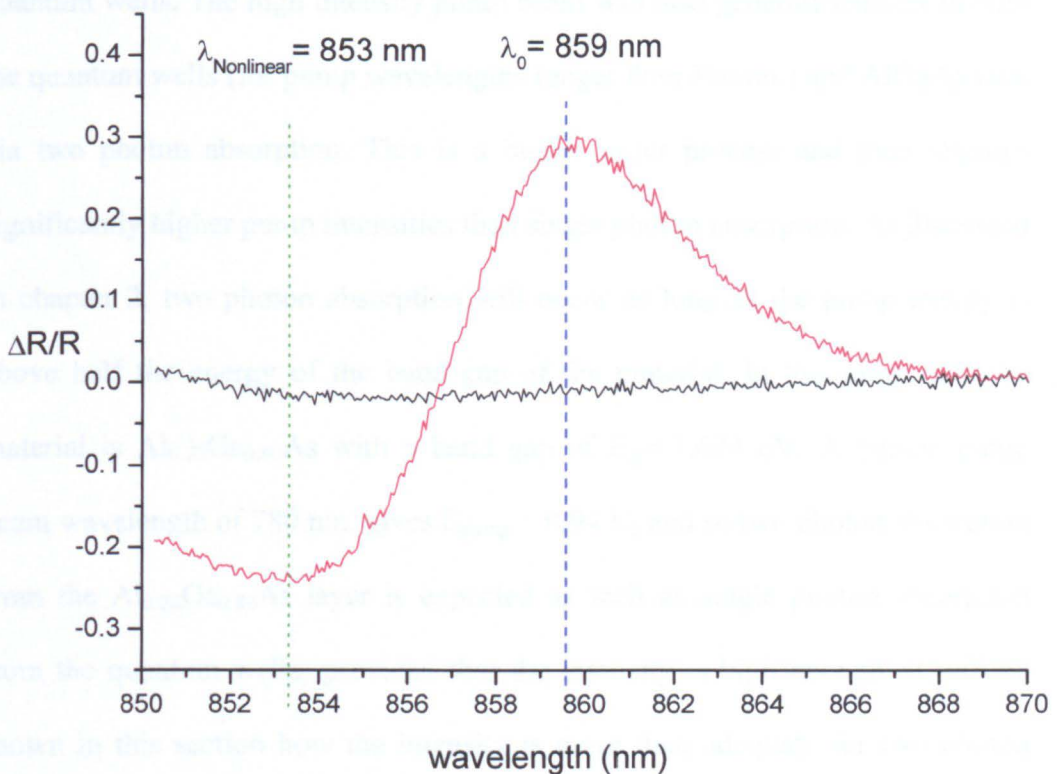


**Figure 4-11** Time resolved differential reflectivity spectra for a sample with period  $a = 675 \text{ nm}$ , air fill factor  $f = 30 \%$  and etch depth  $d = 850 \text{ nm}$ . The black trace shows a negative time delay spectrum while the red trace is at zero delay. The dashed blue line indicates the linear position of the photonic resonance, while the green dotted line represents the position of the photonic resonance at zero time delay.

#### 4.5.2 Single and two photon absorption tuning of photonic resonances.

In this section the nonlinear shift of the photonic resonances due to refractive index changes induced by single and two photon absorption processes will be studied when the samples are pumped in the range 780-820 nm.

Due to the active nature of our samples, pumping at energies above the exciton energy, i.e. energies above 1.55 eV or wavelengths shorter than 800 nm, will result in absorption of the high intensity pump beam and photo creation of carriers will follow. This is due to single photon absorption by the multiple quantum wells. The high intensity pump beam will also generate carriers in both the quantum wells (for pump wavelengths longer than 800 nm) and AlGaAs core via two photon absorption. This is a higher order process and thus requires significantly higher pump intensities than single photon absorption. As discussed in chapter 2, two photon absorption will occur as long as the pump energy is above half the energy of the band gap of the material. In this case, the core material is  $\text{Al}_{0.20}\text{Ga}_{0.80}\text{As}$  with a band gap of  $E_g = 1.674$  eV. A typical pump beam wavelength of 780 nm, gives  $E_{\text{pump}} = 0.94 E_g$  and so two photon absorption from the  $\text{Al}_{0.20}\text{Ga}_{0.80}\text{As}$  layer is expected as well as single photon absorption from the quantum wells, provided that the intensity is high enough. It will be shown in this section how the intensity is more than adequate for two photon absorption to take place. It should be noted that the AlGaAs core is considerably thicker than the quantum wells. Hence a smaller change in the refractive index of the core can still produce a significant effect.

When the pump energy is below the exciton energy, single photon absorption will not take place in the multiple quantum wells. However two photon absorption will continue to take place, as a typical pump wavelength of 810 nm will lie above half the band gap of  $\text{Al}_{0.20}\text{Ga}_{0.80}\text{As}$  which forms the core of the samples.

It is, thus, expected that the change in the refractive index will be smaller when pumping at energies below the exciton, where carriers will only be created via two photon absorption than when pumping above the exciton, where carriers not only will be created via two photon absorption (in the core) but also through single photon absorption (in the quantum wells). Consequently the shift of the photonic resonance will be larger for the latter case than for the former case.

As discussed above, any pump wavelength shorter than the exciton wavelength will result in photo generation of carriers via single photon absorption and two photon absorption, and a corresponding shift of the photonic resonance. A pump wavelength of 780 nm was selected, with an average power of 250  $\mu\text{W}$ . The diameter of the focused laser spot size was measured to be  $200 \pm 50 \mu\text{m}$  which equates to a fluence  $F = 0.49 \text{ mJ/cm}^2$  or, for a pulse width of  $\tau_p = 130 \text{ fs}$ , an intensity of  $I = 3.45 \text{ GW/cm}^2$ . A temporal step size of 3.3 picoseconds was used in the experiments presented in this chapter. This step size is longer than the rise time, which was measured to be approximately 1 ps (not shown). Experiments with finer temporal resolution will be discussed in the next chapter. The sample used had a period of  $a = 880 \text{ nm}$ , a fill factor  $f = 20\%$  and an etch depth

$d = 850$  nm, it is a low exposure sample. A typical time resolved measurement for these parameters is shown in figure 4-12.

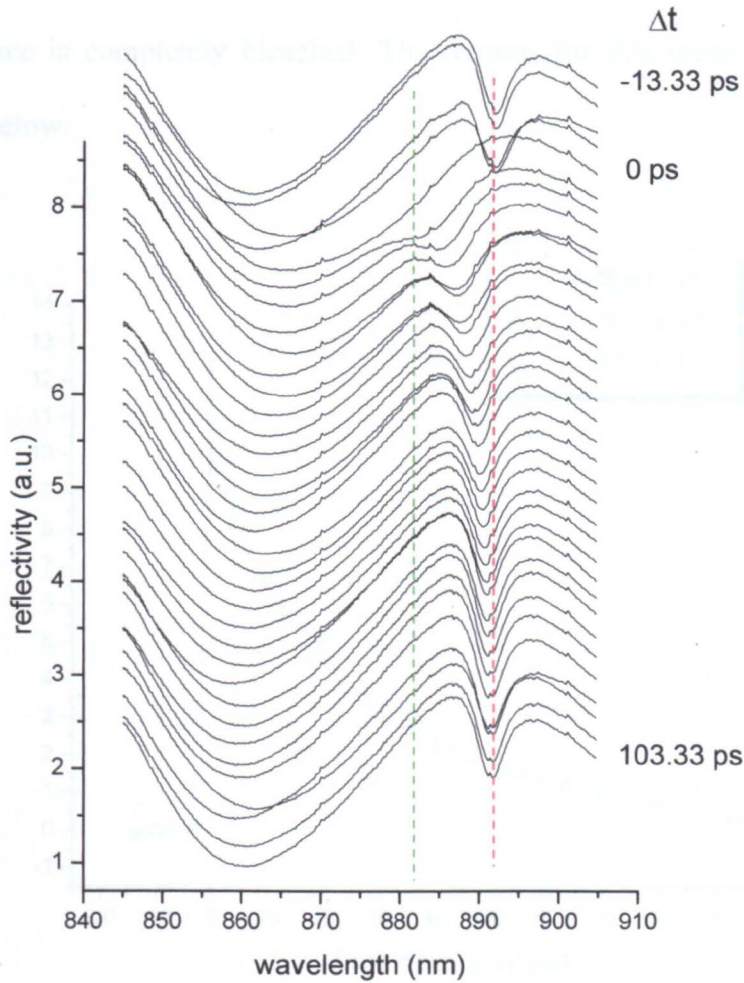


**Figure 4-12** Time resolved reflectivity spectra taken in 3.3 ps steps. Red and green dashed lines indicate positions of the feature at negative delay and zero delay respectively. The sample was from the low exposure set and the sample parameters are as follows: Period  $a = 880$  nm, fill factor  $f = 20\%$  and etch depth  $d = 850$  nm. The pump wavelength is  $\lambda_{\text{pump}} = 780$  nm. The input fluence is  $F = 0.49$  mJ/cm<sup>2</sup>.

A very large shift in the photonic resonance occurs in figure 4-12, approximately  $\Delta\lambda = -11$  nm, where  $\Delta\lambda = \lambda_{\text{linear}} - \lambda_{\text{nonlinear}}$ , at zero time delay. The exact amount of the nonlinear shift near zero time delay is impossible to ascertain correctly as the resonance is completely bleached. The reasons for this bleaching will be discussed below.

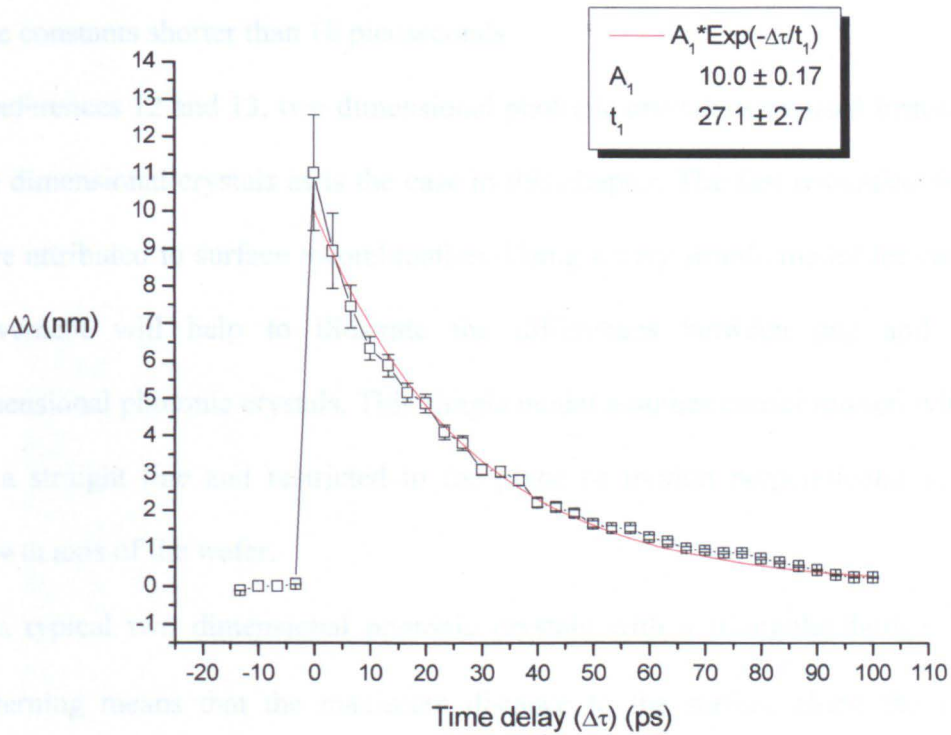


**Figure 4-13** Plot of  $\Delta\lambda$  versus time delay. The open squares represent experimental data extracted from figure 4-12. The red line is a first order exponential decay fit. The fit parameters are presented in the shadowed box.

The photonic resonance is very sharp with a quality factor  $Q = 200$ , marked by the dashed red line in figure 4-12,  $\lambda_{\text{linear}} = 891$  nm. At zero time delay the resonance is completely bleached. It then quickly recovers to its original shape

and spectral position as the time separation of the pump and the probe decreases. This broadening at zero time delay means that the error in  $\Delta\lambda$  is quite large, as shown in figure 4-13. The position of the resonance at zero time delay is extrapolated back from the position of the resonance at later times.

The first order exponential decay fit reveals a time constant  $\tau = 27.1 \pm 2.7$  ps. This is considerably longer than in previous work by this group<sup>12,13</sup>, which had time constants shorter than 10 picoseconds.

In references 12 and 13, two dimensional photonic crystals were used instead of one dimensional crystals as is the case in this chapter. The fast relaxation times were attributed to surface recombination. Using a very simple model for carrier movement will help to illustrate the differences between one and two dimensional photonic crystals. This simple model assumes carrier motion will be on a straight line and restricted to the plane of motion perpendicular to the growth axis of the wafer.

In a typical two dimensional photonic crystals with a triangular lattice. The patterning means that the maximum distance to the surface along the  $\Gamma$ -M

direction, will be  $l_M = \frac{\sqrt{3}a - 2r}{2}$ , where  $a$  is the photonic crystal lattice period

and  $r$  is the hole radius, while along the  $\Gamma$ -K direction this will be reduced

to  $l_K = \frac{a - 2r}{2}$ . These are the distances from the centre point between two air

cylinders to the surface of an air cylinder along either  $\Gamma$ -M or  $\Gamma$ -K symmetry directions, as shown in figure 4-14. Using the sample parameters of reference

12,  $l_K$  is 145 nm, while  $l_M$  is 400 nm. These distances are less than the distances

travelled by free carriers in bulk AlGaAs where free carriers with a decay time of 100 picoseconds<sup>14</sup> and a carrier velocity of approximately 20000 m/s<sup>15</sup> travel  $\sim 2 \mu\text{m}$ . Consequently, there is a significant probability that surface recombination will occur for the great majority of free carriers as they will all reach a surface before recombining by other channels. Diffusion to the surface is therefore likely to be the limiting factor in the nonlinear response decay time in two dimensional photonic crystals.

This is illustrated in figure 4-14, where a scanning electron micrograph of a two dimensional photonic crystal, shows  $l_K$ ,  $l_M$  and the maximum distance that free carriers could travel in an unpatterned medium.

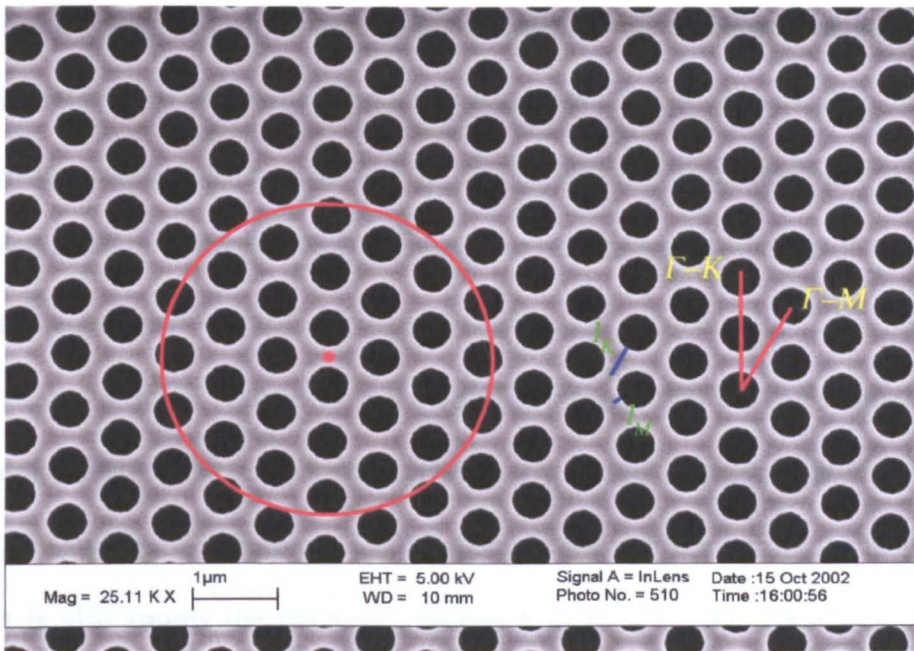


**Figure 4-14** Scanning electron micrograph of a two dimensional photonic crystal with period  $a = 700$  and air fill factor  $f = 30\%$ . The two main lattice directions are marked by red lines.  $l_K$  and  $l_M$  are marked by short blue lines. The red circle represents (approximately) the maximum distance free carriers would travel in an unpatterned medium, i.e.  $2 \mu\text{m}$ , if originally excited from the red dot.

A similar one dimensional lattice will have a maximum distance of half the length of the sample, which in this case is 40  $\mu\text{m}$ . In the periodic direction the maximum distance will be comparable to a two dimensional photonic crystal. This, in essence, means that there will be surface recombination due to the etching of the crystal, but this is only relevant for carriers generated relatively close to any of the surfaces that diffuse towards that surface. The effects of this limited amount of surface recombination can be seen on the time constants, which are longer than reported on reference 13, (approximately 10 picoseconds for a two dimensional photonic crystal) yet shorter than in bulk AlGaAs, where the carrier decay time is approximately 100 picoseconds.

It is quite clear that surface recombination plays a less predominant role in carrier relaxation in one dimensional photonic crystals than it does in two dimensional photonic crystal due to the different lattice topology. A more detailed account of the role played by surface recombination will be discussed in the next chapter.

The second striking feature from the data, is the apparent disappearance of the photonic feature at zero time delay. The high intensity pump beam,  $I = 3.45 \text{ GW/cm}^2$ , not only causes the photonic resonance to shift in wavelength, but it also causes the photonic resonance to bleach. This bleaching can be explained if we assume that the high intensity pump not only induces a large change in the real part of the refractive index change but also causes a change in the imaginary component of the refractive index. This imaginary part of the refractive index causes the photonic resonance to disappear, as shown in figure

4-9. Typically, free carrier absorption can be responsible for induced absorption in pump-probe experiments; however, the absorption caused by free carrier absorption at this wavelength is negligible. Other mechanisms responsible for absorption include band gap renormalization and inter-valence absorption. The photonic resonances are simply too far away from the band gap for band gap renormalization to be responsible for the absorption. Inter-valence band absorption effects are also too far away in the infrared to be responsible for the absorption. At this point the mechanism responsible for the absorption remains unknown.

It is only for small shifts of the photonic resonance that the coupling strength is approximately maintained and thus the photonic resonance approximately maintains its strength and linewidth. This is apparent in the experimental data at long time delays in figure 4-12. A purer shift of the photonic resonance can be seen on figure 4-17, at similar pump intensities.

Figure 4-15 shows power dependent measurements performed on a sample with period  $a = 860$  nm, air fill factor  $f = 20\%$ , etch depth  $d = 850$  nm and low exposure dose. The pump wavelength was set to 780 nm. The average pump power ranged from 0 to 150  $\mu\text{W}$ , i.e. fluence ranging from  $0 \leq F \leq 0.44$   $\text{mJ}/\text{cm}^2$ , or intensity  $0 \leq I \leq 3.3$   $\text{GW}/\text{cm}^2$ . This measurement was taken with an altered laser spot size of approximately  $150 \pm 50$   $\mu\text{m}$ .

As discussed before in this section, single photon absorption as well as two photon absorption are responsible for photo generated carriers for pump wavelengths shorter than the exciton wavelength, approximately 799 nm, and

longer than the electronic band gap of AlGaAs, in this case 740 nm. A pump wavelength of 780 nm ensures this is the case.

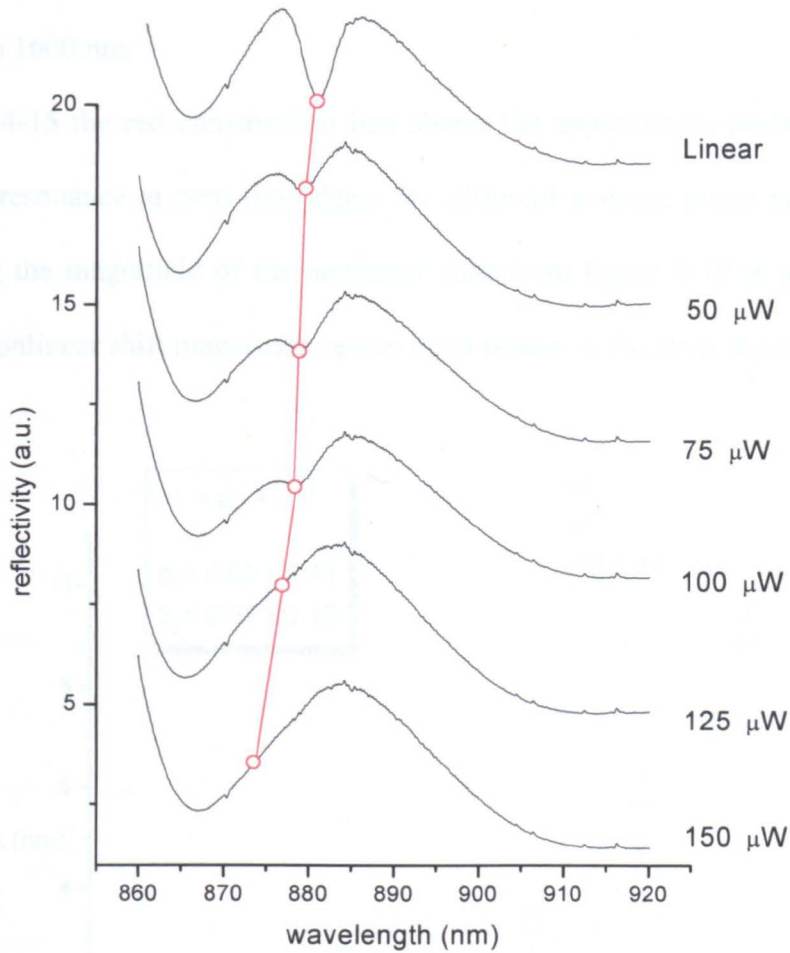


**Figure 4-15** Power dependent reflectivity spectra plotted at zero time delay. The red construction line indicates the position of the photonic resonance. The sample details are as follows: period  $a = 860$  nm, air fill factor  $f = 20\%$ , etch depth  $d = 850$  nm and low exposure dose. The pump wavelength was set to 780 nm.

Pump wavelengths longer than the exciton wavelength will not be absorbed by the multiple quantum wells exciton, and consequently single photon absorption will not occur. However, two photon absorption will still occur in the AlGaAs

core, providing that the pump wavelength is between 1480 and 740 nm. In actual fact, two photon absorption can also occur in the quantum wells<sup>16,17</sup>, and therefore the wavelength range in which two photon absorption should be from 740 nm to 1600 nm.

In figure 4-15 the red construction line shows the approximate position of the photonic resonance at zero time delay for different average pump powers. By extracting the magnitude of the nonlinear shift from figure 4-15 is possible to plot the nonlinear shift magnitude versus input power as shown in figure 4-16.

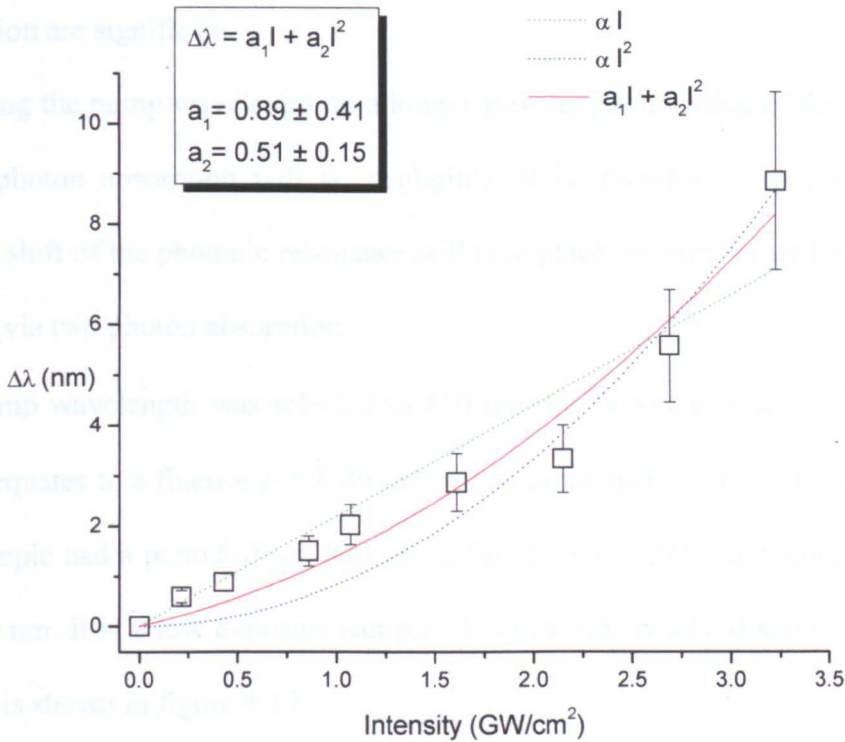


**Figure 4-16** Power dependence plot extracted from figure 4-15. The data points are marked by open squares. The red trace is a parabolic fit to the data points with the origin set to zero. Green dotted line is a linear fit. Blue dotted line is a quadratic fit.

Single photon absorption is expected to have a linear dependence with intensity<sup>18</sup>. This is shown by the green dotted line in figure 4-16, which is a linear fit to the data points. The agreement is quite good at low intensities,  $I < 1 \text{ GW/cm}^2$ . Two photon absorption on the other hand is expected to have a quadratic dependence on the pump intensity, see equation 2.25. This quadratic dependence is shown by the blue dotted line in figure 4-16.

The best overall agreement achieved, as shown by the red trace, includes both a linear and a quadratic term with origin at zero and fit parameters  $a_1 = 0.89 \pm 0.4$  and  $a_2 = 0.51 \pm 0.15$ . This implies that both single photon and two photon absorption are significant.

By tuning the pump wavelength to a longer wavelength than that of the exciton, single photon absorption will be negligible. It is, therefore, expected that a smaller shift of the photonic resonance will take place, as carriers are only being created via two photon absorption.

The pump wavelength was selected to 810 nm, the power was set to 250  $\mu\text{W}$ , which equates to a fluence  $F = 0.49 \text{ mJ/cm}^2$  or an intensity of  $I = 3.45 \text{ GW/cm}^2$ . The sample had a period of  $a = 860 \text{ nm}$ , a fill factor  $f = 20 \%$  and an etch depth  $d = 850 \text{ nm}$ . It is a low exposure sample. A set of time resolved spectra for this sample is shown in figure 4-17.

The photonic resonance, originally located at 881 nm, can be seen to blueshift and broaden at zero time delay. As the temporal delay between the pump and the probe increases, the resonance quickly shifts back to its original position. The nonlinear shift is markedly smaller on figure 4-17, than it is in figure 4-12. This

can be better appreciated in figure 4-18 a), where we that the maximum value for  $\Delta\lambda$  is 4.5 nm as opposed to 11 nm.

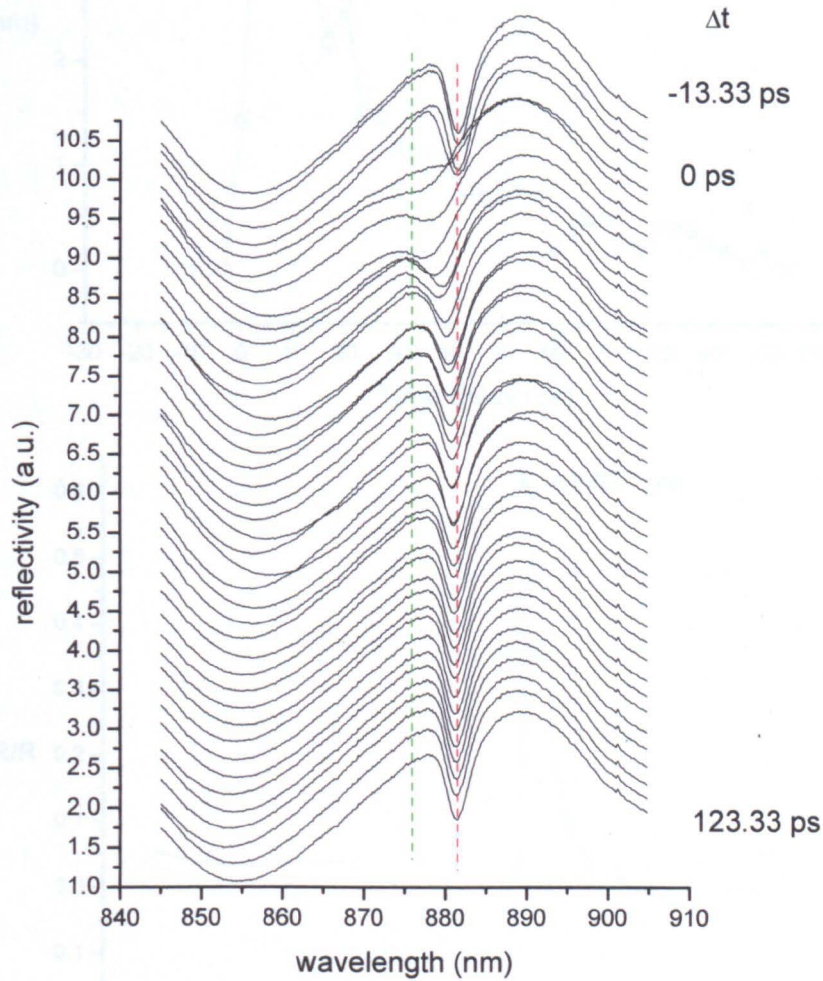


**Figure 4-17** Time resolved reflectivity spectra. Red and green dashed lines indicate positions of the resonance at negative delay and zero time delay respectively. The sample was from the low exposure set and the parameters as follows: Period  $a = 860$  nm, fill factor  $f = 20\%$  and etch depth  $d = 850$  nm. The pump wavelength is  $\lambda_p = 810$  nm and the fluence  $F = 0.49$  mJ/cm<sup>2</sup>.

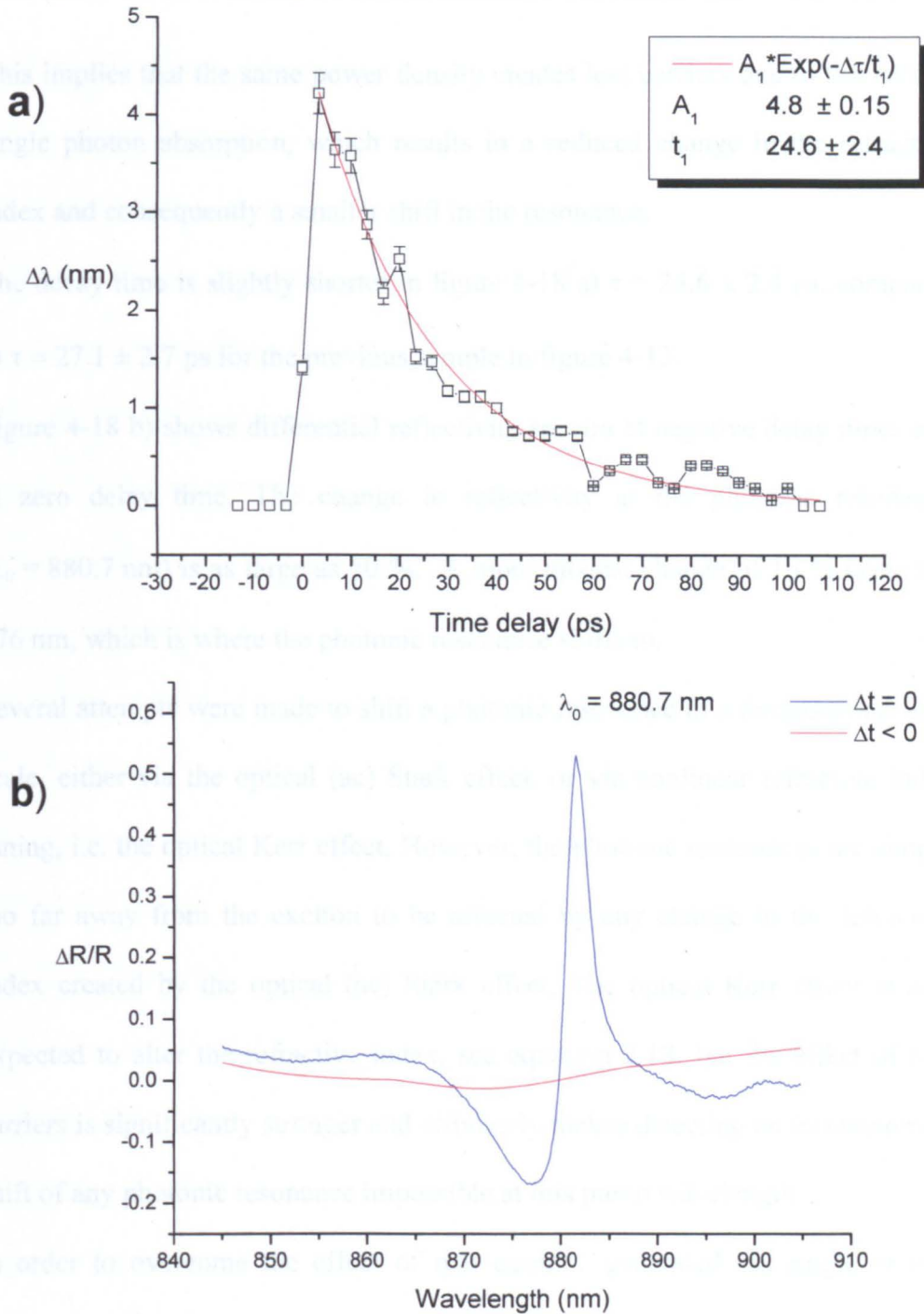


**Figure 4-18 a)** Plot of  $\Delta\lambda$  versus time delay. The open squares represent experimental data extracted from figure 4-17. The red line is a first order exponential decay fit. Fit parameters are presented in the shadowed box. **b)** Differential Reflectivity plot extracted from figure 4-17. The red trace shows negative time delay, whereas the blue trace shows the differential reflectivity at zero time delay.

This implies that the same power density creates less carriers due to the lack of single photon absorption, which results in a reduced change in the refractive index and consequently a smaller shift in the resonance.

The decay time is slightly shorter in figure 4-18 a)  $\tau = 24.6 \pm 2.4$  ps, compared to  $\tau = 27.1 \pm 2.7$  ps for the previous sample in figure 4-13.

Figure 4-18 b) shows differential reflectivity spectra at negative delay times and at zero delay time. The change in reflectivity at the photonic resonance ( $\lambda_0 = 880.7$  nm) is as large as 50 %. A more modest change of 15 % occurs at 876 nm, which is where the photonic resonance shifts to.

Several attempts were made to shift a photonic resonance in a femtosecond time scale, either via the optical (ac) Stark effect, or via nonlinear refractive index tuning, i.e. the optical Kerr effect. However, the photonic resonances are simply too far away from the exciton to be affected by any change in the refractive index created by the optical (ac) Stark effect. The optical Kerr effect is also expected to alter the refractive index, see equation 2.18, but the effect of real carriers is significantly stronger and ultimately makes detecting an instantaneous shift of any photonic resonance impossible at this pump wavelength.

In order to overcome the effect of real carriers, generated via single or two photon absorption, it was decided to set the pump wavelength in the infrared beyond 1600 nm, as this would get rid of two photon absorption and therefore reduce the number of generated real carriers. These experiments are described in the next section.

#### 4.4.2 Two and Three photon absorption tuning of photonic resonances.

In this section, two and three photon absorption will be used to tune the photonic resonance, in much the same way as in the previous section. The key difference is that the pump wavelength will be in the infrared region of the spectrum, ranging from 1250 nm to 2135 nm.

The pump beam focusing lens was changed. A calcium fluoride lens with focal length  $f = 15$  cm was used as BK7 behaves less than adequately at wavelengths above 1.8-2  $\mu\text{m}$ . The lens was also repositioned, and the laser spot size remeasured. A value of  $100 \pm 50$   $\mu\text{m}$  was determined. The relatively large error, comparable with the measured value, is due to the accuracy of the equipment used to measure it. Estimations of fluence and intensity will undoubtedly suffer from this lack of accuracy. It should be noted, though, that relative trends will still be valid. The bigger laser spot size obtained from the BK7 lens in the previous section ensures that a more accurate measurement was made.

The pump wavelength was set to 1330 nm, using the signal beam from the TOPAS OPA, which is collinear with the idler beam at 1950 nm. The same sample that was last measured for two photon absorption tuning of the photonic resonance is again used here, see data of figure 4-17, i.e. Period  $a = 860$  nm, fill factor  $f = 20$  % and etch depth  $d = 850$  nm. It is a low exposure sample. The average pump power was set to 300  $\mu\text{W}$ , which gives a fluence of  $F = 2.15$   $\text{mJ}/\text{cm}^2$  or a power density of  $I = 16.6$   $\text{GW}/\text{cm}^2$ . A typical time resolved measurement is shown in figure 4-19.

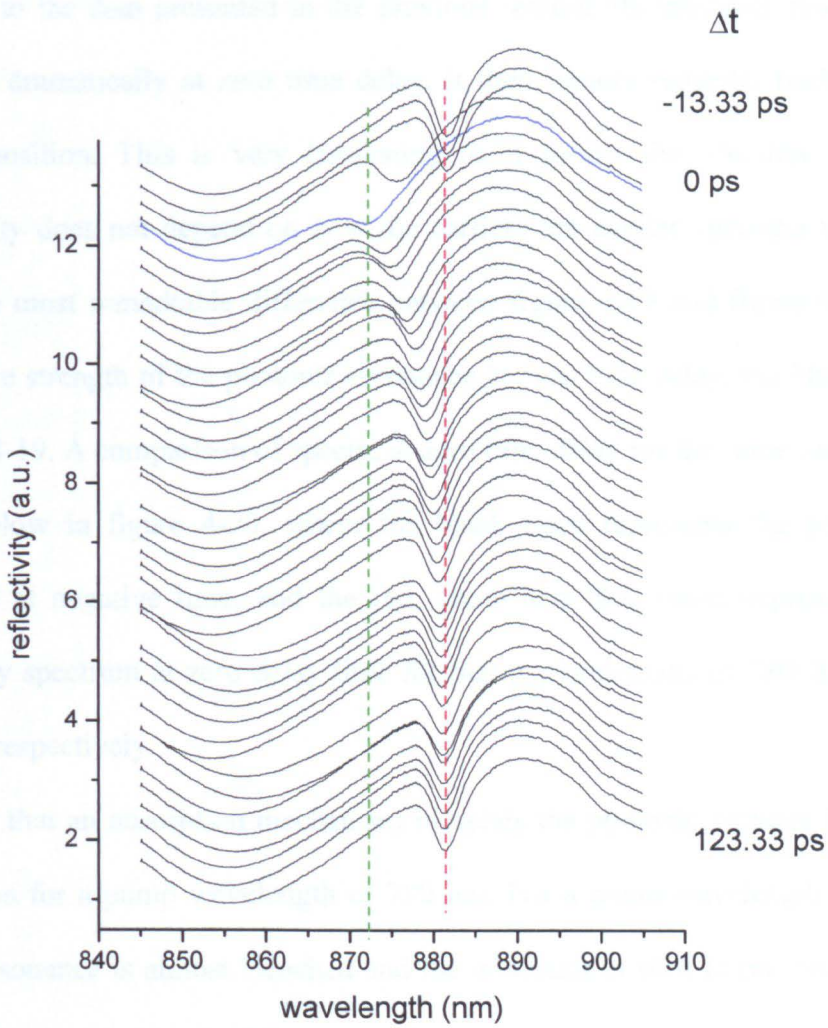


**Figure 4-19** Time resolved reflectivity spectra. Red and green dashed lines indicate positions of the feature at negative delay and zero delay respectively. The sample was from the low exposure set and the parameters as follows: Period  $a = 860$  nm, fill factor  $f = 20$  % and etch depth  $d = 850$  nm. The pump wavelength is  $\lambda_{\text{pump}} = 1330$  nm and the fluence is  $F = 2.15$  mJ/cm<sup>2</sup>.

Similarly to the data presented in the previous section, the photonic resonance blueshifts dramatically at zero time delay, it then rapidly redshifts back to its original position. This is very interesting as it means that the free carrier nonlinearity does not depend on how the carriers are excited onto the valence band. The most remarkable difference between figure 4-19 and figure 4-17, is the relative strength of the photonic resonance at zero time delay, the blue trace in figure 4-19. A comparison of spectra at zero time delay for the same sample is shown below in figure 4-20, where the black trace represents the photonic resonance at negative time, and the red, green and blue traces represent the reflectivity spectrum at zero delay time for pump wavelengths of 780, 810 and 1330 nm respectively.

It is clear that an absorption mechanism bleaches the photonic features beyond recognition for a pump wavelength of 780 nm. For a pump wavelength of 810 nm the resonance is almost bleached and the nonlinear shift is smaller, while for a pump wavelength of 1330 nm there is a reduction on the resonance strength but it is marginal when compared with pump wavelengths of 810 nm and especially 780 nm.

The origin of this mechanism remains unknown. It is clear that free carrier absorption is not responsible for the bleaching as the absorption at the wavelengths of interest is almost negligible. Further work will be needed to clarify the different absorption mechanisms that are involved.

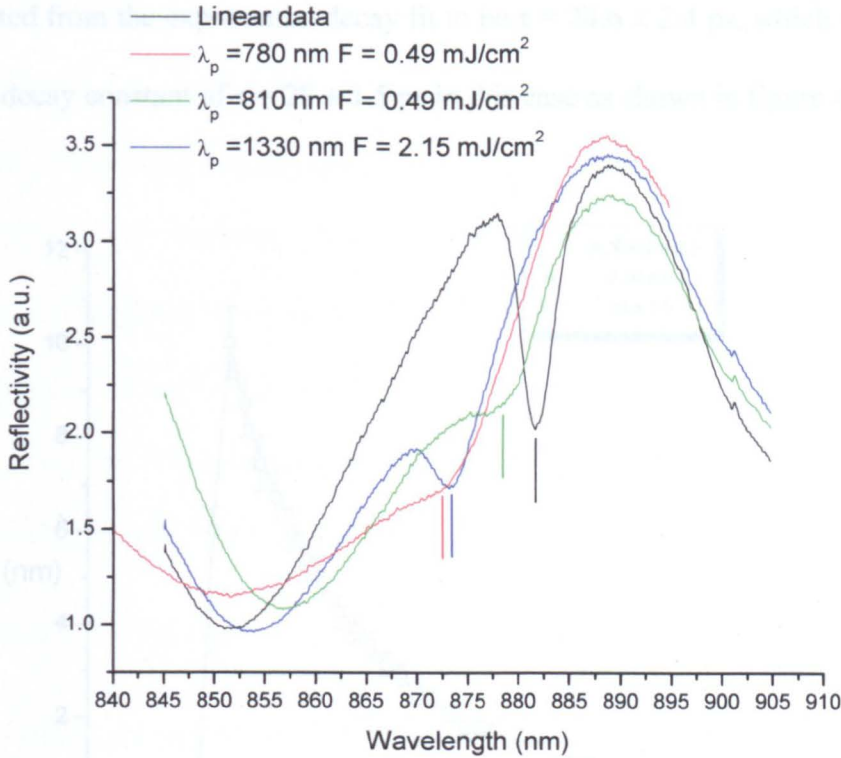


**Figure 4-20** Spectra comparison plot at zero time delay for three different pump wavelengths. The black trace is a linear spectrum. The coloured traces are nonlinear spectra. Coloured vertical lines indicate the position of the photonic resonance. Sample parameters as follows: Period  $a = 860 \text{ nm}$ , fill factor  $f = 20 \%$  and etch depth  $d = 850 \text{ nm}$ . Note the higher fluence for the 1330 nm data.

In the previous section the bleaching of the photonic resonance at zero time delay made judging the actual nonlinear shift of the resonance very hard. In this section, however, the bleaching of the photonic resonance is less pronounced, which makes the job of estimating the nonlinear shift of the resonance significantly easier and makes the fit to the decay slightly more reliable. It is apparent in figure 4-21 that the decay time in this measurement is slightly longer than for previous measurements involving two photon absorption only at a wavelength of 810 nm, see figure 4-18 a), where the decay constant was

estimated from the exponential decay fit to be  $\tau = 24.6 \pm 2.4$  ps, which compares with a decay constant of  $\tau = 28 \pm 1.5$  ps in this case as shown in figure 4-21.

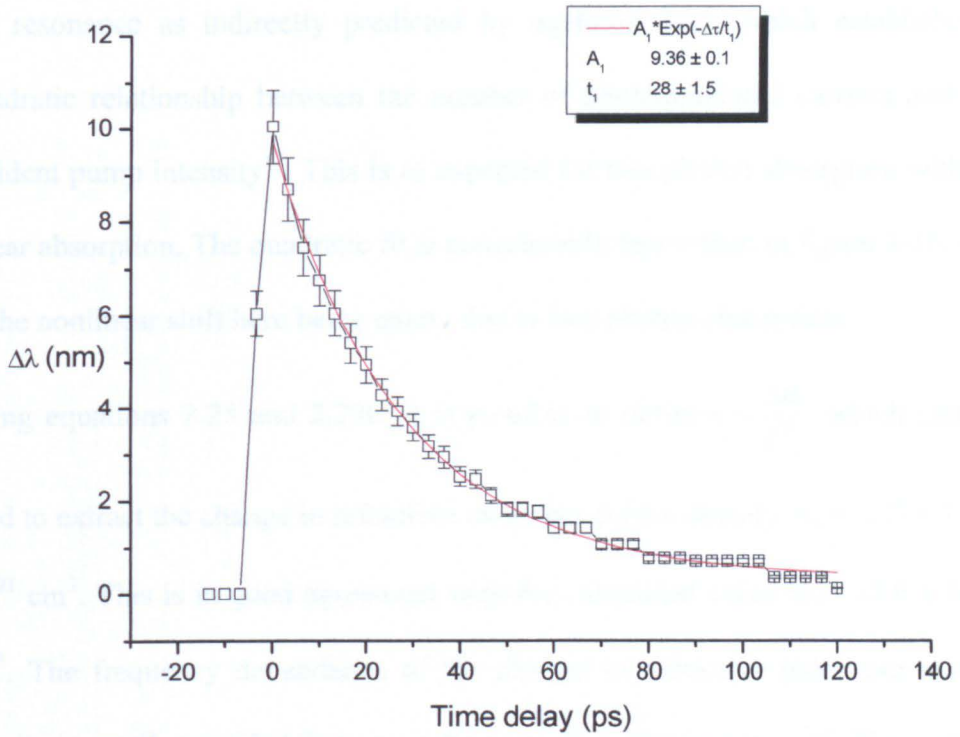


**Figure 4-21** Plot of  $\Delta\lambda$  versus time delay. The open squares represent experimental data extracted from figure 4-19. Red line is a first order exponential decay fit. The fit parameters are presented in the shadowed box.

While the decay constant extracted from the fitted single exponential decay in figure 4-21 is slightly longer than expected, it is consistent with measurements on the same sample at different powers and at different pump wavelengths as shown in table 4-1.



## **IMAGING SERVICES NORTH**

Boston Spa, Wetherby

West Yorkshire, LS23 7BQ

[www.bl.uk](http://www.bl.uk)

**MISSING PAGES ARE  
UNAVAILABLE**

Extracting the magnitude of the nonlinear shift allows for plotting the shift magnitude versus pump power as shown in figure 4-23. It is apparent that a quadratic relationship occurs between the pump power and the nonlinear shift of the resonance as indirectly predicted by equation 2.25, which establishes a quadratic relationship between the number of photogenerated carriers and the incident pump intensity<sup>19</sup>. This is as expected for two photon absorption with no linear absorption. The quadratic fit is considerably better than in figure 4-16, due to the nonlinear shift here being solely due to two photon absorption.

Using equations 2.25 and 2.29b, it is possible to define  $x = \frac{\Delta n}{I^2}$ , which can be used to extract the change in refractive index per carrier density  $\sigma_N = -2.3 \pm 1.1 \times 10^{-21} \text{ cm}^3$ . This is in good agreement with the calculated value  $\sigma_N = -4.9 \times 10^{-21} \text{ cm}^3$ . The frequency dependence of the change in refractive index per carrier density is small, provided that one is far away from the resonance<sup>20</sup>. The error in the measured value is large, due to the accumulated errors, e.g. laser spot size, pump beam average power.

Once the setup has been thoroughly tested at infrared wavelengths, the wavelength was changed to 2050 nm. This will ensure that photo generation of free carriers via two photon absorption will be negligible. However, three photon absorption as a mechanism for photo generation of free carriers is still present at this wavelength, although a significantly higher threshold is expected as this is a higher order process mediated by  $\chi^{(5)}$ <sup>21</sup>. Three photon absorption is expected as the pump energy is between one third and one half of the band gap, with the

band gap for  $\text{Al}_{0.20}\text{Ga}_{0.80}\text{As}$  being  $E_g = 1.674$  eV, the former is  $E_{g1/3} = 0.558$  eV ( $\lambda = 2220$  nm) whereas the latter is  $E_{g1/2} = 0.837$  eV ( $\lambda = 1480$  nm).

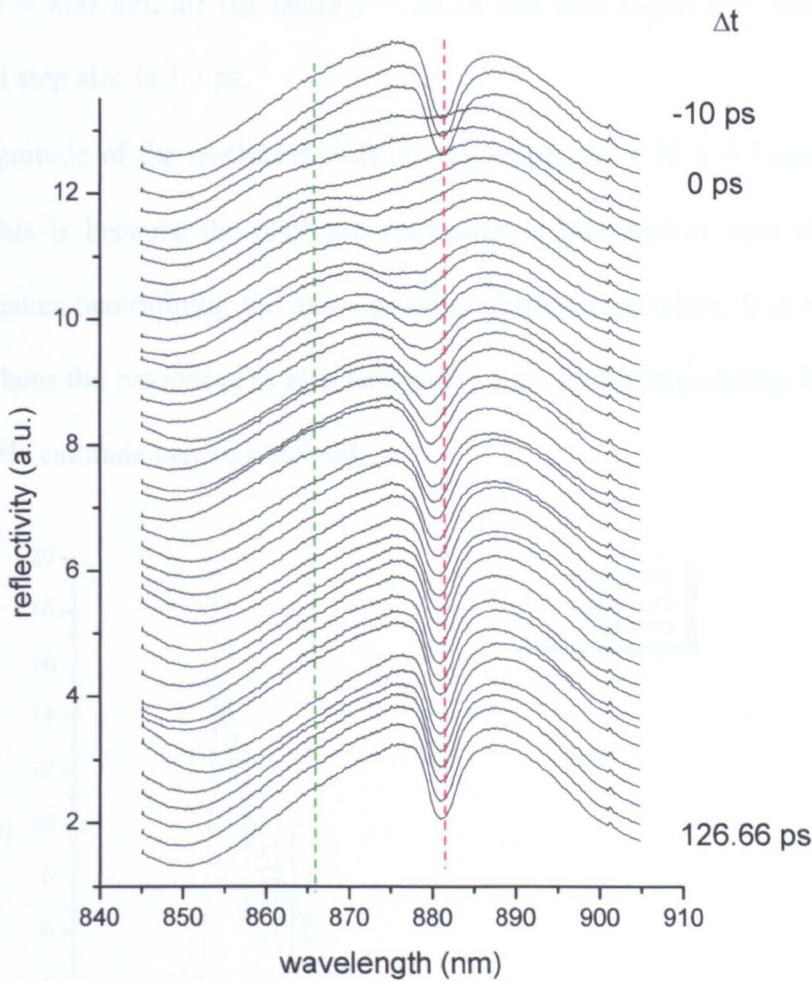


**Figure 4-24** Time resolved reflectivity spectra. Red and green dashed lines indicate positions of the feature at negative delay and zero delay respectively. The sample was from the low exposure set and the parameters as follows: Period  $a = 860$  nm, fill factor  $f = 20$  % and etch depth  $d = 850$  nm. The pump wavelength is  $\lambda_{\text{pump}} = 2050$  nm and the fluence is  $F = 2.15$  mJ/cm<sup>2</sup>.

Figure 4-24 shows the time resolved reflectivity spectra for a pump wavelength

of  $\lambda = 2050$  nm and a fluence of  $F = 2.15$  mJ/cm<sup>2</sup> or a power density of  $I = 16.58$  GW/cm<sup>2</sup>. This is the same fluence used in the previous measurement with a wavelength of  $\lambda = 1330$  nm on the same sample used in this section, with period  $a = 860$  nm, air fill factor  $f = 20$  % and etch depth  $d = 850$  nm. The temporal step size is 3.3 ps.

The magnitude of the nonlinear shift is very large,  $\Delta\lambda = 15 \pm 4.5$  nm, as is the error. This is because the photonic resonance is bleached at zero time delay, which makes determining the exact position almost impossible. It is by looking at the where the resonance is at a later delay time and extrapolating back that a reasonable estimate can be obtained.

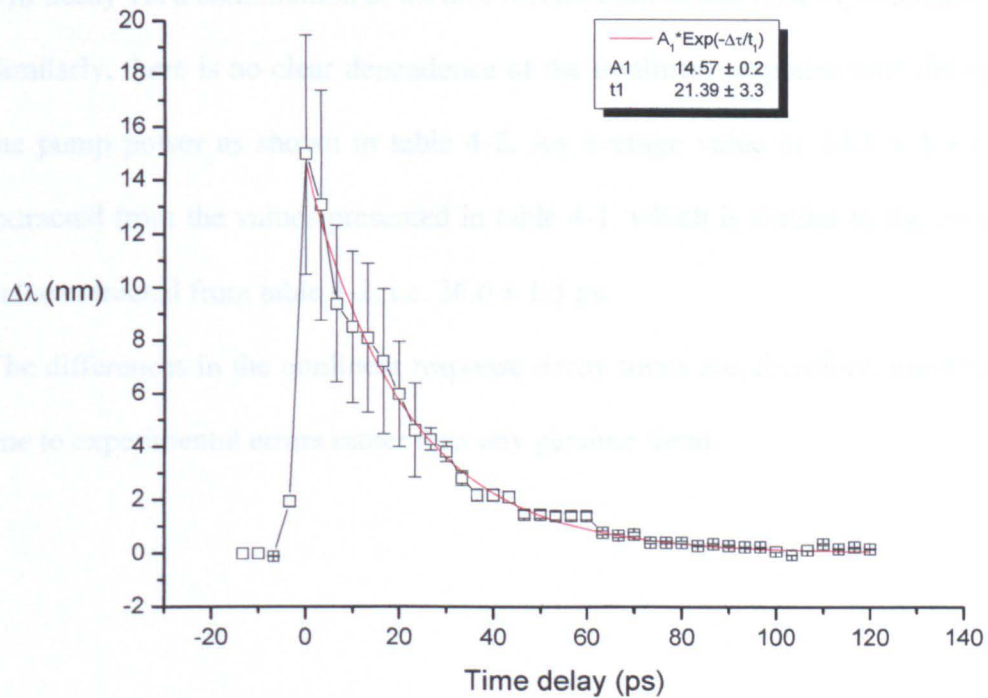


**Figure 4-25** Plot of  $\Delta\lambda$  versus time delay. The open squares represent experimental data extracted from figure 4-24. The red line is a first order exponential decay fit to the experimental data. The fit parameters are presented in shadowed box.

The decay constant is shorter than for other measurements on this sample at different wavelengths,  $\tau = 21.4 \pm 3.5$  ps as shown in figure 4-25, compared with  $\tau = 28 \pm 1.5$  ps for a pump wavelength of  $\lambda = 1330$  nm,  $\tau = 24.6 \pm 2.4$  ps for a pump wavelength of  $\lambda = 810$  nm and  $\tau = 24 \pm 2.9$  ps for a pump wavelength of  $\lambda = 780$  nm.

A summary of these results is presented in table 4-1. Also a summary of nonlinear response time decay versus average input pump power is shown in table 4-2.

There is no clear relationship between the pump wavelength and the decay time.

This is indeed to be expected as once the free carriers have been created they will decay via a combination of surface recombination and bulk recombination.

Similarly, there is no clear dependence of the nonlinear response time decay on the pump power as shown in table 4-2. An average value of  $24.5 \pm 1.4$  ps is extracted from the values presented in table 4-1, which is similar to the average value extracted from table 4-2, i.e.  $26.6 \pm 1.5$  ps.

The differences in the nonlinear response decay times are, therefore, most likely due to experimental errors rather than any genuine trend.

**Table 4.1 Time decay for different pump wavelengths (See text for details of input power)**

Pump Wavelength (nm)	Time Decay (ps)	Error (ps)
780	24	2.9
810	24.6	2.4
1330	28	1.5
2050	21.4	3.3

**Table 4.2 Time decay values for different input powers. Pump wavelength  $\lambda_{\text{pump}} = 810$  nm.**

Average Input Power (mW)	Input Fluence (mJ/cm <sup>2</sup> )	Time Decay (ps)	Error (ps)
150	1.03	30	3.3
200	1.37	23.33	3.3
250	1.7	26.7	2.5
325	2.19	24.3	3.5
375	2.53	28.4	5.3

The sample details used for the above tables are as follows: period  $a = 860$  nm, air fill factor  $f = 20\%$  etch depth  $d = 850$  nm, low exposure set.

In the simplest approximation the three photon absorption coefficient can be defined by  $\frac{dI}{dz} = -\gamma I^3$ , where  $\gamma$  is the three photon absorption coefficient of the medium and is sometimes expressed as either  $\beta_3$  or  $\alpha_3$ . It is therefore expected that nonlinear shift in the photonic resonance will present a cubic dependence on the intensity.

While there is a wealth of measurements of the two photon absorption coefficient of Al(GaAs)<sup>22,23,24</sup>, there is a lack of measurements of the three photon absorption coefficient<sup>25</sup>, particularly so at the range of wavelengths of interest, i.e. 2050 – 2150 nm. The three photon absorption coefficient can be calculated using the following formula<sup>26</sup>:

$$\gamma = \frac{3^{10} \sqrt{2}}{8} \pi^2 \left( \frac{e^2}{\hbar c} \right)^3 \frac{\hbar^2 P^2 \sqrt{3\hbar\omega / E_g - 1}}{n^3 E_g^7 (3\hbar\omega / E_g)^9} \quad (4.3)$$

where  $P$  is the Kane momentum parameter, extracted from  $E_p = \frac{2P^2 m}{\hbar^2}$ , which is a momentum matrix element<sup>27</sup> and has a value of ~21 eV for most direct band gap semiconductors<sup>23,27</sup>.  $E_g$  is the band gap energy,  $\omega$  is the angular frequency of the photon and  $n$  is the refractive index of the material.

A three photon absorption coefficient of approximately  $\gamma = 0.3 \times 10^{-18} \text{ cm}^3 \text{ W}^{-2}$  is found upon substitution for the wavelength range of interest.

Power dependent measurements were performed at this wavelength on the same sample as for figure 4-24, i.e. period  $a = 860$  nm, air fill factor  $f = 20$  %, etch depth  $d = 850$  nm and low exposure dose. The pump wavelength is set to 2100 nm. The average pump power ranged from zero to 350  $\mu\text{W}$ , which is

equivalent to a range in fluences of  $0 \leq F \leq 2.51 \text{ mJ/cm}^2$  or intensities of  $0 \leq I \leq 19.14 \text{ GW/cm}^2$ .

For average pump powers in excess of  $350 \text{ }\mu\text{W}$ , the position of the photonic resonance at zero time delay is determined by indirect means as described above, due to it being completely bleached.

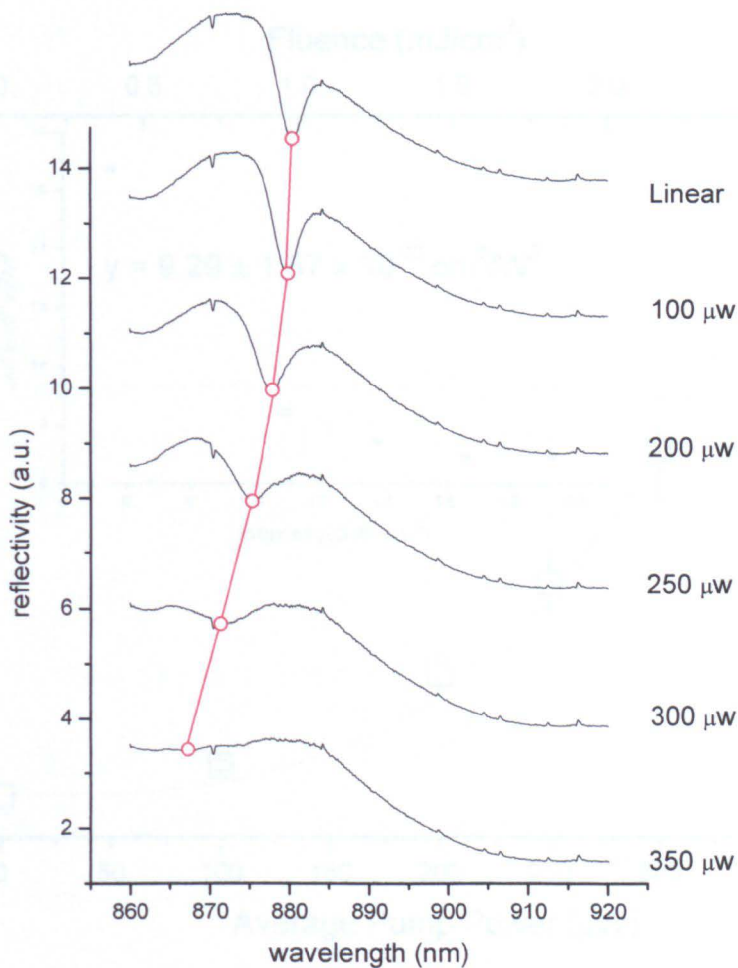


**Figure 4-26** Power dependence plot. Reflectivity spectra are plotted at zero time delay. The red construction line indicates the position of the photonic resonance for each pump power. The sample was from the low exposure set and the parameters are as follows: Period  $a = 860 \text{ nm}$ , air fill factor  $f = 20 \%$  and etch depth  $d = 850 \text{ nm}$ . The pump wavelength is  $\lambda_{\text{pump}} = 2100 \text{ nm}$

In figure 4-26 the red construction line shows the approximate position of the photonic resonance at zero time delay. Note how the feature is completely bleached for an average pump power of 350  $\mu\text{W}$ .

Extracting the magnitude of the nonlinear shift allows for plotting the shift magnitude versus pump power as shown in figure 4-27.

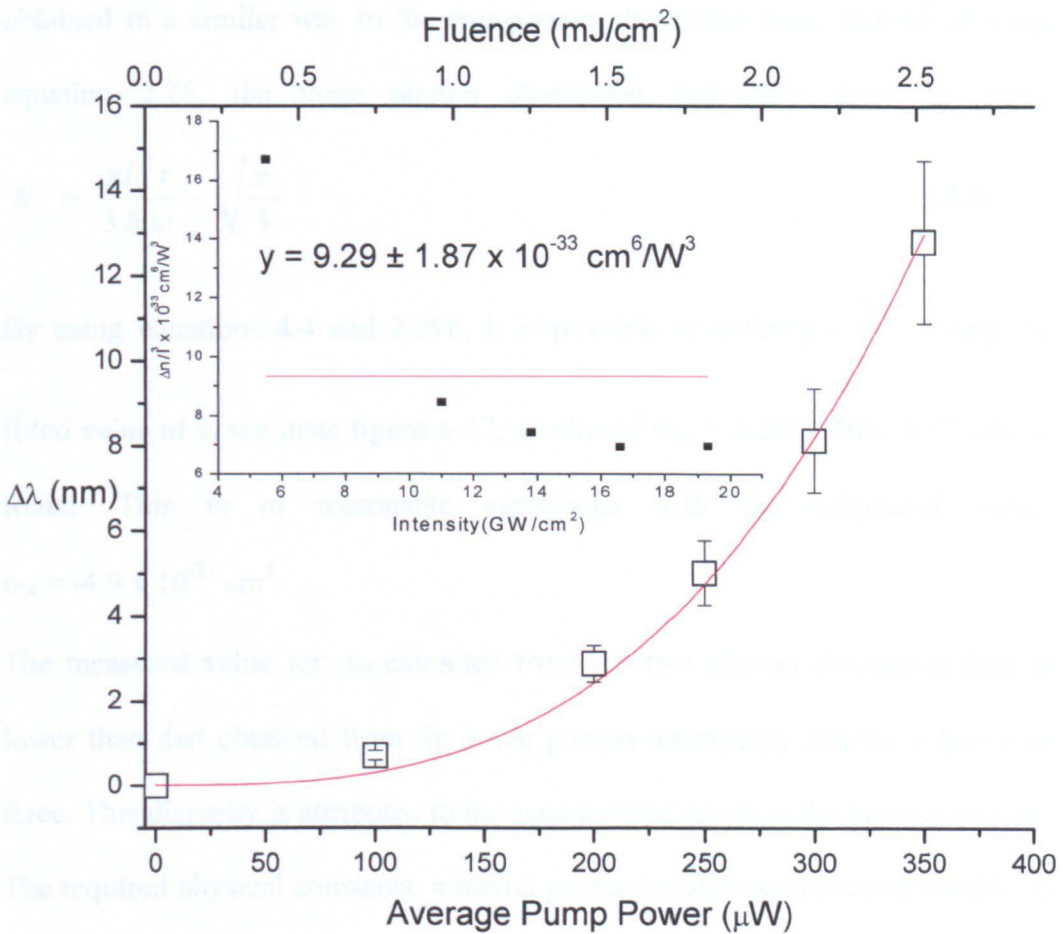


**Figure 4-27** Power dependence plot. The data points are marked by open squares. The red trace is a cubic fit to the data points. The inset shows the refractive index change divided by the cube of the pump intensity.

In contrast with the two photon absorption dominated nonlinear shift at 1250 nm, shown in figure 4-23, which shows a quadratic relationship with the intensity of the pump power, it is expected that this three photon absorption dominated nonlinear shift will present a cubic relationship with input intensity, see equation 4.4. Figure 4-27 shows that this is indeed the case.

An estimate of the refractive index change per carrier density,  $\sigma_N$  can also be obtained in a similar way to the two photon absorption case. Instead of using equation 2.25, the three photon absorption equivalent must be used:

$$N = \frac{\gamma I_0^3 \tau_p}{3 \hbar \omega_p} \sqrt{\frac{\pi}{3}} \quad (4.4)$$

By using equations 4.4 and 2.29b, it is possible to define  $y = \frac{\Delta n}{I^3}$ . Using the fitted value of  $y$ , see inset figure 4-27, a value of  $\sigma_N = -6.59 \pm 10 \times 10^{-20} \text{ cm}^3$  is found. This is in reasonable agreement with the calculated value,  $\sigma_N = -4.9 \times 10^{-21} \text{ cm}^3$ .

The measured value for  $\sigma_N$  extracted from the two photon absorption data is lower than that obtained from the three photon absorption data by a factor of three. This disparity is attributed to the accumulated errors in the measurements. The required physical constants, material properties and experimental conditions to calculate  $\sigma_N$  and  $N$  are summarised in table 4.3.

**Table 4.3** Parameters required to calculate  $\sigma_N$  and  $N$ 

<b>Physical Constants</b>			
$e$	Electronic charge	$1.602 \times 10^{-19} \text{ C}$	
$m_0$	Electronic rest mass	$9.1 \times 10^{-31} \text{ Kg}$	
$\epsilon_0$	Vacuum permittivity	$8.85 \times 10^{-12} \text{ Fm}^{-1}$	
$h$	Planck's constant / $2\pi$	$1.055 \times 10^{-34} \text{ Js}$	
<b>Material Properties</b>			
$E_g$	Electronic band gap of waveguide core	$1.673 \text{ eV}$	
$n_0$	Refractive index of core at $\sim 880\text{nm}$	$3.45$	
$m_e$	Effective mass of electrons	$0.079 m_0$	
$m_h$	Effective mass of heavy hole	$0.56 m_0$	
$\beta$	Two photon absorption coefficient for AlGaAs	$9 \times 10^{-9} \text{ cm W}^{-1}$	
$\gamma$	Three photon absorption coefficient for AlGaAs	$0.3 \times 10^{-18} \text{ cm}^3 \text{W}^{-2}$	
<b>Experimental Conditions</b>			
$f_{\text{rep}}$	Laser repetition rate	$1 \text{ kHz}$	
$\tau_p$	Laser pulse width	$130 \text{ fs}$	
$r_p$	Focused laser spot radius	$50 \mu\text{m}$	
$\lambda_p$	Pump wavelength	Two photon absorption	$1250 \text{ nm}$
		Three photon	$2100 \text{ nm}$
$\lambda_{\text{pr}}$	Probe wavelength		$880 \text{ nm}$

## 4.5 Conclusions

In this chapter I have demonstrated nonlinear shifting of the photonic resonances via single photon and two photon absorption, two photon alone and three photon absorption.

By using a pump wavelength shorter than the exciton wavelength, yet longer than the electronic band gap of  $\text{Al}_{0.20}\text{Ga}_{0.80}\text{As}$ , ( $\lambda_p = 780$  nm in this case), single and two photon absorption processes created free carriers that changed the refractive index, which ultimately shifted the photonic resonance by approximately  $\Delta\lambda = -11$  nm for a fluence of  $F = 0.49$  mJ/cm<sup>2</sup>. Despite the relatively low fluence, the photonic resonance is completely bleached at zero time delay. A decay time of  $\tau = 27.1 \pm 2.7$  ps is observed. This is longer than for previous work carried out by this group in two dimensional photonic crystals. The different topology of these samples accounts for significantly reduced surface recombination, which was responsible for  $\sim 10$ ps decay times in two dimensional samples. In one dimensional photonic crystals, carriers have, on average, to travel longer distances to reach any surface than in higher dimensionality photonic crystals and consequently the amount of surface recombination taking place is reduced which in turn increases the nonlinear response decay time.

When the pump wavelength is longer than the exciton wavelength,  $\lambda_p = 810$  nm in this case, single photon absorption will not occur, and two photon absorption is the only real carrier creation mechanism. A similar fluence resulted in a smaller shift of the photonic resonance, approximately  $\Delta\lambda = -5$  nm. This smaller

shift is due to two photon absorption being a third order process and consequently having a smaller absorption coefficient, thereby generating less carriers.

Changes in the reflectivity as large as 50 % were observed at the original (unshifted) photonic resonance position, i.e.  $\lambda_{\text{linear}} = 881$  nm. Smaller changes of 15 % were observed at the wavelength the photonic resonance shifted to, i.e.  $\lambda_{\text{nonlinear}} = 876$  nm.

A significantly larger shift,  $\Delta\lambda = -10$  nm, was observed for two photon absorption at pump wavelengths in the infrared,  $\lambda_p = 1330$  nm. The pump fluence was, however markedly larger  $F = 2.15$  mJ/cm<sup>2</sup>. Despite the large pump fluence, the photonic resonance is not bleached, in sharp contrast to the behaviour at shorter wavelengths where the resonance is completely bleached for smaller pump fluences.

A power dependent measurement confirmed a quadratic dependence of the nonlinear shift on the pump intensity. The change of the refractive index per unit carrier density was extracted from the power dependent data and was found to have a value of  $\sigma_N = -2.29 \times 10^{-21}$  cm<sup>3</sup>, which compares favourably with a calculated value of  $\sigma_N = -4.9 \times 10^{-21}$  cm<sup>3</sup>.

A very large shift,  $\Delta\lambda = -15$  nm, is observed for three photon absorption, for a pump wavelength  $\lambda_p = 2050$  nm, for an identical fluence to the infrared two photon absorption case, i.e.  $F = 2.15$  mJ/cm<sup>2</sup>. It should be noted that there is a significant contribution to this shift by the quantum wells which also exhibit three photon absorption. As with the infrared two photon absorption case, a

power dependent measurement was carried out. In contrast to the two photon absorption case, a cubic dependence of the nonlinear shift on the pump intensity was found.

The change of the refractive index per unit carrier density was extracted from the power dependent data and was found to have a value of  $\sigma_N = -6.59 \times 10^{-20} \text{ cm}^3$ , in reasonable agreement with the calculated value of  $\sigma_N = -4.9 \times 10^{-21} \text{ cm}^3$ .

It is clear that the nonlinear change of the refractive index that ultimately causes shifts of the photonic resonances does not depend on how the carriers are excited. It depends solely on the free carrier density generated.

The nonlinear response decay time was found to depend neither on the pump wavelength nor on the input pump power. This is to be expected as once the carriers have been excited to the conduction band, the decay time will be governed by the amount of surface recombination taking place.

The dependence of the nonlinear decay time on the photonic crystal parameters, period and air fill factor, i.e. stripe width and etch depth will be discussed in the next chapter along with the nonlinear response of photonic crystals in femtosecond time scales.

**References:**

1. A. Mysyrowicz, D. Hulin, A. Antonetti, A. Migus, W.T. Masselink, H. Morkoc,” “Dressed excitons” in a multiple quantum well structure: Evidence for an optical stark effect with femtosecond response time” *Phys Rev Lett.* **56**(25) 2748 (1986).
2. R. Dingle, W. Wiegmann, C. H. Henry, “Quantum States of Confined Carriers in Very Thin Al<sub>x</sub>Ga<sub>1-x</sub>As-GaAs-Al<sub>x</sub>Ga<sub>1-x</sub>As Heterostructures” *Phys Rev. Lett.* **33**, 827–830 (1974).
3. Most solid state physics book will have a section on excitons, see for example C. Kittel, “Introduction to Solid State Physics” Wiley (1986).
4. D. S. Chemla and D. A. B. Miller, "Room-Temperature Excitonic Nonlinear-Optical Effects in Semiconductor Quantum-Well Structures," *J. Opt. Soc. Am. B* **2**, 1155 (1985).
5. V.N.Astratov, R.M.Stevenson, M.S.Skolnick. D.M.Whittaker, S. Brand, T.F.Krauss, R.M.De La Rue, O.Z. Karimov, “Experimental technique to determine the band structure of two dimensional photonic lattices” *IEE Proc.- Optoelectro.* **145**, 398 (1998).
6. V.N.Astratov, R.M.Stevenson, I.S.Culshaw, D.M.Whittaker, M.S.Skolnick, T.F.Krauss, R.M.De La Rue, “Heavy photon dispersions in photonic crystal waveguides” *Appl Phys Lett* **77** 178, (2000).
7. A.R. Cowan, Jeff. F. Young, “Mode matching for second-harmonic generation in photonic crystal waveguides” *Phys. Rev. B* **65**, 085106 (2002).
8. D.M. Whittaker, I.S. Culshaw, ” Scattering matrix treatment of patterned multilayer photonic structures” *Phys. Rev. B* **60**, 2610 (1999)
9. See for instance E. Hecht “Optics” Addison-Wesley, (1998).
10. The quality factor, or finesse is defined as  $\frac{\lambda}{\Delta\lambda}$ , where  $\lambda$  is the position of the resonance and  $\Delta\lambda$  is the full width half maximum value.

11. Kurt Busch, Stefan Lölkes, Ralf B. Wehrspohn, Helmut Föll "Photonic Crystals Advances in Design, Fabrication, and Characterization", Wiley (2004).
12. A. D. Bristow, J.-P. R. Wells, W. H. Fan, A. M. Fox, M. S. Skolnick, D. M. Whittaker, A. Tahraoui, T. F. Krauss, J. S. Roberts, "Ultrafast nonlinear response of AlGaAs two-dimensional photonic crystal waveguides" Appl Phys Lett **83**, 851 (2003).
13. A.D. Bristow, D.O. Kundys, A. Z. García-Déniz, J.-P.R. Wells, A.M. Fox, M.S. Skolnick, D.M. Whittaker, A. Tahraoui, T.F. Krauss, J.S. Roberts, "Ultrafast nonlinear tuning of the reflection properties of AlGaAs in photonic crystal waveguides by two-photon absorption," J. Appl. Phys. **96**, 4729 (2004).
14. M. J. LaGasse, K. K. Anderson, C. A. Wang, H. A. Haus and J. G. Fujimoto, "Femtosecond measurements of the nonresonant nonlinear index in AlGaAs," Appl. Phys. Lett. **56**, 417 (1990).
15. D.E. Aspnes, "Recombination at semiconductor surfaces and interfaces" Surf. Sci. **132** 406 (1983).
16. A. Obeidat, J. Khurgin, "Excitonic enhancement of two photon absorption in semiconductor quantum well structures" J. Opt. Soc. Am. B **12**, 1222 (1995).
17. M.N. Islam, C. E. Socolich, R. E. Slusher, A. F. J. Levi, W. S. Hobson, M. G. Young, "Nonlinear spectroscopy near half-gap in bulk and quantum well GaAs/AlGaAs waveguides" J Appl Phys **71** 1927 (1992).
18. The carrier density generated by one photon absorption is given by: 
$$N = \alpha I \tau_p \frac{\sqrt{\pi}}{\hbar \omega_p}$$
19. H. Folliot, M. Lynch, A.L. Bradley, T. Krug, L. A. Dunbar, J. Hegarty, J.F. Donegan, L.P. Barry, "Two photon induced photoconductivity enhancement in semiconductor microcavities: a theoretical investigation" J Opt Soc Am B Vol **19**, No 10, 2396 (2002).

20. T. G. Ulmer, R. K. Tan, Z. Zhou, S. E. Ralph, R. P. Kenan, C. M. Verber and A. J. Spring-Thorpe, "Two-photon absorption induced self-phase modulation in GaAs-AlGaAs waveguides for surface emitted second harmonic generation" *Opt Lett* **24** 756 (1999).
21. The order of the susceptibility tensor responsible for multiple photon absorption goes as  $2n-1$ , where  $n$  is the number of photon involved, see for instance, P.N. Butcher, D. Cotter, "The Elements of Nonlinear Optics", Cambridge University Press (1990).
22. H.Q. Le, H.K. Choi, C.A. Wang, "Measurement of the two-photon absorption coefficient in a GaAs/AlGaAs quantum well laser" *Appl. Phys. Lett.* **57**, 212 (1990).
23. E.W. Van Stryland, M.A. Woodall, H Vanherzeekem, M.J. Soileau, "Energy band gap dependence of two photon absorption" *Opt Lett* **10** 490 (1985).
24. A. Villeneuve, C.C. Yang, G.I Stegeman, Chen-Hui Lin, Hao-Hsiung Lin, "Nonlinear refractive-index and two photon-absorption near half the band gap in AlGaAs" *Appl. Phys. Lett.* **62**, 2465 (1992).
25. J.U. Kang, A. Villeneuve, M. Sheik-Bahe, G.I Stegeman, K. Al-Hemyari, J.S. Aitchison, C. N. Ironside, "Limitation due to three-photon absorption on the useful spectral range for nonlinear optics in AlGaAs below half band gap" *Appl. Phys. Lett.* **65**, 147 (1994).
26. B.S. Wherrett, "Scaling rules for multiphoton interband absorption in semiconductors" *J Opt Soc Am B Vol 1*, No 1, 67 (1984).
27. M. Sheik-Bahae, D.J. Hagan, E.W. Van Stryland, "Dispersion and band-gap scaling of the electronic Kerr effect in solids associated with two-photon absorption" *Phys Rev. Lett.* **65**, 96 (1990).

# **Chapter 5: Nonlinear Switching Properties of 1D Photonic Crystals**

## **5.1. Introduction**

## **5.2. Experimental Setup Modifications**

## **5.3. Nonlinear Response Lifetime Control via Alteration of the Photonic Crystal Waveguide Parameters**

### **5.3.1. Period and Fill Factor (Stripe Width)**

### **5.3.2. Modelling of the Dependence of the Nonlinear Response Lifetime on the Stripe Width**

### **5.3.3. Etch Depth**

## **5.4. Subpicosecond Switching via Virtual Nonlinearities**

### **5.4.1. Subpicosecond Switching via the Nonlinear Kerr Effect**

### **5.4.2. Subpicosecond Switching via the Optical (AC) Stark Effect**

## **5.5. Conclusions**

“Son cinco minutos, la vida es eterna en cinco minutos”

*Te Recuerdo Amanda, Victor Jara*

## 5.1 Introduction

In the previous chapter the nonlinear properties induced by real carriers in one dimensional AlGaAs/InAlGaAs multiple quantum well photonic crystals were measured.

It was found that the carrier decay time was longer than in two dimensional photonic crystals. It was also hinted that the decay time of these free carrier nonlinearities might depend on the period length due to the effects of surface recombination. Surface recombination is responsible for the faster carrier decay in photonic crystals<sup>1</sup> than in bulk<sup>2</sup>.

In this chapter a relationship between the period and fill factor (stripe width) and the nonlinear response decay times will be studied in detail and explained by a simple in-plane surface recombination model. Different etch depths will also be studied, in order to further understand how surface recombination affects the nonlinear response lifetime in one dimensional crystals.

One limitation in the nonlinear response of photonic crystals as presented in the previous chapter is that the carrier decay time is in the tens of picoseconds range. This is, undoubtedly fast, but it is significantly longer than the pulse width, i.e. longer than 130 femtoseconds. In the second half of this chapter, experimental results will be presented showing a response time of less than 400 femtoseconds.

Here, two different ultrafast nonlinear effects, namely the optical Kerr effect and optical (ac) Stark effect, will be shown to be responsible for these subpicosecond nonlinear responses of the photonic crystals.

This chapter is organized as follows: section 5.2 will discuss the experimental set-up modifications necessary to perform the experiments in this chapter. Section 5.3 will discuss the dependence of the nonlinear response decay time of one dimensional photonic crystals on fabrication parameters such as the period, air fill factor and etch depth. An in-plane model will be introduced to simulate the dependence of the nonlinear response decay time on the stripe width, i.e. period and air fill factor.

Section 5.4 will discuss subpicosecond switching of photonic resonances via virtual nonlinearities. Sub-section 5.4.1 will discuss subpicosecond switching of photonic resonances via the optical Kerr effect for infrared pumping, while sub-section 5.4.2 will also discuss subpicosecond switching of photonic resonances, but via a different mechanism, namely the optical (ac) Stark effect, for near infrared pumping.

## **5.2 Experimental Set-Up Modifications**

The experimental set-up used for these measurements is similar to that used in the previous chapter, but several changes were needed to perform the experiments in this chapter. The changes will be now discussed.

The motorized linear translational stage was changed for a different one, with claimed  $0.1 \mu\text{m}$ , i.e. 0.33 femtoseconds, accuracy. The repeatability of this stage

is significantly better than the one used up to this point the only downside is that it is almost ten times slower. This is crucial to ensure accurate determination of the time delay between the pump and the probe, which for step sizes of 33.33 femtoseconds, i.e. 0.005 mm, was not guaranteed by the stage used until now.

The lenses used for focusing and collimating light in the white light continuum generation part of the set-up were substituted for two BK7  $f = 5$  cm aspherical lenses. This was done to have a greater degree of control over the intensity hitting the sapphire plate. The longer focal length results in a larger laser spot on the sapphire, which means that less attenuation is needed and crucially, that the white light continuum should be less sensitive to small changes in the attenuation, thus helping the stability of the white light continuum.

Finally, the last change made was only for the experiments carried out in section 5.5 where the optical (ac) Stark effect is investigated.

This change was necessitated by the highly resonant nature of the optical Stark effect and several initial attempts to measure it ended in failure, due to the fact that the photonic resonances were significantly far away from the exciton,  $\Delta\lambda = \lambda_{\text{resonance}} - \lambda_{\text{exciton}}$  ranged from 30 to 100 nm. Since it was impossible to resolve a photonic resonance closer to the exciton than  $\lambda_{\text{resonance}} = 830$  nm, it was decided to alter the experimental geometry somewhat.

As discussed in chapter three, the output from the Spitfire regenerative amplifier is split 90/10, with 90% of the light going into the TOPAS and the remaining

10% used for generating a white light continuum. This has now been modified as follows:

The beam coming out from TOPAS, formerly used as the pump beam, is now generating the white light continuum. The TOPAS wavelength was selected to be far away from the exciton, i.e.  $\lambda_{\text{TOPAS}} = 700$  nm. Quite serendipitously, it was found that when the white light continuum was generated using the collinear signal beam at  $\lambda_{\text{signal}} = 1400$  nm, it was significantly more stable, albeit much weaker. It was, therefore, decided to use this configuration for the experiments, with an increased number of accumulations, to overcome the weaker signal.

The pump beam is now the remaining 10% of the Spitfire beam, formerly used to generate the white light continuum. The wavelength is set to  $\lambda_{\text{pump}} = 800$  nm.

This arrangement poses one significant problem, and that is the lack of tunability of the pump wavelength. The TOPAS optical parametric oscillator is aligned to work with an input wavelength of 800 nm, and so any major change to this wavelength will require realigning of the TOPAS. It was found, however, that it was possible to tune the Spitfire wavelength by 16 nm, from 792 nm to 808 nm, without any need to realign the TOPAS.

There was a certain degree of concern about the ability of the TOPAS to generate a stable white light continuum. The possible increase in noise due to nonlinear processes by which light at 700 nm is generated by the TOPAS was the major source of concern. These concerns proved to be unfounded as the stability of the white light continuum generated using the TOPAS was significantly better than that from the Spitfire as discussed above.

The useful spectral range available from the white light continuum has now improved, as can be seen in figure 5-1. The long wavelength limit is still set by the response of the CCD detector.

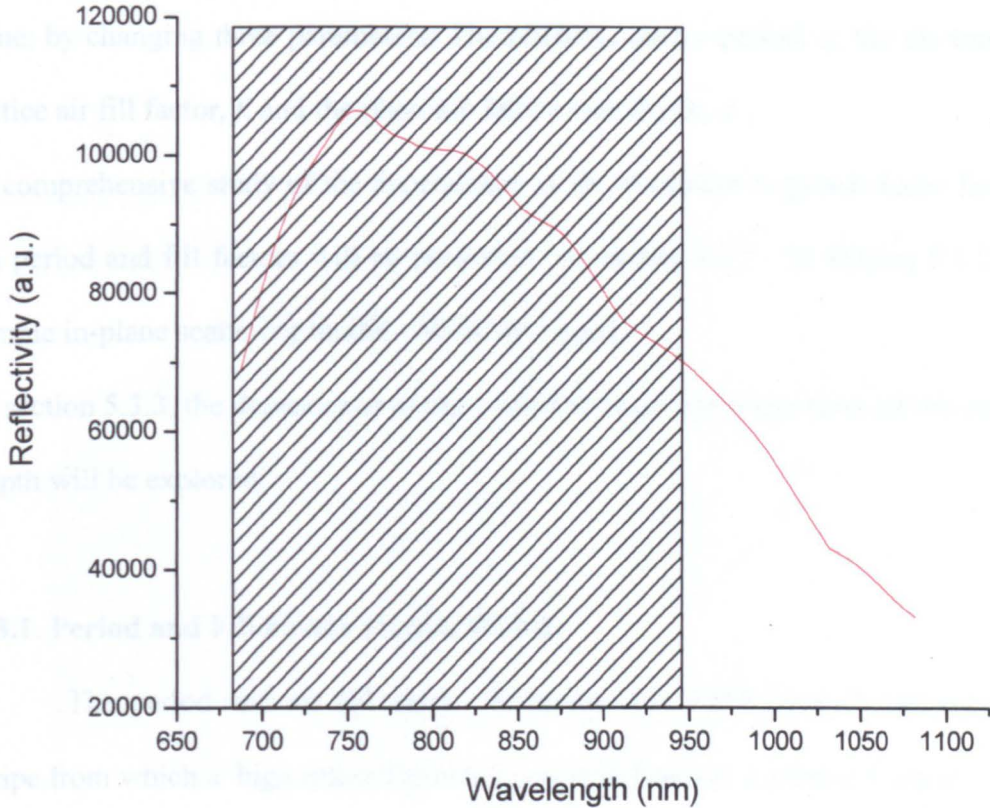


**Figure 5-1** Spectrum of femtosecond white light continuum. Hatched area represents theoretical useful area (for the CCD used).

Finally, the pump and probe angles were exchanged in order to avoid a time consuming setting up process. The pump angle is now  $\theta_{\text{pump}} = 45^\circ$  and the probe angle is  $\theta_{\text{probe}} = 30^\circ$ . Note that for all other experiments performed in this chapter the pump was set to  $30^\circ$  and the probe to  $45^\circ$ . A photograph of this layout can be seen in the previous chapter, figure 4-5.

### 5.3 Nonlinear Response Lifetime Control via Alteration of the Photonic Crystal Waveguide Parameters

In this section it will be shown how the nonlinear response lifetime of one dimensional photonic crystal waveguides can be altered at the fabrication time, by changing three parameters: The photonic lattice period,  $a$ , the photonic lattice air fill factor,  $f$ , and the photonic lattice etch depth,  $d$ .

A comprehensive study of the dependence of the nonlinear response decay time on period and fill factors will be presented on section 5.3.1. In section 5.3.2 a simple in-plane scattering model will be discussed.

In section 5.3.3, the dependence of the nonlinear response decay time on the etch depth will be explored.

#### 5.3.1. Period and Fill Factor (Stripe Width)

The period and air fill factor, determine the width of each individual stripe from which a high refractive index contrast photonic crystal is formed.

The width of each stripe,  $w$ , can be calculated using the following expression:  $w = a \cdot (1 - f)$  where  $a$  is the period and  $f$  is the air fill factor, which is expressed as a fraction not a percentage. An illustration of a typical sample is shown in figure 5-2. The stripe width is marked for clarity.

The range of sample periods available goes from 330 nm to 880 nm, and the air fill factors used are either 20% or 30%. The range of stripe widths goes from 231 nm, for a 330 nm period and 30% air fill factor sample to 704 nm, for a period of 880 nm and 20% air fill factor. A longer stripe width,  $w = 792$  nm, is

available from a sample with a period of 880 nm and 10% air fill factor, but unfortunately no resolvable photonic resonances were found at the wavelengths of interest. The available range of stripe widths will, nonetheless, be sufficient to carry out a systematic study of the dependence of the carrier lifetime on the stripe width.

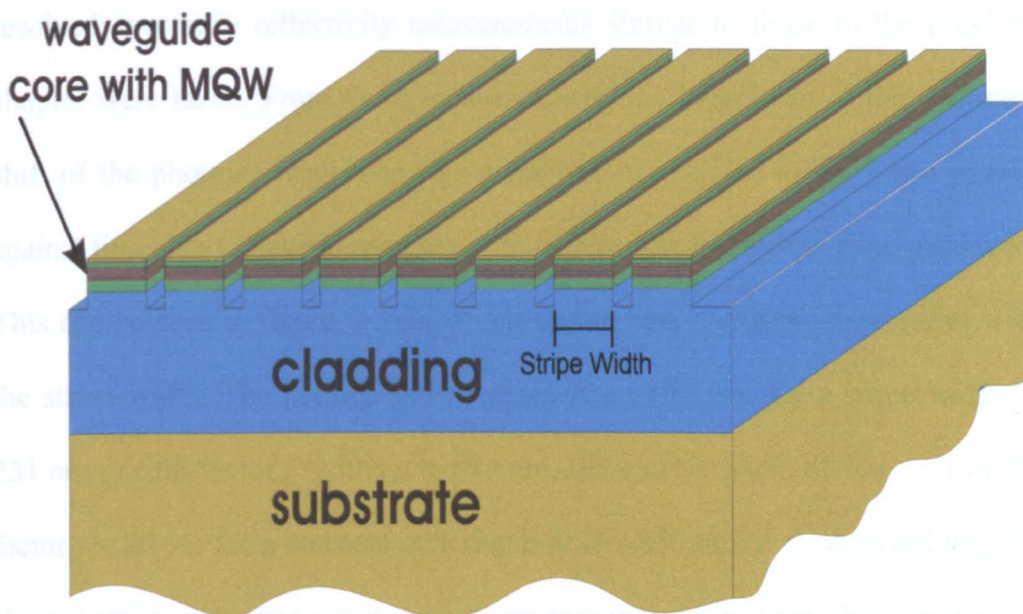


**Figure 5-2** Schematic drawing of a typical one dimensional sample.

As discussed in section 4.4.1, surface recombination is responsible for the significantly reduced carrier relaxation time in photonic crystals. In the previous chapter it was shown that the effect of surface recombination is significantly smaller in one dimensional photonic crystals than it is in two dimensional photonic crystals<sup>3</sup>.

This is due to the fact that in a two dimensional lattice, carriers are always very close to the surface, due to the increased surface area created by etching the lattice. In one dimensional lattices the distances to any surface are, on average longer and therefore nonradiative recombination also plays a significant role in the relaxation of photogenerated carrier relaxation.

In this section the pump wavelength will be kept constant  $\lambda_{\text{pump}} = 810$  nm. Time resolved spectrally reflectivity measurements similar to those in the previous chapter were taken. From these measurements, the magnitude of the nonlinear shift of the photonic resonance was extracted, normalized to unity and plotted against time delay. Several samples with different stripe widths were measured. This can be seen in figure 5-3 a), which shows how the decay time varies with the stripe width. The periods shown range from 330 nm, for a stripe width of 231 nm (air fill factor  $f = 30\%$ ), to 880 nm, for a stripe width of 704 nm (air fill factor  $f = 20\%$ ) for a constant etch depth of  $d = 850$  nm. It is observed that the shorter stripe width has a faster nonlinear response decay time, this variation of the nonlinear response lifetime with stripe width cannot be attributed to a difference in the pump fluence or the pump wavelength. As the nonlinear response lifetime was shown, in the previous chapter, not to depend on the pump wavelength or pump fluence, see figure 4-26

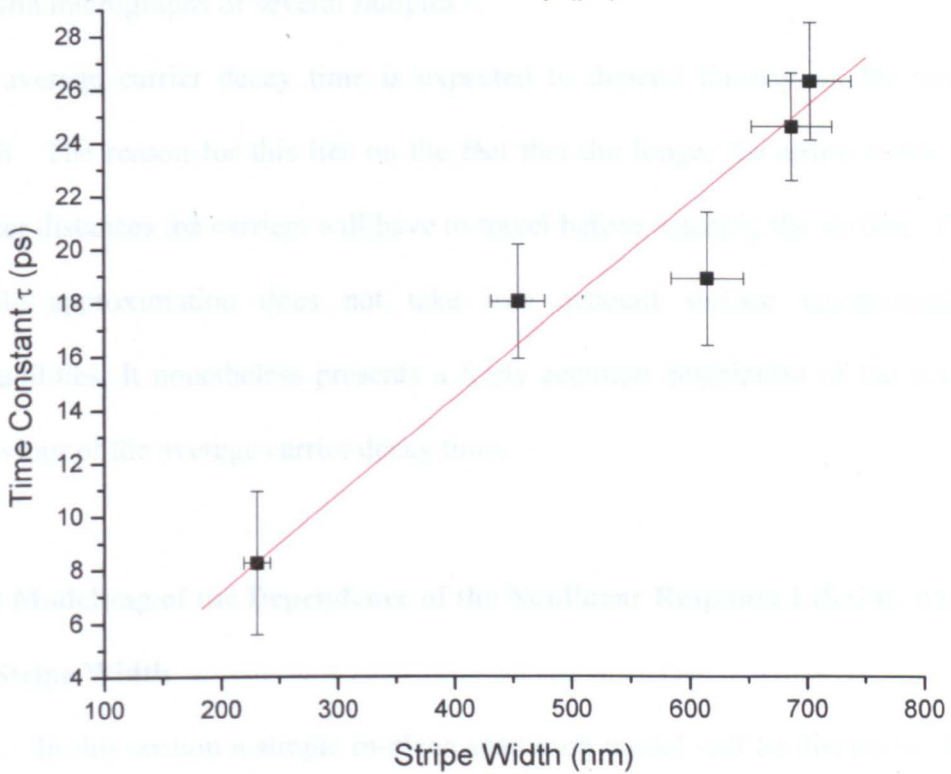
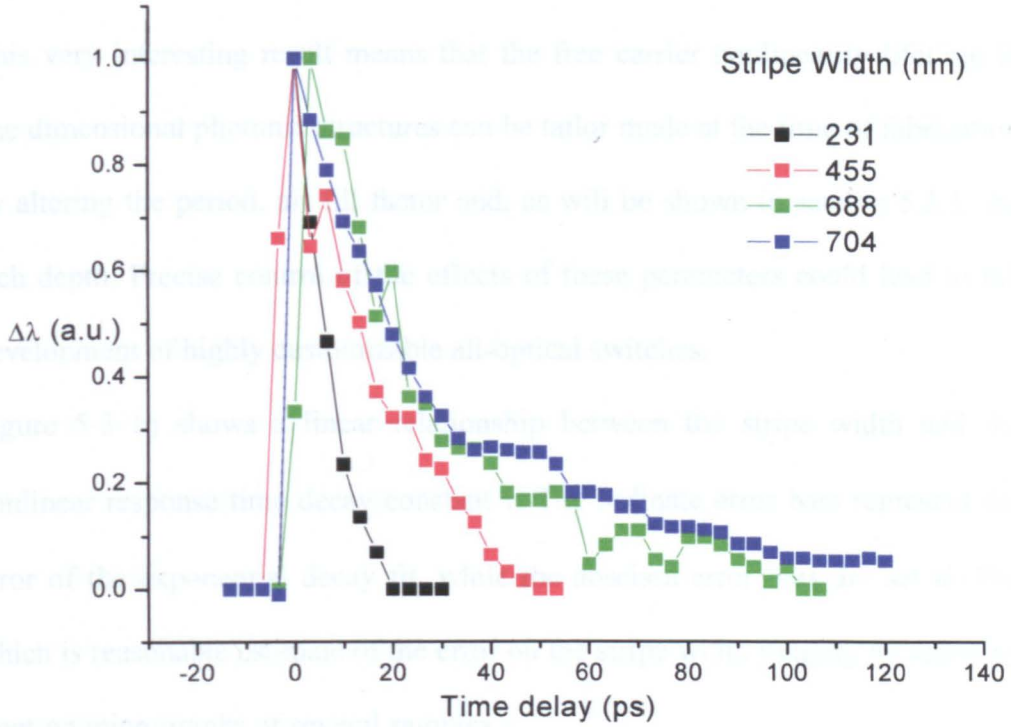


**Figure 5-3 a)** Normalized  $\Delta\lambda$  versus time delay plot for different stripe widths.  $\Delta\lambda$  has been set to unity at zero time delay. Etch depth is fixed at  $d = 850$  nm. **b)** Decay constant versus stripe width plot. The red trace is a linear fit to the data points.

This very interesting result means that the free carrier nonlinearity lifetime in one dimensional photonic structures can be tailor made at the time of fabrication by altering the period, air fill factor and, as will be shown in section 5.3.3, the etch depth. Precise control of the effects of these parameters could lead to the development of highly customizable all-optical switches.

Figure 5-3 b) shows a linear relationship between the stripe width and the nonlinear response time decay constant  $\tau$ . The ordinate error bars represent the error of the exponential decay fit, while the abscissa error bars are set to 5%, which is reasonable estimate of the error on the stripe width judging by scanning electron micrographs of several samples.

The average carrier decay time is expected to depend linearly on the stripe width. The reason for this lies on the fact that the longer the stripe width the greater distances the carriers will have to travel before reaching the surface. This simple approximation does not take into account surface recombination probabilities. It nonetheless presents a fairly accurate description of the actual behaviour of the average carrier decay time.

### **5.3.2 Modelling of the Dependence of the Nonlinear Response Lifetime on the Stripe Width**

In this section a simple in-plane scattering model will be discussed. The main objective of this model is not to provide an accurate prediction of the carrier lifetime, (it is too simple to achieve that), but to achieve the more modest goal of predicting a trend of behaviour.

In order to provide an accurate model of the carrier lifetime in one dimensional crystals or two dimensional crystals, all three dimensions must be considered. This is due to the fact that the deeper the etching the larger the surface area is going to be, and consequently surface recombination will become more prevalent as the etch depth increases. This model however calculates in-plane scattering only. The main reason for developing the model was to try to obtain a simple understanding of the dependence of the nonlinear response lifetime on the stripe width.

The model works by calculating the probability of a carrier reaching the edge of a rectangle of width,  $w = a \cdot (1 - f)$  where  $a$  is the period of the lattice and  $f$  is the air fill factor of the lattice, and height  $80 \mu\text{m}$ , which is the length of the photonic crystal lattice. This rectangle represents one stripe of the one dimensional photonic crystal lattice as shown in orange in figure 5-4.

The model first assumed that the carriers travelled in a straight line with a diffusion speed of  $20000 \text{ m/s}^4$ . As the samples are one dimensional the only source of surface scattering are the edges of the rectangle. This proved to be too simple an assumption that overestimated the amount of surface recombination taking place, as the calculated distance travelled by the carriers was longer than the real distance, which lead to an overestimation of the amount of surface recombination. Therefore, in order to simulate the carrier trajectory more accurately, the straight line distance travelled by the carrier is multiplied by a random number with value between 0 and 1.

This is a more accurate estimation of the actual distance travelled by the carrier and more importantly of the carrier final position. This random number is calculated for each instance, in order to ensure, a truly random process. The effect of this random number can be seen in figure 5-4, where the blue arrows represent the calculated trajectories of the carriers. Note how the distances travelled for each angle are different.

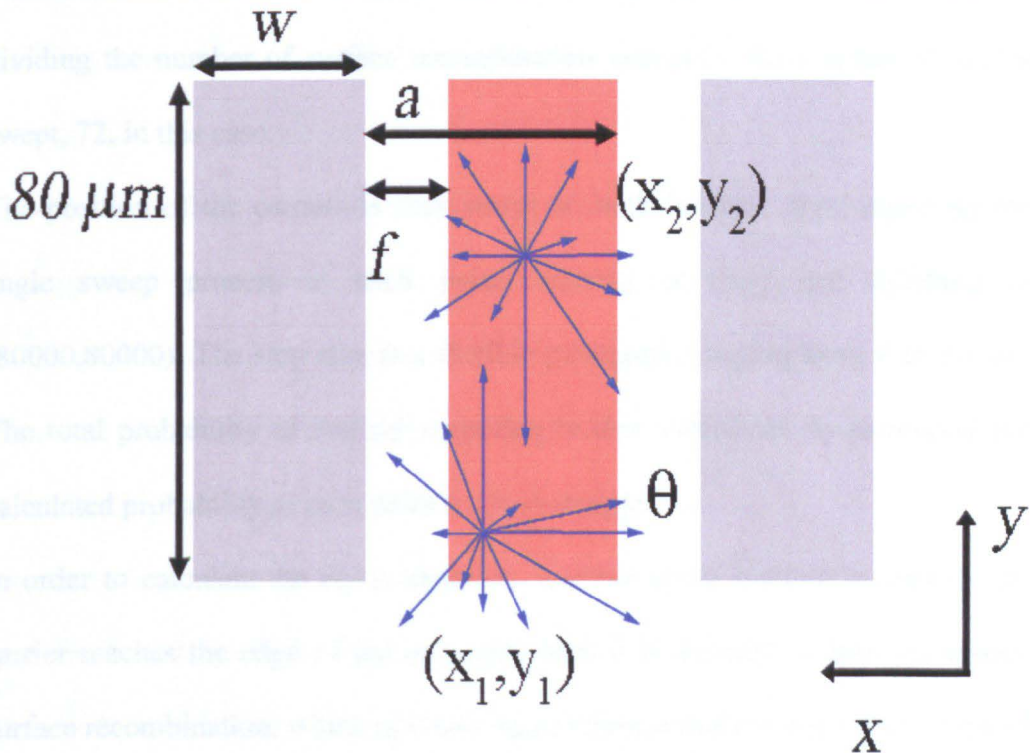


**Figure 5-4** Schematic view of a typical high refractive index contrast one dimensional photonic crystal. The orange stripe is the rectangle used in the in-plane model.  $w$  is the stripe width,  $a$  is the period and  $f$  is the air fill factor. The modelled carrier trajectories are shown by blue arrows. Positions  $x_1, y_1$  and  $x_2, y_2$  show carrier trajectories at different positions and for different sweep angles (not all angles are shown for clarity).

At each position in the stripe, the probability of the carrier reaching an edge of the rectangle, i.e. the surface of the stripe, is calculated by performing an angular sweep of all possible trajectories. In essence the model calculates the distance travelled by the carrier along each angle, the angle step size was set to 5 degrees, and then the probability of a carrier moving from that position reaching the edge of the rectangle, is calculated by looking at the final carrier position for each angle. If the final carrier position is outside the rectangle then surface recombination is deemed to have taken place. The probability is calculated by dividing the number of surface recombination events by the number of angles swept, 72, in this case.

The position of the carriers is then swept on both in-plane axes, repeating the angle sweep process at each point, starting at (0,0) and finishing at (80000,80000). The step size is a flexible parameter, ranging from 4 to 10 nm. The total probability of surface scattering is then calculated by averaging the calculated probability at each point in the rectangle.

In order to calculate the decay constant, a rather crude method is used. If the carrier reaches the edge of the rectangle, then it is deemed to have undergone surface recombination, which in GaAs based semiconductors has a decay time of several picoseconds. If the carrier does not reach the edge of the rectangle then nonradiative recombination is deemed to have occurred with a decay time, in AlGaAs, of approximately 100 picoseconds<sup>2</sup>.

The diffusion time is calculated for carriers undergoing surface recombination and added to the surface recombination decay time. The average lifetime for

carriers at each point is then calculated from the surface recombination plus diffusion time for carriers undergoing surface recombination and from the literature value of nonradiative recombination in AlGaAs. The final value of the decay constant is obtained by averaging over all positions.

As described in the introduction, this model only calculates in-plane scattering. A numerical factor,  $z$ , was introduced in a crude attempt to model the different etch depths. This numerical factor ranges between 0 and 1 and modulates the nonradiative recombination time. A factor of 1 equates to an unpatterned crystal, while an infinitely deep patterned structure would have a value of zero. A value of  $z = 0.31$  was found to give reasonable estimates for an etch depth of  $d = 850$  nm as used in the samples in the previous section.

This method artificially reduces the nonradiative recombination time. This, in essence means that more weight is given to surface recombination processes as the etching becomes deeper. This approach will be vindicated by the data shown in section 5.3.3.

At any rate, the principal objective of the model is not to obtain an accurate prediction of the carrier lifetime (the model is too simple to do that as has been discussed above) but its principal objective is to predict patterns of behaviour, i.e. how does the carrier lifetime change with increasing or decreasing the stripe width. The model achieves this more modest goal with ease.

As discussed above a linear dependence of the decay time on the stripe width is observed. The model correctly predicts such a linear dependence as shown in figure 5-5. The modelled data shows a similar linear dependence between the

stripe width and the decay constant to that shown by the experimental data in figure 5-3 b).

There is a reasonable agreement between the calculated and measured decay constant values, despite the rather simplistic nature of the model.

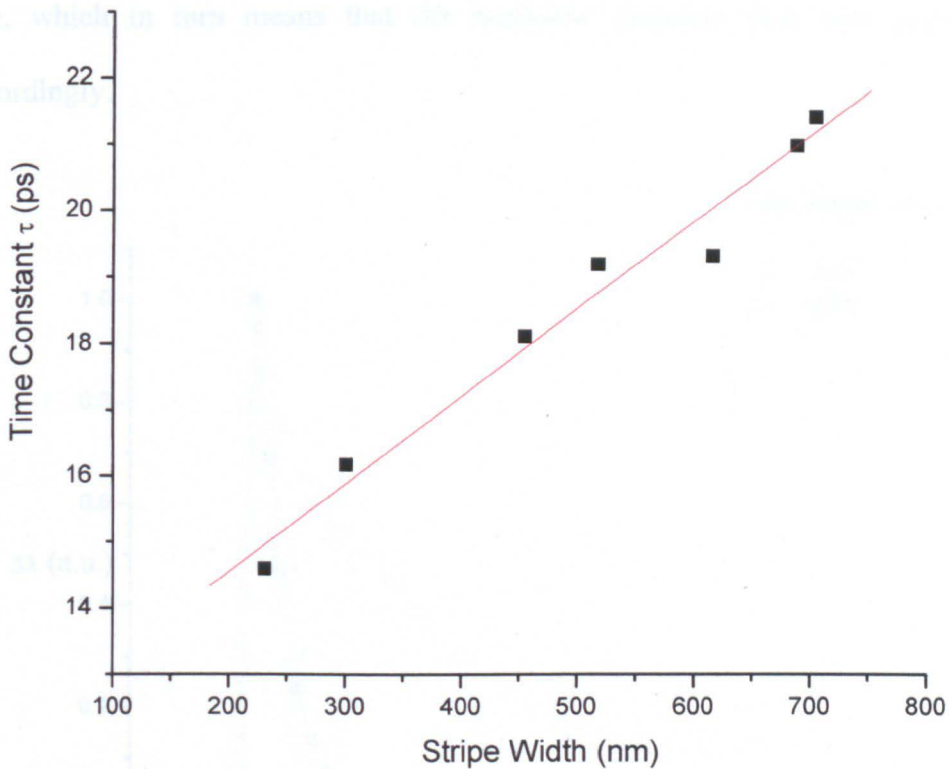


**Figure 5-5** Decay constant versus stripe width plot. The red trace is a linear fit to the modelled data points.

### 5.3.3 Etch Depth

In the previous sections the etch depth has been kept constant at  $d = 850$  nm, as has been the case so far in this thesis. In this section, samples with different etch depths will be measured, namely 100 and 200 nm and

compared with 850 nm etch depth. It will be shown how the etch depth also affects the nonlinear response lifetime of one dimensional photonic crystals.

This is due to the changes in surface area associated with changes in the etch depth. As the etch depth increases, so does the surface area, and it is thus expected that surface recombination will play an ever increasingly important role, which in turn means that the nonlinear response time will decrease accordingly.

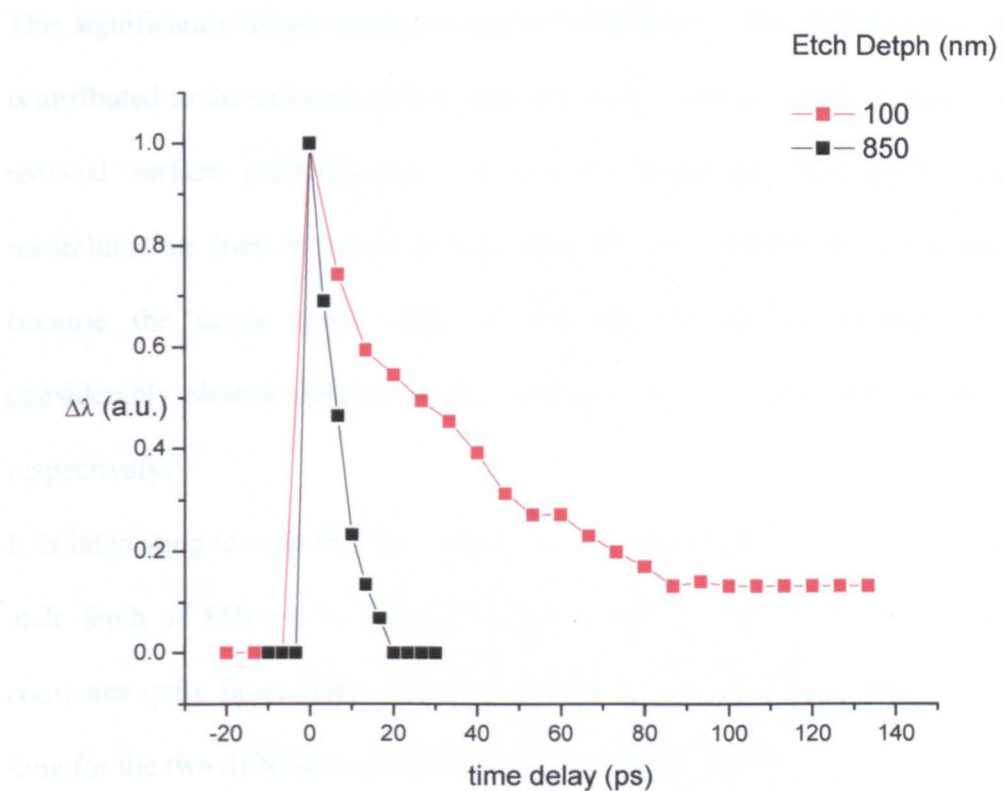


**Figure 5-6** Normalized  $\Delta\lambda$  versus time delay plot for different etch depths.  $\Delta\lambda$  has been set to unity at zero time delay. Period is  $a = 330$  nm, air fill factor  $f = 30\%$  stripe width is  $w = 231$  nm. Fluence  $F = 0.56$  mJ/cm<sup>2</sup>.

It is thus expected that samples with shallower etch depths, i.e. 100 and 200 nm, will show longer nonlinear response than those measured before, i.e.

$d = 850$  nm. This is clearly illustrated in figure 5-6, which compares normalized  $\Delta\lambda$  versus time delay for two samples with the same period and air fill factor,  $a = 330$  nm,  $f = 30\%$ , giving a stripe width of  $w = 231$  nm, but two different etch depths, namely 100 and 850 nm.

The change in the nonlinear response lifetime for the different etch depth is remarkable. For an etch depth of 850 nm, the decay constant is  $\tau = 8.5 \pm 2.5$  ps, whereas for an etch depth of 100 nm, the decay constant is  $\tau = 33.5 \pm 2.6$  ps. This significantly longer nonlinear response lifetime for the shallower etch depth is attributed to the reduced surface area due to the etching, which in turns means reduced surface recombination. Despite the shallower etch depth, surface recombination does still play an important role as a carrier decay mechanism because the decay time, while longer than for deeper etching, is still considerably shorter than for bulk AlGaAs, i.e. 33 versus 100 picoseconds respectively.

It is interesting to note that the reduction in total surface area on going from an etch depth of 850 nm to 100 nm is approximately 4.5 times. This reduction compares quite favourably with the reduction of the nonlinear response decay time for the two different etch depths, which is approximately 4 times.

A further comparison of the dependence of the nonlinear response on etch depth is presented in figure 5-7. The sample has the same period as in figure 5-6, i.e.  $a = 330$  nm, but the air fill factor is now  $f = 20\%$ . The etch depths are 100 and 200 nm. The small contrast in etch depth results in a much smaller difference in the nonlinear response lifetime when compared with figure 5-6.

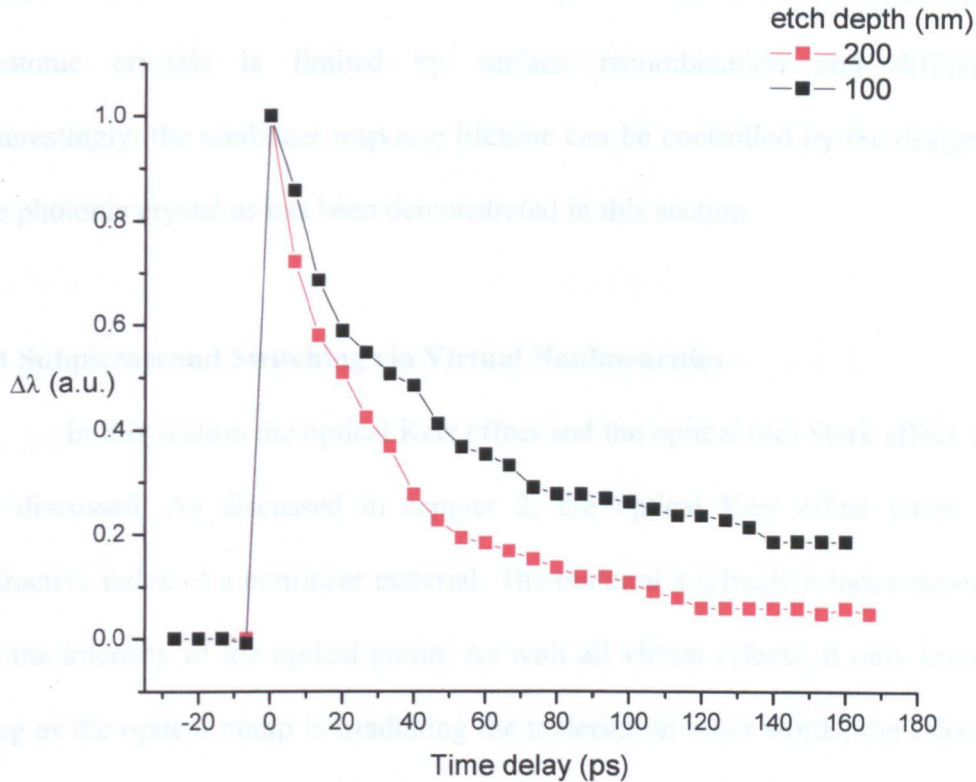


**Figure 5-7** Normalized  $\Delta\lambda$  versus time delay plot for different etch depths.  $\Delta\lambda$  has been set to unity at zero time delay. Period is  $a = 330$  nm, air fill factor  $f = 20\%$  stripe width is  $w = 264$  nm. Fluence  $F = 0.56$  mJ/cm<sup>2</sup>

For an etch depth of 100 nm, the decay constant is  $\tau = 35.6 \pm 2.4$  ps, whereas for an etch depth of 200 nm the decay constant is  $\tau = 29 \pm 2.2$  ps.

The reduction of surface area is just 1.4 times this time, which again compares quite favourably with a reduction in the nonlinear response decay time of 1.2 times.

As expected the nonlinear response lifetime becomes shorter for deeper etching. The difference in the nonlinear response lifetime between both etch depths is small due to the small difference in etch depth.

These results confirm that the nonlinear response lifetime of one dimensional photonic crystals is limited by surface recombination and diffusion. Interestingly, the nonlinear response lifetime can be controlled by the design of the photonic crystal as has been demonstrated in this section.

#### **5.4 Subpicosecond Switching via Virtual Nonlinearities**

In this section the optical Kerr effect and the optical (ac) Stark effect will be discussed. As discussed in chapter 2, the optical Kerr effect alters the refractive index of a nonlinear material. The material's refractive index depends on the intensity of the optical pump. As with all virtual effects, it only lasts as long as the optical pump is irradiating the material, in other words, the effect is only present for a time comparable to the pump pulse width. This effect has been reported in Bragg mirrors<sup>5</sup> and in silicon based two dimensional photonic crystals<sup>6</sup>, but has not been reported in III-V based high refractive index contrast photonic crystals.

The other virtual effect that will be discussed is the optical (ac) Stark effect. In this effect the exciton energy is renormalized by the optical pump. This changes the refractive index, which in turn changes the band structure of the photonic crystal. The optical Stark effect has been observed in Bragg mirrors<sup>7</sup> and in organic based photonic crystals<sup>8</sup>, but again it has not been observed in III-V based high refractive index contrast photonic crystals.

### 5.4.1. Subpicosecond Switching via the Nonlinear Kerr Effect

In this section subpicosecond switching of photonic resonances via the optical Kerr effect will be discussed. In a Kerr medium the refractive index of a material becomes:

$$n(I) = n_0 + n_2 I \quad (5.1)$$

where  $n_0$  is the linear refractive index and the nonlinear refractive index  $n_2$  takes the form (for isotropic media):

$$n_2 = \frac{1}{n_0^2 c \epsilon_0} \chi^{(3)} \quad (5.2)$$

where  $\chi^{(3)}$  is the electric susceptibility.

In a Kerr medium, the refractive index depends on the intensity of the pump beam. The implications of this effect for photonic crystals are very interesting. It has been shown in the previous chapter that nonlinear changes in the refractive index lead to nonlinear shifts of the photonic resonances. So far in this thesis, these nonlinear shifts in the photonic resonances have been caused by the photogeneration of free carriers, which had decay times around of 10-30 picoseconds. The nonlinear Kerr effect is a virtual effect, and as such, no real carriers are created. One main consequence of this is that the effect will only last for as long as the pump is on and it is, therefore, expected that this effect will last for several hundred femtoseconds, which is approximately two orders of magnitude faster than with real carriers.

As discussed in the previous chapter, several attempts to see subpicosecond nonlinear shifts of a photonic resonance at near infrared pump wavelengths,

either via the optical (ac) Stark effect, or the nonlinear Kerr effect, failed initially, mainly due to the presence of real carriers that shifted the photonic resonance by a greater amount than a virtual effect would, making it impossible to see any evidence of an subpicosecond nonlinear shift.

In this section the pump wavelength ranges from 2050 to 2135 nm. This range of wavelengths fall very close to the maximum in the three photon absorption coefficient as can be seen in figure 5-8. Unfortunately the range of wavelengths was limited by a poor choice of filtering optics used to separate the signal from the idler beam of the TOPAS output.

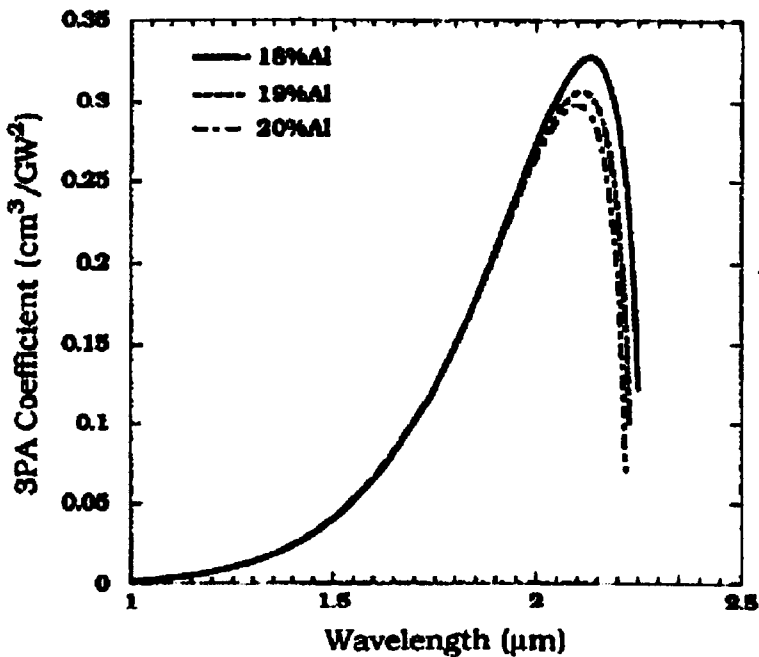


**Figure 5-8** Three photon absorption coefficient versus wavelength plot. The graph is reproduced from reference 9.

This is unfortunate as it means that there will still be photogenerated free carriers, as shown in section 4.4.2., which was the main reason for using a pump

wavelength in the infrared. Fortunately, it was possible to observe a subpicosecond shift of the photonic resonance. This nonlinear shift was however superimposed on the nonlinear shift due to photogenerated carriers created via three photon absorption.

Figure 5-9 shows a typical time resolved differential reflectivity spectra set for a sample with the following parameters: Period  $a = 860$  nm, air fill factor  $f = 20\%$  and etch depth  $d = 850$  nm from the high exposure set. The pump wavelength is set to  $\lambda_{\text{pump}} = 2135$  nm and the average pump power is  $250 \mu\text{W}$ , which equates to a fluence  $F = 1.8 \text{ mJ/cm}^2$  or an intensity  $I = 13.2 \text{ GW/cm}^2$ . The time step is  $0.005$  ns or  $33.33$  femtoseconds.

A remarkable feature of the data presented in figure 5-9 is how the photonic resonance located at  $865$  nm rises and decays on a femtosecond timescale. This is appreciated better by looking at the maximum value of the differential reflectivity for every spectra (i.e. the value of the differential reflectivity at the original (unshifted) position of the photonic resonance (i.e.  $866$  nm)) versus time delay as shown in figure 5-10.

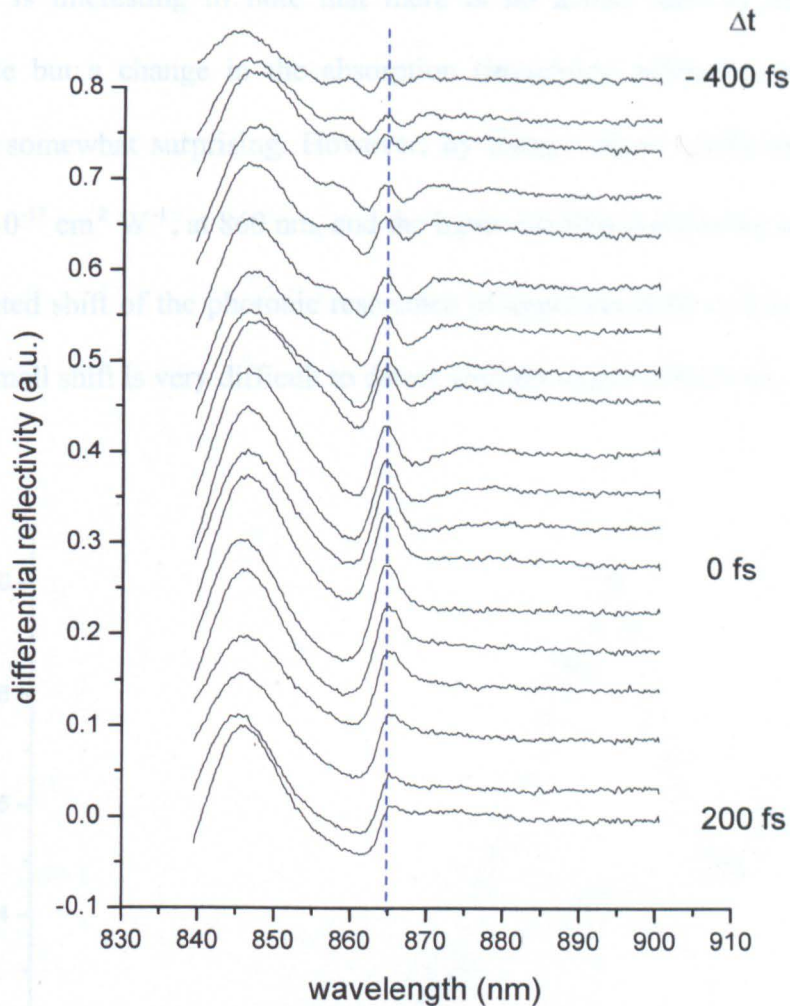


**Figure 5-9** Time resolved differential reflectivity spectra showing subpicosecond switching of a photonic resonance via the optical Kerr effect. The sample is from the high exposure set and the parameters are as follows: Period  $a = 860$  nm, fill factor  $f = 20\%$  and etch depth  $d = 850$  nm. Blue dashed line indicates position of photonic resonance. The pump wavelength is  $\lambda_{\text{pump}} = 2135$  nm and the fluence is  $F = 1.8$  mJ/cm<sup>2</sup>.

The photonic resonance does not fully decay to its original state due to the onset of three photon absorption which generates a significant change in the refractive index and consequently a shift in the photonic resonance as discussed in section

4.5.3. It is interesting to note that there is no actual shift of the photonic resonance but a change in the absorption (imaginary refractive index). This result is somewhat surprising. However, by using a Kerr coefficient value of  $n_2 = 4 \cdot 10^{-13} \text{ cm}^2 \text{ W}^{-1}$ , at 860 nm, and the input intensity used in the experiments a calculated shift of the photonic resonance of approximately -0.3 nm is found. Such a small shift is very difficult to detect with the experimental set-up used.

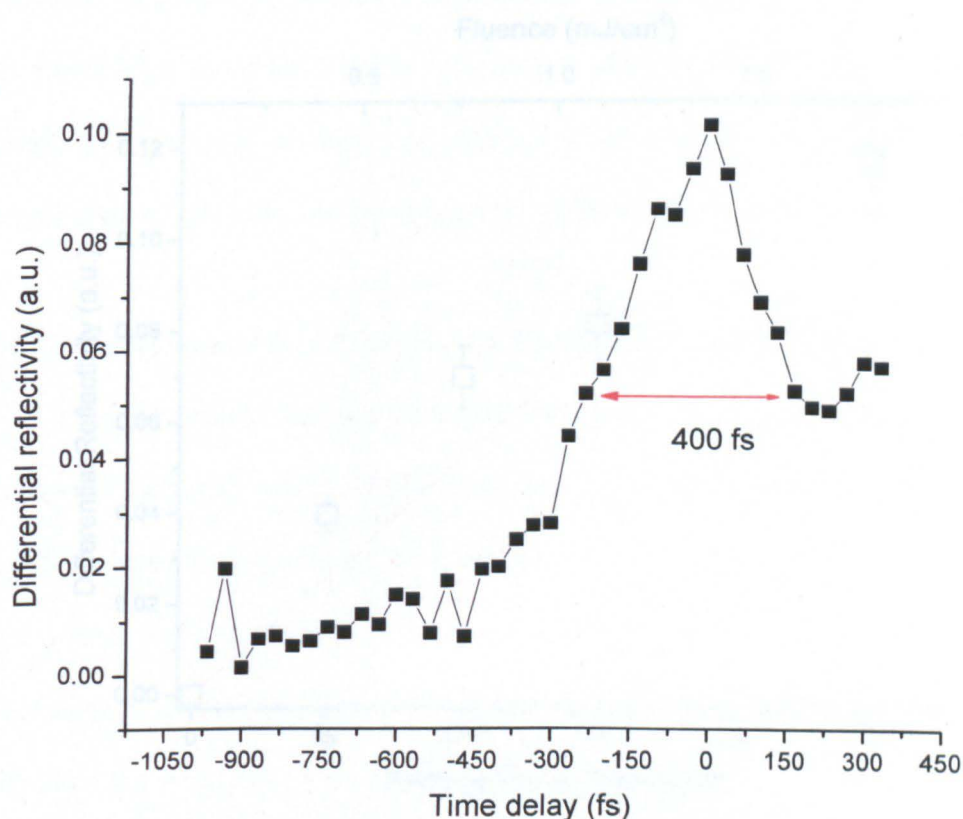


**Figure 5-10** Differential reflectivity at 865 nm versus time delay (extracted from figure 5-9, showing subpicosecond switching of a photonic resonance via the optical Kerr effect. The sample is from the high exposure set and the parameters are as follows: Period  $a = 860 \text{ nm}$ , fill factor  $f = 20 \%$  and etch depth  $d = 850 \text{ nm}$ . The pump wavelength is  $\lambda_{\text{pump}} = 2135 \text{ nm}$  and the fluence is  $F = 1.8 \text{ mJ/cm}^2$ .

Nevertheless figure 5-10 clearly shows subpicosecond switching of a photonic resonance due to the nonlinear Kerr effect. As discussed before; the subpicosecond switching of the resonance is superimposed on a rising background due to real carriers generated by three photon absorption that create a nonlinear shift of the photonic resonance on a much longer (tens of picoseconds) time scale.

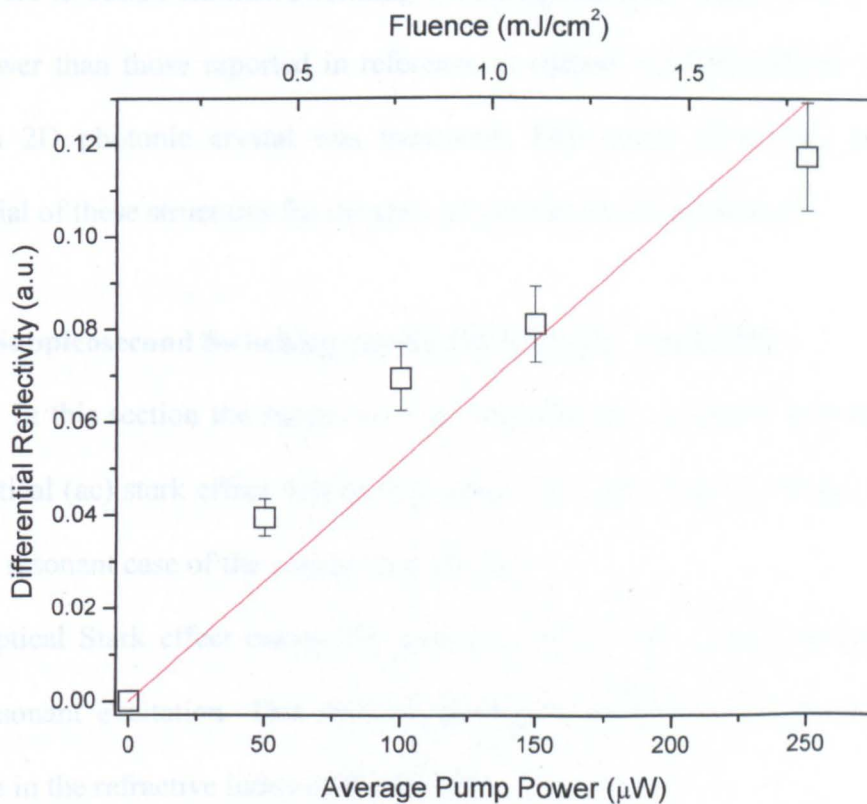


**Figure 5-11** Nonlinear optical Kerr effect dependence of the differential reflectivity on the pump power. The data points are marked by open squares and are extracted from figure 5-9. The red trace is a linear fit to the data points.

A power dependent measurement was carried out on the same sample used in this section so far. This is shown in figure 5-11. The data shows an approximate

linear dependence of the optical Kerr effect with input pump power. This linear relationship between the input power and the change in the refractive index stems directly from equation 5.1

In this section it has been shown, for the first time in III-V based high refractive index photonic crystals, that it is possible to instantaneously switch a photonic resonance using the optical Kerr effect. It is worth noting that the intensities used here to obtain ultrafast switching via the optical Kerr effect, 2-13 GW/cm<sup>2</sup>, are lower than those reported in reference 6, namely 20-100 GW/cm<sup>2</sup> where a silicon 2D photonic crystal was measured. This result shows the excellent potential of these structures for ultrafast all-optical switching devices.

#### 5.4.2 Subpicosecond Switching via the Optical (AC) Stark effect

In this section the subpicosecond switching of a photonic resonance via the optical (ac) stark effect will be discussed. This effect can be thought of as a highly resonant case of the optical Kerr effect.

The optical Stark effect causes the atomic levels to shift when submitted to a non-resonant excitation. This shift of the atomic levels can be interpreted as change in the refractive index of the structure<sup>10</sup>.

The change in refractive index due to the optical Stark is, thus proportional to the change in the atomic levels:

$$\Delta n^{Stark}(t) \propto -\frac{|\mu \cdot E_p|^2}{\omega_p - \omega_{EX}} \quad (5.3)$$

where  $\mu$  is the exciton oscillator strength,  $E_p$  is the electric field,  $\omega_p$  is the frequency of the light field and  $\omega_{EX}$  is the frequency of the exciton.

Equation 5.3 illustrates the three key parameters in the optical Stark effect, namely: the exciton oscillator strength, pump intensity and pump frequency detuning with respect to the exciton.

In previous observations of the optical Stark effect, a high number of multiple quantum wells have been used ( $>10$ )<sup>11,7</sup>. By contrast the samples used here only have five quantum wells, which makes obtaining a sizeable effect somewhat harder as the quantum wells are a smaller fraction of the waveguide core. Alternatively, a very high exciton oscillator strength material has been used<sup>8,12</sup> in order to obtain a sizeable effect.

The use of cryogenic temperatures leads to sharper exciton signatures and consequently it has also been used in previous experiments<sup>11,7</sup>. Unfortunately, the present experiments are more difficult to perform using a cryostat, which, together with the limited tunability of the experimental set-up precludes any meaningful use of cryogenic temperatures here.

The pump frequency detuning is critical. Resonant pumping will result in photo generation of real carriers and consequently no Stark shift will be observed. Almost negligible Stark shifts were found for pump wavelengths less than 10 nm away from the exciton wavelength.

A typical set of time resolved differential reflectivity spectra showing subpicosecond switching of a photonic resonance caused by the optical Stark effect is shown in figure 5-12.

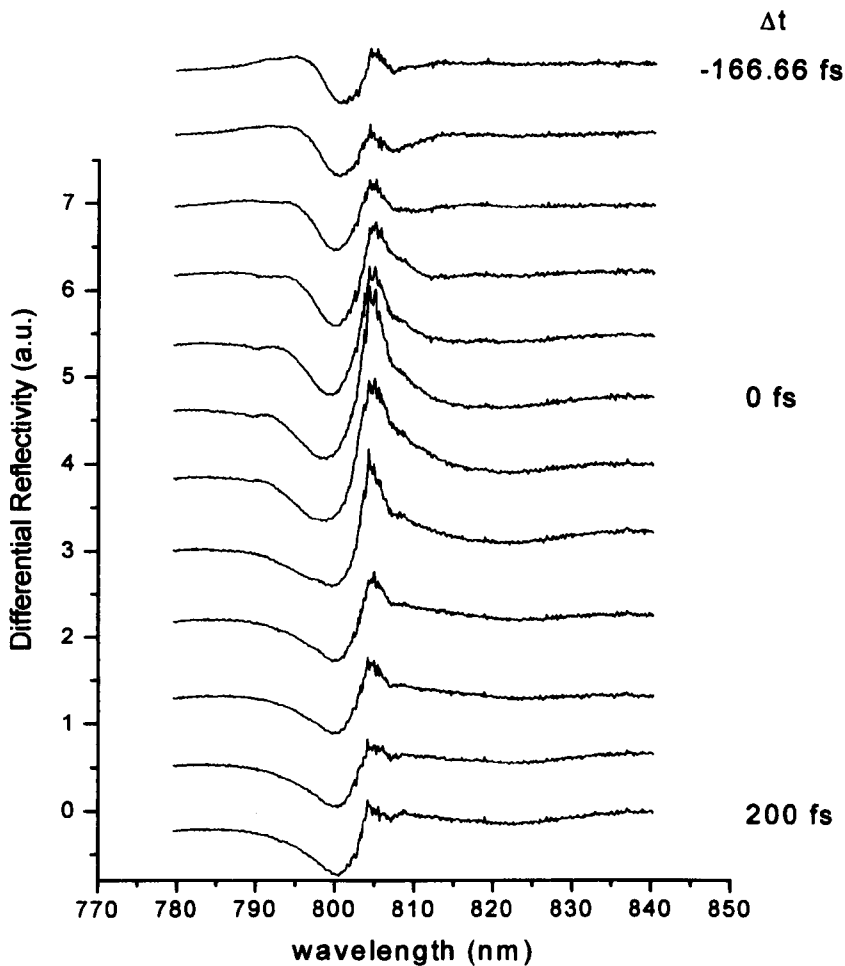


**Figure 5-12** Time resolved differential reflectivity spectra showing subpicosecond switching of a photonic resonance via the optical (ac) Stark effect. The sample is from the low exposure set and the parameters are as follows: Period  $a = 860$  nm, fill factor  $f = 30\%$  and etch depth  $d = 850$  nm. Pump wavelength is  $\lambda_{\text{pump}} = 800$  nm. Fluence is  $F = 0.71$  mJ/cm<sup>2</sup>.

The sample parameters are as follows: Period  $a = 860$  nm, fill factor  $f = 30$  % and etch depth  $d = 850$  nm from the low exposure set. The pump wavelength is set to  $\lambda_p = 800$  nm. This means that there is a detuning between the pump wavelength and the exciton of 1 nm. The average pump power is  $100 \mu\text{W}$ , which equates to a fluence  $F = 0.71 \text{ mJ/cm}^2$  or an intensity  $I = 5.52 \text{ GW/cm}^2$ . The temporal step size is  $0.005 \text{ ns}$  or  $33.33$  femtoseconds.

Figure 5-12 clearly shows an ultrafast change in the photonic resonance located approximately at  $805$  nm. This change is due to the optical Stark effect which alters the refractive index, which ultimately causes the photonic resonance to blue shift. The signature of the shift is clear with no associated bleaching as with real carriers as shown in the previous chapter. As predicted by the virtual nature of the optical Stark effect, the photonic resonance has completely recovered after less than  $350$  femtoseconds. Exciton ionization<sup>13</sup> cannot be responsible for this ultrafast blueshift as the photonic resonance completely recovers to its original position. This is easier to see in figure 5-13 below, in which the maximum value of the differential reflectivity for every spectra, i.e. the original (unshifted) position of the photonic resonance, versus time delay is plotted.

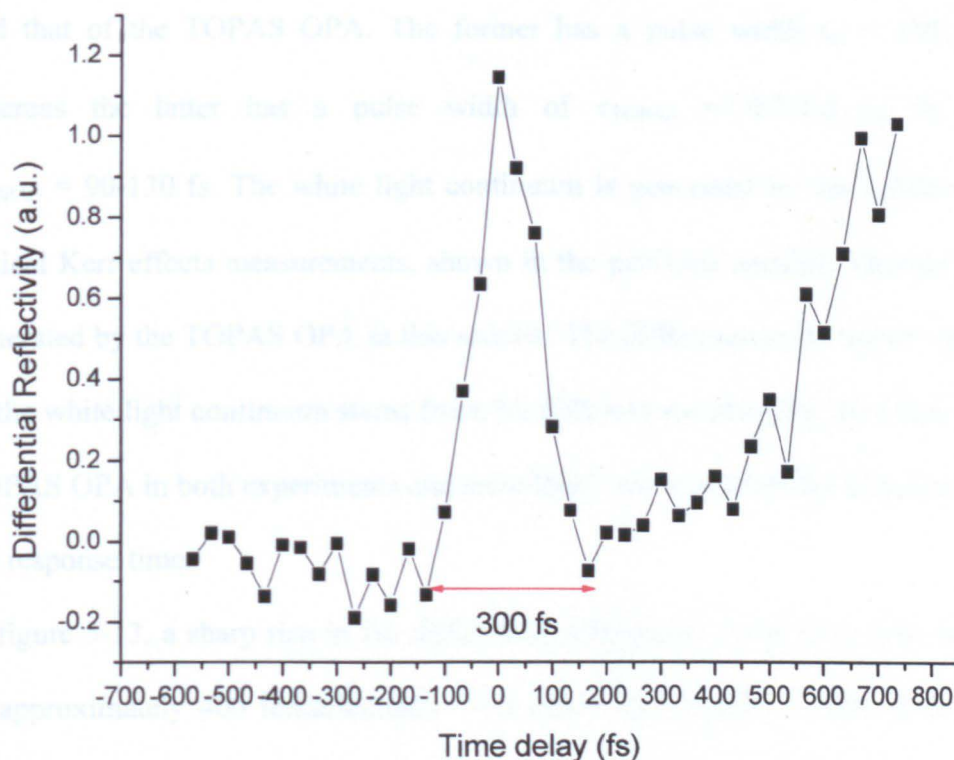


**Figure 5-13** Differential reflectivity at 805 nm versus time delay plot showing subpicosecond switching of a photonic resonance via the optical (ac) Stark effect, extracted from figure 5-12. The sample is from the high exposure set and the parameters are as follows: Period  $a = 860$  nm, air fill factor  $f = 30\%$  and etch depth  $d = 850$  nm. Pump wavelength is  $\lambda_{\text{pump}} = 800$  nm. Fluence is  $F = 0.71$  mJ/cm<sup>2</sup>.

It is clear from figure 5-13, that the change in the photonic resonance and ultimately, in the refractive index, only last for approximately 300 femtoseconds. This is approximately twice the pulse width of the laser system.

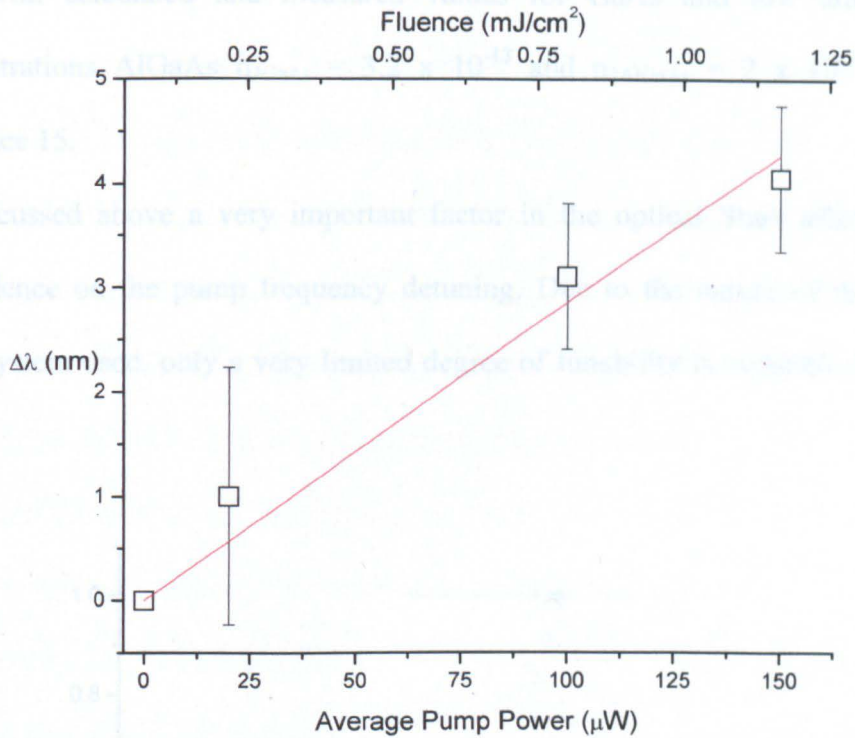
The difference between the time responses in figure 5-13, which shows the optical Stark effect mediated change in the refractive index, and figure 5-10, which shows the optical Kerr effect mediated change in the refractive index stems from the difference in pulse width of the Spitfire regenerative amplifier

and that of the TOPAS OPA. The former has a pulse width  $\tau_p = 130 \text{ fs}^{14}$ , whereas the latter has a pulse width of  $\tau_{\text{TOPAS}} = 0.7-1.0 \tau_p \text{ fs}$ , i.e.  $\tau_{\text{TOPAS}} = 90-130 \text{ fs}$ . The white light continuum is generated by the Spitfire for optical Kerr effects measurements, shown in the previous section, whereas it is generated by the TOPAS OPA in this section. The difference in the pulse widths of the white light continuum stems from the different wavelengths used from the TOPAS OPA in both experiments and most likely account from the difference in the response time.

In figure 5-13, a sharp rise in the differential reflectivity occurs at a time delay of approximately 400 femtoseconds. This rise is attributed to a change in the refractive index caused by real carriers. Two photon absorption is responsible for photogeneration of these carriers.

The power dependent response of the optical Stark effect is expected to be similar to that of the optical Kerr effect, i.e. linear with pump intensity or quadratic with the field, as described by equation 5.3.

In order to test the expected linear dependence with power, a power dependent measurement was carried out on the same sample used in this section so far. This is shown in figure 5-14.



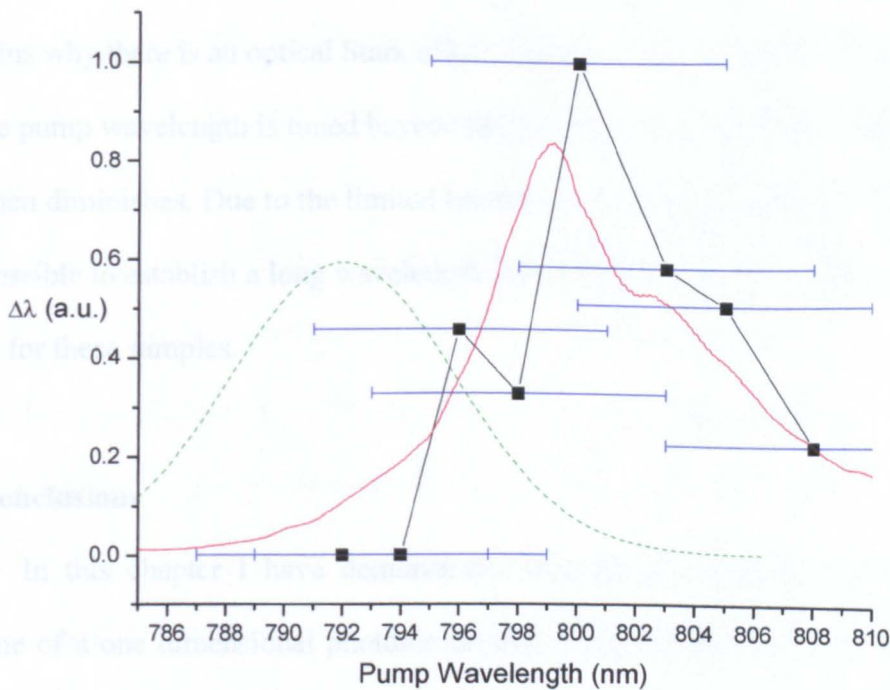
**Figure 5-14** Optical (ac) Stark effect power dependence plot.  $\Delta\lambda$  versus pump power is plotted. The data points are marked by open squares. The red trace is a linear fit to the data points.

Figure 5-14 shows the result of power dependent measurements. The red trace is a reasonable fit to the data points. Figure 5-14 shows that there is a linear dependence of the induced change in refractive index caused by the optical Stark effect on the input power as expected from equation 5.3.

An estimate for the value of  $n_2$  can be extracted from figure 5-14 using equation 2.28, to calculate the change in the refractive index associated with the nonlinear shift of the photonic resonance caused by the optical Stark effect, and equation 5.1. A value for  $n_2 = 5.2 \pm 4.1 \times 10^{-12}$  is found. This value compares reasonably

well with calculated and measured values for GaAs and low aluminium concentrations AlGaAs  $n_{2\text{GaAs}} = 3.2 \times 10^{-13}$  and  $n_{2\text{AlGaAs}} = 2 \times 10^{-13}$  see reference 15.

As discussed above a very important factor in the optical Stark effect is its dependence on the pump frequency detuning. Due to the nature of the laser-OPA system used, only a very limited degree of tunability is available, namely 16 nm.



**Figure 5-15** Photonic resonance nonlinear shift (normalized) versus pump wavelength. The red trace is a PL spectrum of the sample, showing the position of the exciton to be at 799 nm. The green dotted trace represents a typical laser pulse centred at 792 nm. The fluence is  $F = 1.25 \text{ mJ/cm}^2$ . The blue error bars represent the pulse bandwidth at each pump wavelength.

Figure 5-15 shows a plot of the nonlinear shift of the photonic resonance versus pump wavelength detuning. The same sample as for the previous measurement is used. The average power was increased to  $175 \mu\text{W}$ , this gives a fluence  $F = 1.25 \text{ mJ/cm}^2$  or an intensity  $I = 9.67 \text{ GW/cm}^2$ . It is interesting to note the lack of nonlinear shift for wavelengths shorter than 794 nm shown in figure 5-15. This is due to most of the pump pulse being resonant with the exciton and thus generating real carriers. At longer pump wavelengths, 796, 798 nm, a significant amount of the pump pulse is non-resonant with the exciton which explains why there is an optical Stark effect induced shift at these wavelengths. As the pump wavelength is tuned beyond the exciton wavelength, the shift peaks and then diminishes. Due to the limited tunability of the experimental set-up it is not possible to establish a long wavelength limit of detection of the optical Stark effect for these samples.

## 5.5 Conclusions

In this chapter I have demonstrated that the free carrier nonlinearity lifetime of a one dimensional photonic crystal waveguide depends on its stripe width, which is determined by its period and air fill factor, and on its etch depth. By keeping the etch depth constant at 850 nm, the nonlinear response decay constant,  $\tau$ , was found to range with stripe width from 8.5 ps for a stripe width of 231 nm (i.e. sample period of 330 nm and air fill factor of 30 %) to 26.4 ps for a stripe width of 704 nm (i.e. sample period of 880 nm and air fill factor of 20 %).

The stripe width affects the amount of surface recombination taking place. Longer stripe widths result in less surface recombination, as carriers have to travel, on average, longer distances to any surface, and therefore the nonlinear response lifetime will be shorter, as more non-radiative recombination takes place. A simple model verified this trend, and confirms previous assumptions by Bristow *et al* about the role of surface recombination as a relaxation mechanism for excited carriers.

By using the same sample (i.e. period  $a = 330$  nm, air fill factor  $f = 30\%$ ) etched down to different depths, the decay constant was found to increase significantly from 8.5 to 33.5 ps on going from an etch depth of 850 nm to an etch depth of 100 nm.

A small change in the decay constant was found for a different sample with period  $a = 330$  nm and air fill factor  $f = 20\%$ , for a smaller variation of the etch depth. For an etch depth of 100 nm the decay constant was measured to be 35.6 ps whereas for a 200 nm etch depth the decay constant was measured to be 29 ps.

The variation of the decay time with etch depth can be understood by realizing that by reducing (increasing) the etch depth, the surface area is also reduced (increased), and therefore the amount of surface recombination taking place decreases (increases), which explains the increased (decreased) decay times.

It was found that there is a good correlation between the relative surface area sizes and the relative nonlinear response decay times. A reduction of the surface area of 4.5 times, on going from an etch depth of 850 nm to an etch depth of 100

nm, resulted in the nonlinear response decay time increasing by 4 times, from 8.5 ps to 33.5 ps. Similarly, a reduction of surface area of 1.4 times, on going from an etch depth 200 nm to an etch depth of 100 nm resulted in the nonlinear response decay time increasing by 1.2 time, from 29 to 35.6 ps.

This shows that the nonlinear response decay time of one dimensional photonic crystals can be controlled by altering the photonic crystals parameters, namely: period, air fill factor and etch depth.

I have also demonstrated subpicosecond switching of photonic resonances via the optical Kerr effect when pumping off resonance at 2.1  $\mu\text{m}$ . A nonlinear response time of approximately 400 fs was found for this effect. Interestingly, the photonic resonance was not shifted, but partially bleached. The shift of the photonic resonance was calculated to be 0.3 nm which is almost undetectable. A linear dependence of the change in refractive index on input power was found as predicted from theory.

Finally, resonant subpicosecond switching of photonic resonances via the optical (ac) Stark effect was also demonstrated when pumping almost resonantly with the exciton at 800 nm.

An even faster nonlinear response time was found: approximately 300 fs. The difference in response was attributed to the effect of the different pulse widths for the different wavelength of the TOPAS OPA on the pulse width of the white light continuum. Similarly to the optical Kerr effect, the optical Stark effect was shown to depend linearly on the input power. A value for the nonlinear

refractive index  $n_2 = 5.2 \pm 4.1 \times 10^{-12}$  was extracted from the data. This value compares well with literature values.

The highly resonant nature of the optical Stark effect was also studied. Resonant excitation provided no effect as expected. For a small detuning of 8 nm, the effect was reduced by almost 5 times.

The applicability of the optical (ac) Stark effect in real world devices is limited by the effect of real carriers due to two photon absorption which will feature for high enough laser intensities.

These results demonstrate the excellent potential of III-V based high refractive index contrast photonic crystals in general, and one dimensional high refractive index contrast photonic crystals in particular, in ultrafast all-optical switching devices.

**References:**

1. A. D. Bristow, J.-P. R. Wells, W. H. Fan, A. M. Fox, M. S. Skolnick, D. M. Whittaker, A. Tahraoui, T. F. Krauss, J. S. Roberts, "Ultrafast nonlinear response of AlGaAs two-dimensional photonic crystal waveguides" *Appl Phys Lett* **83**, 851 (2003).
2. M.J. LaGasse, K.K. Anderson, C.A. Wang, H.A. Haus, J.G. Fujimoto, "Femtosecond measurements of the nonresonant nonlinear refractive index in AlGaAs" *Appl Phys Lett* **56**, 417 (1990).
3. A. D. Bristow D. O. Kundys, A. Z. García-Déniz, J.-P. R. Wells, A. M. Fox, M. S. Skolnick, D. M. Whittaker, A. Tahraoui, T.F. Krauss, J.S. Roberts, "Ultrafast nonlinear tuning of the reflection properties of AlGaAs photonic crystal waveguides by two photon absorption" *J. Appl. Phys.* **96** 4729 (2004).
4. D.E. Aspnes, "Recombination at semiconductor surfaces and interfaces" *Surf. Sci.* **132** 406 (1983).
5. S.R. Hastings, M.J.A. de Dood, H. Kim, W. Marshall, H.S. Eisenberg and D. Bouwmeester, "Ultrafast optical response of a high-reflectivity GaAs/AlAs Bragg mirror" *Appl Phys Lett* **86**, 031109, (2005).
6. H.W. Tan, H.M. van Driel, S.L. Schweizer, R.B. Wehrspohn, U. Gösele, "Nonlinear optical tuning of a two-dimensional silicon photonic crystal" *Phys. Rev. B* **70**, 205110 (2004).
7. J.P. Prineas, J.Y. Zhou, J.Kuhl, H.M. Gibbs, G. Khitrova, S.W. Koch, A. Knorr, "Ultrafast ac Stark effect switching of the active photonic band gap from Bragg-periodic semiconductor quantum wells" *Appl Phys Lett* **81**(23) 4332, (2002).
8. M. Shimizu, T. Ishihara, "Subpicosecond transmission change in semiconductor-embedded photonic crystal slab: Toward ultrafast optical switching" *Appl Phys Lett* **80**(16) 2836, (2002).
9. J.U. Kang, A. Villeneuve, M. Sheik-Bahe, G.I Stegeman, K. Al-Hemyari, J.S. Aitchison, C. N. Ironside, "Limitation due to three-photon absorption

- on the useful spectral range for nonlinear optics in AlGaAs below half band gap” Appl. Phys. Lett. **65**, 147 (1994).
10. P.N. Butcher, D. Cotter, “The Elements of Nonlinear Optics”, Cambridge University Press (1990).
  11. A. Mysyrowicz, D. Hulin, A. Antonetti, A. Migus, W.T. Masselink, H. Morkoc,” “Dressed excitons” in a multiple quantum well structure: Evidence for an optical stark effect with femtosecond response time” Phys Rev Lett. **56** (25) 2748 (1986).
  12. T. Fujita, Y. Sato, T. Kuitani, T. Ishihara, “Tunable polariton absorption of distributed feedback microcavities at room temperature” Phys. Rev. B **57**, 12428 (1998).
  13. W.H. Knox, R.L. Fork, M.C. Downer, A.B. Miller, D.S. Chemla, C.V. Shank, “Femtosecond dynamics of Resonantly excited excitons in room temperature GaAs Quantum wells” Phys Rev Lett. **54** (12) 1306 (1985).
  14. The pulse width has been measured to be  $\tau_p = 126$  fs. See A.D. Bristow, “Optical investigation of AlGaAs photonic crystal waveguides”, PhD thesis, University of Sheffield, 2003.
  15. D.C. Hutchings, B.S. Wherrett, “Theory of the dispersion of ultrafast nonlinear refraction in zinc-blende semiconductors”, Phys. Rev. B **50**, 4622 (1994) and references therein.

# **Chapter 6: Summary and Conclusions**

## **6.1. Summary and Conclusions**

## **6.2. Future Work**

“640kb ought to be enough for anyone”

*Bill Gates*

## 6.1 Summary and Conclusions

The realization of all-optical photonic crystal based devices that control the propagation and emission of light in the visible/near infrared part of the spectrum is important in the drive towards miniaturization and faster operational speeds.

Silicon has been the material of choice for the semiconductor industry, mainly due to its abundance in the earth’s crust. However, other materials from the II-VI and III-V ranges are better suited for the optoelectronics industry. In this work, different alloys of AlGaAs have been successfully used to create photonic structures. The advantages of AlGaAs are numerous: patterned structures exhibit high refractive index contrasts, necessary for full band gaps; fabrication and growing techniques are an extension of techniques developed by the optoelectronics industry; they possess large nonlinearity and good light emitting properties.

Chapter 2 presents a theoretical introduction to the linear and nonlinear properties of photonic crystals. The master equation is derived and its properties discussed. Symmetry is studied and it is shown how it can help the study of photonic crystals. An introduction to nonlinear optics is also presented.

In Chapter 3, a photonic stop gap was found for both transverse magnetic and transverse electric polarizations along the  $\Gamma$ -K lattice direction using in-plane transmission spectroscopy on photonic crystals embedded in ridge waveguides.

The nonlinear response of the photonic crystals was found to be almost completely dwarfed by the nonlinear response of the ridge waveguide itself.

Careful design and patterning is needed to ensure a complete band gap along all lattice directions. It is clear that in order to realize the potential in all-optical switching devices of these structures the ridge waveguide length has to be minimized. The length of the photonic crystal can also be extended, which would have the added effect of increasing the attenuation in the photonic band gap, thus further increasing the contrast between the on/off states of a switching device. The emphasis of the work shifted to reflectivity measurements as the obstacles in the study of the nonlinear properties of photonic crystals embedded in ridge waveguides proved insurmountable.

Chapter 4 discusses the linear and nonlinear properties of high refractive index contrast one dimensional InAlGaAs/AlGaAs multiple quantum wells photonic crystal waveguides. An external coupling technique in reflectivity geometry is used to measure these structures. The time resolved nonlinear response is measured using a spectrally resolved pump-probe technique. The high intensity pump excites free carriers into the conduction band. The photo-generated carriers alter the refractive index of the semiconductor, which in turn alters the photonic crystal band structure. This alteration results in a nonlinear shift of the photonic resonances.

One photon absorption together with two photon absorption were found to be responsible for the excitation of free carriers into the conduction band, for pump wavelengths shorter than the quantum wells exciton. Similarly, two photon

absorption and three photon absorption were found to be responsible for excitation of free carriers, for pump wavelengths in the near infrared (810 nm, 1330 nm) and the infrared (2.1  $\mu\text{m}$ ) respectively. The refractive index change per carrier density was found to be in the same order of magnitude as for bulk AlGaAs. The wavelength shift results in massive changes in the reflectivity close to the photonic resonances. This suggests that this effect could be used in all-optical switching devices.

The nonlinear response decay time was found to be significantly faster than in bulk AlGaAs, around 25 picoseconds. The increased area of photonic crystals over bulk results in increased surface recombination which is responsible for the reduced lifetime of the free carrier nonlinearity.

Chapter 5 focuses on the nonlinear properties of high refractive index contrast one dimensional InAlGaAs/AlGaAs multiple quantum wells photonic crystal waveguides. The free carrier nonlinearity decay time is proved to depend on: the stripe width, determined by the period and air fill factor, and the etch depth of the photonic crystal waveguide.

Longer (shorter) stripe widths result in longer (shorter) lived nonlinear responses. As the carriers have to travel longer (shorter) distances to reach a surface, thus decreasing (increasing) the amount of surface recombination taking place and consequently increasing (decreasing) the lifetime of the nonlinear response. An in-plane carrier scattering model showed good qualitative agreement with the experimental data. A fully fledged three dimensional model is needed to better understand the experimental data.

Similarly, shallowly (deeply) etched photonic crystal waveguides have longer (shorter) lived nonlinear responses due to decreased (increased) surface recombination caused by the reduced (increased) surface area associated with the shallower (deeper) etching.

The possibility to control the nonlinear response lifetime at fabrication time coupled to the large changes in the reflectivity close to photonic resonances make high refractive index contrast one dimensional photonic crystals very well suited to be used in all-optical switching devices.

Subpicosecond switching of photonic resonances was demonstrated via non-resonant pumping, optical Kerr effect, and resonant pumping, optical (ac) Stark effect. The former presented a partial bleaching rather than a wavelength shift of the photonic resonance, while the latter presented a wavelength shift. The virtual nature of these effects ensures that the shift and partial bleaching of the photonic resonances lasts only for as long as the pump beam is on. The optical (ac) Stark effect was shown to depend on the pump exciton wavelength detuning.

These results demonstrate the excellent potential of III-V based high refractive index contrast photonic crystals in general, and one dimensional high refractive index contrast photonic crystals in particular, in ultrafast all-optical switching devices.

## 6.2 Future Work

As discussed in chapter 3, a further attempt to obtain a nonlinear change in the refractive index will be carried out. A photonic crystal fibre will be used to generate a white light continuum to be used as a probe beam, while a more powerful laser is expected to provide the necessary extra intensity that precluded the experiments from working.

In the data presented in chapter 4, the photonic resonances were bleached by the high intensity pump, the actual mechanism responsible for this bleaching is not known, further work in the field needs to address this problem. Interestingly, for pump wavelengths at 1300 nm the bleaching was considerably reduced, the reasons for this reduced bleaching also remains unknown, and needs to be explained.

In chapter 5, subpicosecond optical tuning of photonic resonances was observed via the optical Kerr effect, interestingly, limited bleaching was caused by this effect, rather than a wavelength shift of the photonic resonance. Further investigations of this effect are necessary to establish its origin.

The pump exciton detuning dependence of the optical Stark effect needs to be studied in closer detail, in order to better understand it.

An interesting possibility opened up by multiple quantum well photonic crystal waveguide is the study of polaritons, coupling of a waveguide mode to the exciton. Enhanced exciton oscillator strengths would be required, either by increasing the number of quantum wells, by working in cryogenic temperatures or both.

In order to demonstrate real and virtual carrier switching very high pulse energies were required. This needs to be addressed if these effects are ever to be used outside a research laboratory. In order to lower the switching energy, high Q cavities can be embedded in a ridge waveguide. High Q factors, along with small modal volumes, result in enhanced nonlinearities that could lower the switching energies.